Measurement of Fuel Regression Rate of a Pool Fire in Crosswind With and Without a Large Downwind Blocking Object

by

Chris Best

A thesis

presented to the University of Waterloo

in fulfillment of the

thesis requirement for the degree of

Master of Applied Science

in

Mechanical Engineering

Waterloo, Ontario, Canada, 2010

I hereby declare that I am the sole author of this thesis. This is a true copy of the thesis, including any required final revisions, as accepted by my examiners.

I understand that my thesis may be made electronically available to the public.

Chris Best

Abstract

Transportation accidents and the resulting fires are an important field of study. At the University of Waterloo Live Fire Research Facility (UWLFRF), an experiment was conducted in partnership with Sandia National Laboratories in Albuquerque, New Mexico. This experiment was designed to simulate an aircraft accident where fuel is spilled on the runway and is subsequently ignited. A crosswind pushes the 2.0 m diameter pool fire towards the aircraft fuselage and the conditions around the fire are monitored. Literature on the subject is examined first, examining the relationship between the fire, the crosswind, and the 2.7 m diameter blocking object (aircraft fuselage). A full wind characterization is then presented of the UWLFRF both with and without the blocking object in place, using five distinct wind speeds ranging from 3 m/s to 13.5 m/s. Turbulence intensity measurements are made on the centerline of the facility when possible. Details about the two sets of live fire tests are presented, a control experiment without the blocking object in place and then fire tests with the blocking object in place. Additionally, the control experiment has two different setups, one involving a floor surround in order to diminish the effect of the forward facing step on the front of the fuel pan. The fuel regression rate, the wind speed, the ambient conditions and the heat flux near the fuel pan are monitored during each live fire test. The fuel regression rate, defined as the rate at which the height of the liquid fuel level decreases as the fire burns, is then analyzed versus all other monitored variables. During no blocking object tests, trends of increasing wind speed and increasing heat flux on some gauges and decreasing flux on others was observed with increasing fuel regression rate when the floor surround was in place. During no blocking object tests without the floor surround and tests with the blocking object in place, no strong trends were observed when comparing the monitored variables. The ambient conditions were not observed to have an effect on any test. The average fuel regression for tests without the blocking object in place is 4.0 mm/min without the floor surround, and 4.4 mm/min with it in place. With the blocking object in place the average fuel regression rate was measured to be 4.8 mm/min using load cells and 4.1 mm/min using the sight glass.

Acknowledgements

First off, I would like to thank both of my supervisors, Professor E.J. Weckman and Professor C. Devaud. Without them I would not be in the position I am today, and I thank them for all the patience, guidance and every opportunity I was given. I would also like to thank the following people:

- Gord Hitchman and Cecilia Lam, who helped guide my work with their knowledge and experience, and were always available to help discover solutions to difficult problems,
- Professor Al Strong, Andy Barber, Bill Falagitis, as well as numerous co-op students for all their contributions to our experiments,
- My Family, for always supporting me,
- My wife Emily, who never stopped believing in me.

I would also like to acknowledge the large amount of support received from the following groups:

- the Natural Sciences and Engineering Research Council of Canada (NSERC),
- the Canadian Foundation for Innovation (CFI),
- Ontario Innovation Trust (OIT),
- Sandia National Laboratories,
- Rick Hummel, his staff at the Waterloo Region Emergency Service Training and Research Complex (WRESTRC) as well as the Waterloo Region fire departments present during large-scale fire tests.

CONTENTS

LIST OF TABLES

LIST OF FIGURES

Chapter 1

Introduction

Transportation accidents involving fires resulting from hydrocarbon fuel spills occur with enough frequency that many different studies have been performed, focusing on different accident scenarios such as train accidents and aircraft fuel fires [1 - 7]. These types of accidents often occur outdoors, where the prevailing winds influence the fire and its effect on the surrounding area. During a transportation accident, some form of blocking object may be located nearby, such as a transport truck trailer, a train locomotive or aircraft fuselage. All these factors combine to determine the behaviour of the fire and the subsequent damage caused by the fire.

The University of Waterloo Live Fire Research Facility, henceforth known as the UWLFRF, provides an excellent lab facility in which to more fully understand the mechanisms of transportation fires. This facility has a sizeable experimental enclosure for conducting large-scale fires as well as a crosswind generation system which can produce controlled wind conditions during a fire. In this thesis, results of jet fuel spill fire research conducted in partnership with Sandia National Laboratories of Albuquerque, New Mexico are presented. The behaviour of 2.0 m diameter JP-8 military jet fuel pool fires were examined under varying wind speeds up to 13.5 m/s, with and without a 2.7 m blocking object located 1.0 m downwind of the pan burner.

The first series of experiments were designed to simulate an aircraft fuel spill fire in a crosswind. Therefore the blocking object was present and used to represent an aircraft fuselage. Heat flux near the fire and the blocking object, temperatures in the vicinity of the fire, fuel regression rate of the fire, the velocity behind the blocking object, and ambient conditions

outside the UWLFRF were measured in order to provide comprehensive data to better describe the complex relationship between the behaviour of the pool fire and the surrounding conditions. The fuel regression rate is defined as the rate at which the level of the liquid fuel decreases during a fire, and given the units of mm/min. Overall, 31 live fire tests were performed between 2003 and 2006 with this configuration; 24 of these tests had suitable instrumentation for this work and therefore are presented in this thesis.

For the second series of tests, the blocking object was removed from the UWLFRF. Again 2.0 m diameter pool fires were investigated under varying wind speeds, up to 10.0 m/s. These tests formed a set of reference characterizations of the pool fire behaviour without the blocking object in order to understand the effect of the blocking object in the blocking object fire data. Measurements of the heat flux near the fire, the temperatures in the vicinity of the fire as well as downwind, the fuel regression rate of the fire, the velocity downwind of the pool fire, and ambient conditions outside the UWLFRF were collected. Nine live fire tests were performed in 2007, with eight tests being suitable for inclusion in this thesis.

This thesis will focus mainly on the measurements of the fuel regression rates of the 2.0 m diameter pool fires under the different crosswind and blocking object scenarios. Other measurements, including the wind speed and distribution throughout the facility, local flow turbulence, heat flux near the fuel pan and ambient conditions outside of the UWLFRF during both sets of live fire tests are also detailed in order to examine their effect on the fuel regression rate of the pool fire. Other measurements from these test series and previous characterizations of the UWLFRF are not included as they are contained in complementary theses by Lam [8,9] and Randsalu [10], and Weisinger [11].

The three main objectives for the research reported in this thesis, then, were:

1. To characterize the magnitude and distribution of wind flow inside the UWLFRF both when the blocking object is present and when it has been removed, including a preliminary set of turbulence measurements.
2. To determine fuel regression rates of 2.0 m diameter JP-8 pool fires under varying wind conditions, with and without a blocking object present.
3. To investigate any relationships between fuel regression rate, local wind conditions, heat flux near the pool fire, and the ambient conditions for each test.

In Chapter 2, existing literature is reviewed, including sections on turbulent jets and previous wind characterization of the UWLFRF, as well as more general information on pool fires, fires in crosswinds, fires in the presence of objects and heat transfer within pool fires. Details of previous large scale pool fire experiments performed at the UWLFRF are also included. In Chapter 3, the experimental methods used in this work are presented, including the overall methodology for these large-scale pool fire experiments, as well as instrumentation specific to the present experiments. Chapter 4 will focus on the results of the two series of large-scale pool fire tests; the series without the blocking object present, and then the series where it is in place. The fuel regression rate from different tests will be compared against wind speed data collected during flow characterization in the UWLFRF and local heat flux data measured during each experiment. Finally, Chapter 5 will present a summary and the conclusions reached in the previous chapters, as well as recommendations for future work.

Chapter 2

The Literature In Review

This chapter will cover previous literature on two aspects related to the thesis. It begins with an examination of the literature related to the wind generation system and crosswind flows in the UWLFRF. This includes sections on turbulent jet behavior, rectangular jets, and previous attempts at characterization of the wind distribution in the UWLFRF. Following this is a summary examination of current knowledge about the physics of pool fires, as well as the different types of heat transfer occurring within a fire. The fuel regression rate of the fire is related to the heat transfer from the flames to the fuel surface and the relationship between the two will be examined. Next, existing research on the effect of a crosswind on a pool fire, as well as on fire fuel regression rate, will be examined. Finally, some of the experiments presented in this work involve a blocking object; therefore past research into the effect of a blocking object on a fire is also summarized here.

2.1 Literature Related to Characterization of Crosswinds in the UWLFRF

The UWLFRF has a crosswind system that uses six separate fans to generate the wind, which then travels through a plenum before reaching the test enclosure itself (see Section 3.1.1). No previous research into multiple, large scale parallel round jets discharging simultaneously into an enclosed room was identified in this work, therefore, in order to attempt to understand the flow patterns inside the UWLFRF, literature on turbulent jets issuing into a quiescent atmosphere is first discussed. The plenum exit where the jet flow enters the test enclosure has a width/height aspect ratio of approximately 1.5 (see Section 3.1.1). Previous investigators have likened the

flow to that in a bluff wall jet and reviewed the associated literature [11]; however, the plenum aspect ratio is larger than the aspect ratio of 1.0 used to generate the standard turbulent bluff jet, hence the following sections will briefly summarize the key flow features of a bluff jet and relate it to the flows observed in rectangular jets.

2.1.1 Turbulent Jet Behaviour

In general, there are three distinct structures that form as a turbulent bluff jet exits a nozzle and enters a quiescent atmosphere [12 - 14]. A potential core, wherein the flow maintains a constant velocity equal in magnitude to that at the jet exit, forms in the central region of the flow after the nozzle exit. Downstream of this potential core, a region of transitional flow forms as mixing and entrainment occur between the jet and the surrounding air. After the transitional flow region, the jet becomes fully developed and the flow is characterized by a self-similar region. In this fully developed region, the jet has spread considerably and mixing has occurred all the way into the central region of the jet while the velocity near the centre of the jet has decreased. Shear layers, areas of high velocity gradient, demarcate the edges of the jet as the flow slows down to match the velocity of the surrounding air.

As the jet travels downstream, it increases in size and the centre-line velocity decreases as surrounding air is entrained into the edge of the flow. These two phenomena are balanced based on momentum conservation as the jet travels downstream. The static pressure in the jet remains constant unless the jet impinges on some form of blockage during its evolution [13]. The constant velocity in the potential core region is due to this constant static pressure. If the static pressure varies as the jet travels downstream, the velocity decay is affected when compared to a jet where the static pressure is constant. An increase in the static pressure increases the rate at

which the velocity decreases, while a decrease in the static pressure decreases the rate of velocity decay.

2.1.2 Rectangular Turbulent Jets

A rectangular turbulent jet is defined as a jet with a nozzle width/height (aspect ratio) of more than 1.0. It shares many similar features to those of the turbulent bluff jet discussed above, but as the aspect ratio of the rectangular jet increases, differences in the flow characteristics evolve.

Similar to the turbulent jet discussed above, the rectangular jet exhibits three distinct regions of flow development as it issues downstream into a quiescent atmosphere. As illustrated in Figure 2.1, these are again a potential core, a transitional region and the fully developed region (the region prior to point A, the region in between point A and B, and the region beyond point B respectively in Figure 2.1). In the potential core, the axial components of velocity are essentially constant. The nature of the jet then changes in the transitional region. The transitional region, also known as the two-dimensional region when referring to rectangular jets, forms when the shear layers between the surrounding air outside the jet and the flow issuing from the short sides of the rectangular nozzle meet on the centre-line [15]. In Figure 2.1, these two shear layers occur in the X-Y plane, as the smallest side of the nozzle is in this plane. Velocity begins to decay at a rate similar to a planar jet in this region as well. Finally, when the shear layers of the long side of the nozzle meet, the X-Z plane in Figure 2.1, the rectangular jet becomes axisymmetric and its overall flow character becomes self-similar as for the round jet [14 - 16]. The exact location of these three regions and their transition points depends greatly on the geometry of the test enclosure and the aspect ratio of the nozzle. For instance, a jet with a larger aspect ratio becomes

axisymmetric farther downstream [14 - 16]. The presence of sidewalls in the surrounding ambient air also affects the evolution of the turbulent jet. Therefore, a jet issuing into a surrounding enclosure will behave much differently than a free jet. Prior research has shown that the potential core region of a low aspect ratio rectangular jet such as the one at the UWLFRF will end approximately 4 diameters downstream, while the transitional two-dimensional region will end approximately 60 diameters downstream [15], where the diameter of a non-round jet is defined as 4A/P, P being the perimeter of the jet and A being the cross-sectional area of the jet. Previously, jets with two sidewalls have shown delayed development from the potential core region to the transitional region, but there is presently no agreement on the effect of four sidewalls [16].

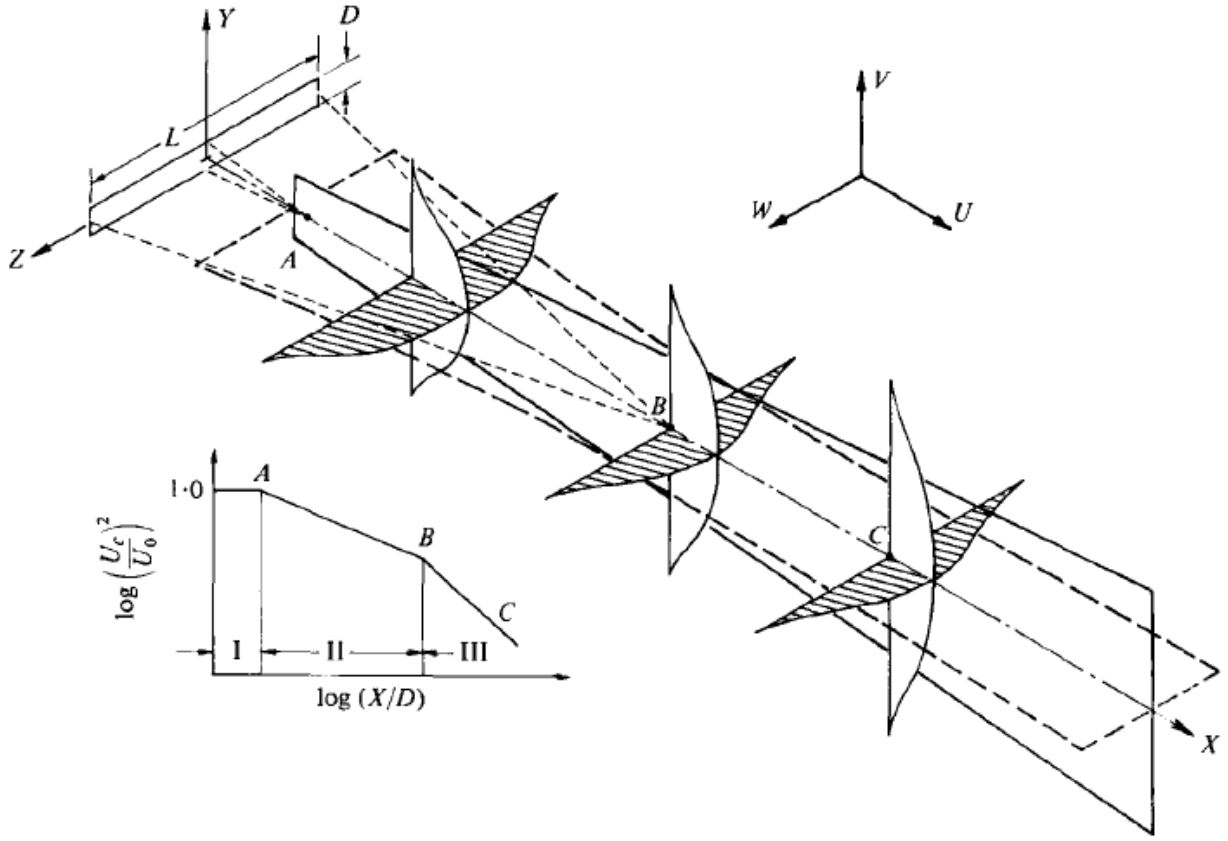

Figure 2.1 The evolution of the flow field of a rectangular Jet [15]

When examining the velocity profile of a rectangular jet prior to the fully developed region, a so-called saddle shape velocity profile tends to form in the direction of the nozzle long axis with maximum measured velocities displaced laterally from the centre-line [14, 15]. This velocity profile is thought to be caused by a series of closed vortex rings within the jet generated at the jet nozzle exit and carried some distance downstream [14 - 16]. Before reaching the fully developed region, these vortex rings break down and cause secondary motion within the plane of the jet cross section, resulting in a velocity configuration with the saddle shape velocity profile mentioned above. These vortex rings have also been observed in round jets, and are thought to form the coherent large scale turbulent structures of the jet in the mixing layer region[18], underscoring the similarities in the flow profiles of rectangular and round jets downstream of the nozzle exit [14, 18].

2.2 Experimental Studies in Wind Characterization at the UWLFRF

In previous work, Weisinger [11] conducted some preliminary measurements to characterize the crosswind flow distribution within the large test enclosure of the UWFRF. Using bidirectional probe sensors and a traversing apparatus, radial profiles of velocity were measured across different vertical planes 2.0, 5.0, 10.0, 15.0 and 17.4m downwind of the facility inlet; however, the results were limited to measurements made only at the maximum velocity (fan speed) of 13.5 m/s (60 Hz). In Figure 2.2, the measured velocity contour maps are reproduced for the five downwind measuring points: x = 2 m, 5 m, 10 m, 15 m, 17.4 m. The key features of the flow observed in that work are discussed below.

As shown in Figure 2.2, at the highest wind velocity the flow through the facility is composed of two regions: a central core region surrounded by regions of slower moving flow

towards the outer edges of the measuring area thought to be caused by flow field interactions with the test enclosure walls and quiescent air towards the ceiling. In the central core, there are initially many regions of elevated velocity, which begin to merge with distance downwind of the plenum exit. From this region, the velocities then gradually decrease towards the test enclosure walls. Weisinger observed that the central flow resembles that of the potential core of a bluff wall jet with relatively uniform velocities [12, 19, 20].

The dimensions of the test enclosure plenum are 5.89 m by 7.60 m wide, and the farthest measurement location is 17.4 m downstream. Using the smallest dimension of the test enclosure plenum as the diameter, the farthest measuring point is approximately three diameters (17.4 m / 6.6 m) downstream of the exit. According to the literature, the potential core region of this bluff wall jet extended a minimum of six diameters from the inlet [19, 20]. Unlike a pure jet flow, two areas of elevated velocity were observed very close to the floor at the UWLFRF, which merged into a single jet as they traveled through the enclosure. It was concluded that the two jets near the floor were non-symmetrical parallel jets [21 - 25].

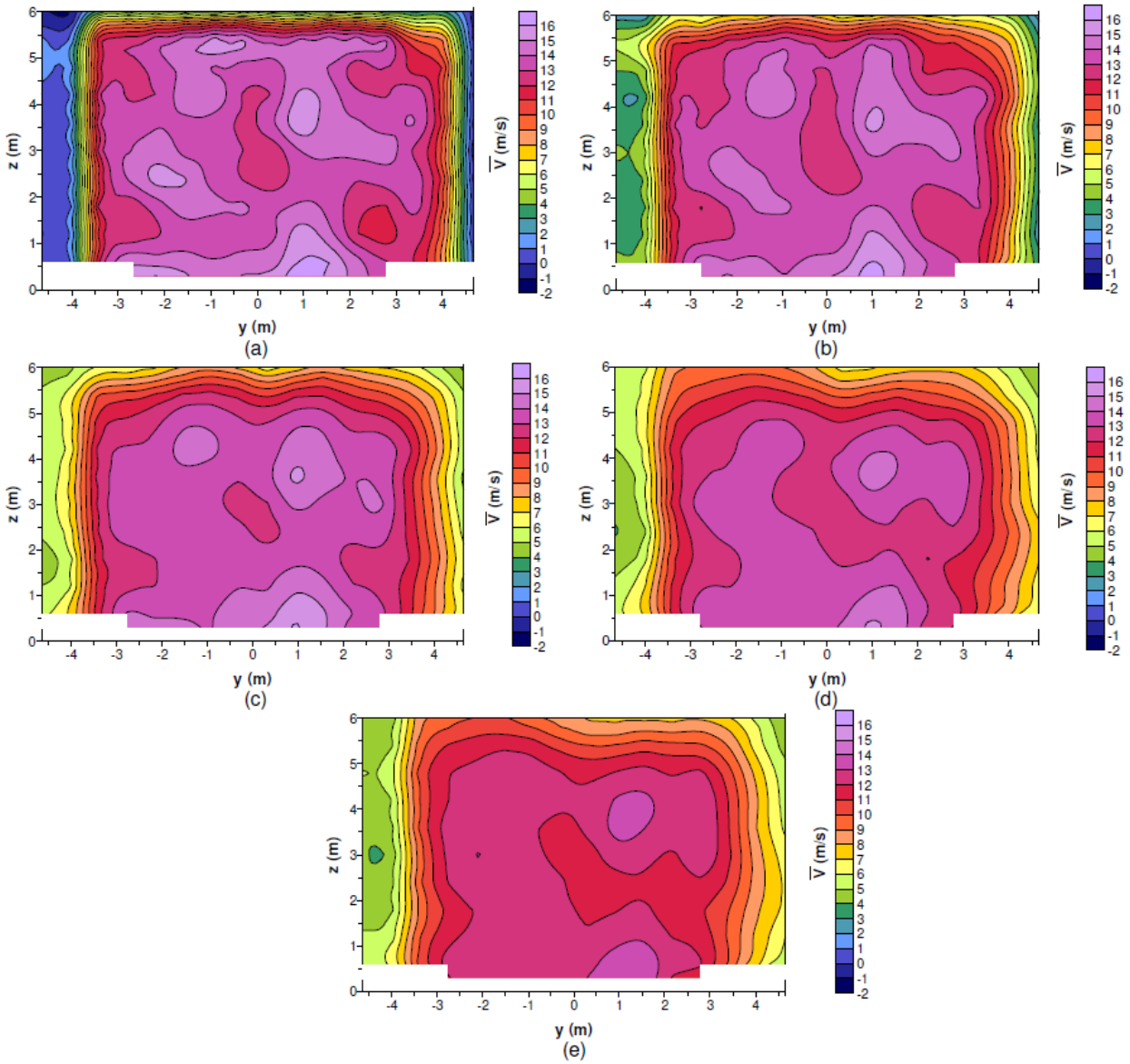

Figure 2.2: Velocity Contours in the empty plane enclosure at the a) x=2m plane; b) x=5m plane; c) x=10m plane; d) x=15m plane; and e) x=17.39m plane. [11]

Weisinger also performed velocity measurements to characterize the test enclosure for the highest fan setting, when a cylindrical steel blocking object, 2.7 m in diameter, mounted 1 m off the ground was in place in the test enclosure. This object was oriented perpendicular to the direction of the flow, and mounted 7 m downwind of the test enclosure inlet.

Results are summarized in Figure 2.3 for locations at x = 2 m, 5 m and 15 m downwind of the plenum exit. Comparisons made of the results in Figure 2.2 for the empty test enclosure and Figure 2.3 for the enclosure with a blocking object present indicated that the flow distribution upwind of the blocking object, at x = 2 m was very similar to that in the empty test enclosure [Figure 2.2], with only a slight overall decrease in the magnitude of the velocity [Figure 2.3]. At x = 5 m, the flow stagnation and diversion of the flow due to the presence of the blocking object can be seen, with decreased velocities near the center of the core region and elevated regions above and below. Measurements taken at x = 15 m behind the blocking object [Figure 2.3] indicated the wake behind the object as would be expected for flow past a cylindrical object [26].

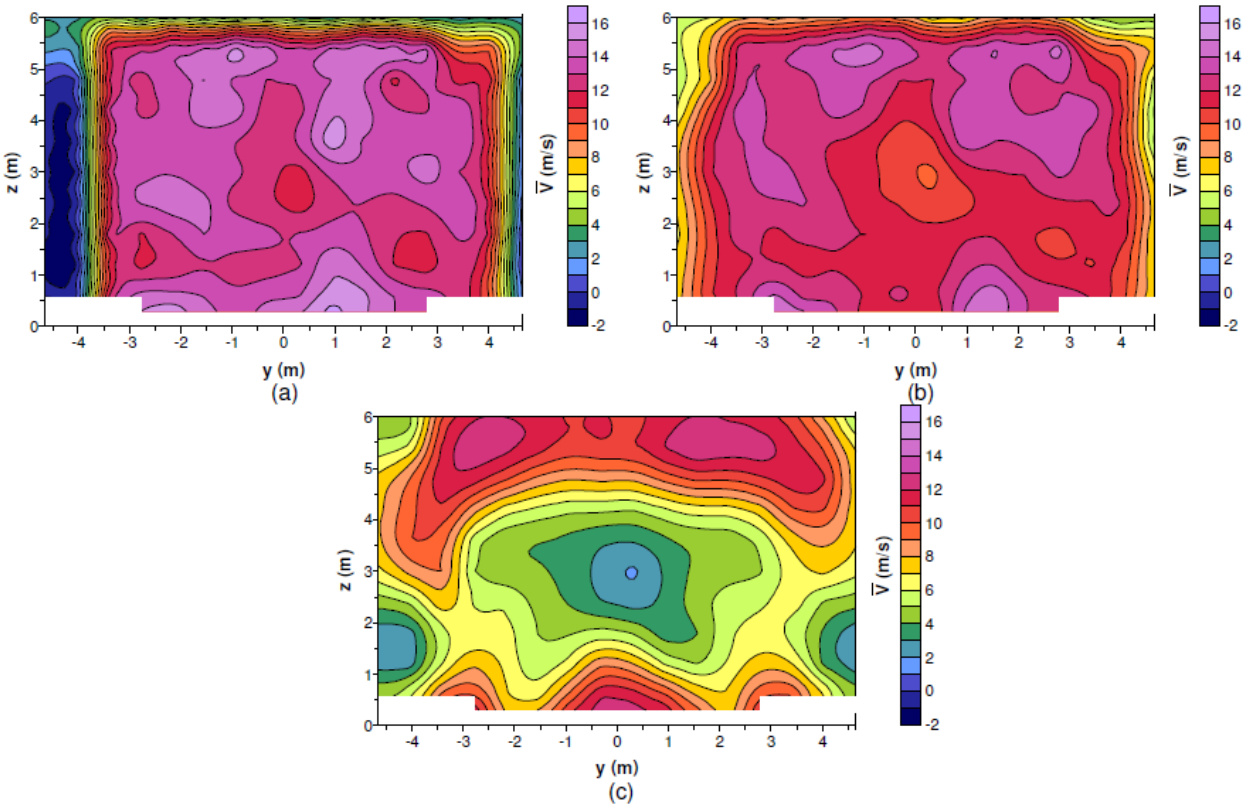

Figure 2.3 Velocity Contours at the a) x=2m plane; b) x=5m plane; and c) x=15m plane; with the blocking object in place [11]

These previous results indicate that the experimental methods used by Weisinger are appropriate for flow characterization in the UWLFRF. Since measurements were restricted to the maximum wind velocity however, they could not be used to describe the flow at any intermediate velocity. Therefore, flow characterization at a series of intermediate velocities is one purpose of the present research.

2.3 Pool Fires

Since the second main objective of this work was to investigate burning rates in large pool fires under different crosswind conditions, this section will be devoted to a discussion of literature on pool fire behaviour. Sections on pool fire heat transfer, objects immersed in pool fires and the effect of a crosswind on a pool fire are included.

There has been a considerable amount of research conducted into the behaviour of medium and large scale liquid fuelled 'pool' fires. Although much of this research was performed under controlled laboratory conditions [27 - 33], the many variations in boundary conditions and experimental configurations used makes comparisons between different series of tests quite difficult. To interpret the results, attention must be paid to the effect of these differences between experiments on the final results [29, 31, 34 - 36], including even small variations in common parameters such as lip height in liquid fuel burner pans, floors surrounding a pan burner, ambient temperature, ambient wind conditions and even diameter of the burner pan itself.

When liquid fuel in a pan burner is ignited, the ensuing pool fire relies on continued evaporation of fuel to feed the combustion process. This evaporation is controlled by heat transfer into the surface of the fuel [37], which relates directly to the burning rate of the fuel and the heat release rate of the fire. The amount of air being entrained into the edges of the fire also greatly influences the burning rate of the fuel. This air does not immediately travel into the interior zones of the fire [35, 38], but is instead consumed by the outer flame regions near the base of the fire. This creates a fuel rich 'unburned vapour' zone in the interior of the fire immediately above the surface of the fuel, which is thought to play a significant role on heat transfer back to the fuel surface [39 - 43].

Blinov and Khudyakov performed the first landmark study of burning rates and flame heights in pool fires [44, 45]. For a wide range of burner sizes and fuel types, they tracked the burning rate of the fuel, which they presented as liquid burning velocity in Figure 2.4.

They found that regression rate depended greatly on pool diameter; the regression rate decreased with increasing diameter until a critical size after which the regression rate began increasing again. As the diameter was increased further, the regression rate eventually leveled off to a constant value. Overall, this relationship was not influenced by the type of petroleum fuel tested [44]. Based on their findings, Blinov and Khudyakov characterized pool fires into laminar, transitional and turbulent fires depending on pool diameter. The laminar region was characterized by decreasing fuel regression rates as pan diameter increased, until pool diameters of around 0.1 m. At the other extreme, the turbulent region was found to begin at diameters of around 1 m and was characterized by fuel regression rates that remain nearly constant with increasing diameter. Fires with diameters between 0.1 m and 1 m were considered to lie in a transitional pool fire regime. Hottel corroborated these results when attempting to add to the

analysis of heat transfer in pool fires [46], while Magnus did the same for gasoline pool fire tests [47]. Other studies done after Blinov and Khudyakov agree with many of their findings; however, some examples of increases in regression rate with increasing pool diameter have been found in later studies into turbulent pool fire behaviour in large diesel fuel and crude oil pool fires [48, 49].

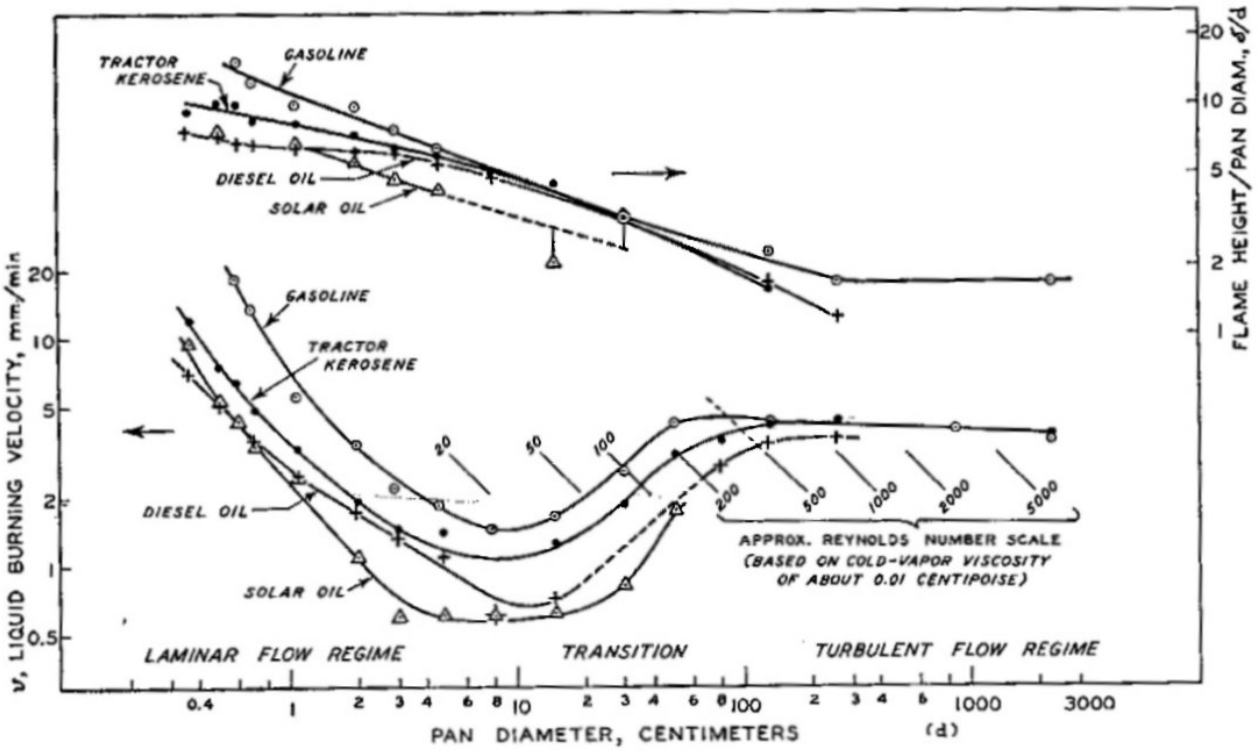

Figure 2.4 Liquid Burning Rate of Pool Fires versus Pan Diameter for Different Fuels [44]

Overall, when examining the effect of pool diameter on pool fire behaviour, the results of Blinov and Khudyakov are considered to be consistent with most experiments. Experiments that do show differing trends demonstrate the importance of examining all the key variables which can influence the behaviour of pool fires.

2.3.1 Heat Transfer in a Pool Fire

Fuel regression rates in fires are directly related to the formation and burning of vapour from the liquid fuel surface. Since vapour formation is inherently linked to heat transfer within fires, it is important in studying fuel regression rate to outline current understanding of heat transfer in fires. Blinov and Khudyakov [44, 45] investigated the modes of heat transfer occurring in the fires for each regime of behaviour. Conduction and convection were the primary forms of heat transfer in small diameter laminar pool fires, with heat conduction from the hot fire gases to the liquid fuel and burner pan creating convection currents and additional heat transfer within the bulk of the liquid fuel. In contrast, these two heat transfer modes are not nearly as prevalent in larger, turbulent pool fires, where radiation becomes the primary form of heat transfer. Since radiative heat transfer is independent of pool fire diameter, the regression rate also remains constant with increasing diameter [50, 51]. In a later study, Babrauskas [52] focused on the flow field in pool fires ranging in diameter from 0.05m to more than 1m and classified the pool fire as either laminar or turbulent, disregarding the transitional pool fires defined by Blinov and Khudyakov. Considering only two forms of heat transfer, convection and radiation, Babrauskas argued, as had Blinov and Khudyakov, that radiation began to dominate heat transfer

in the fire for large diameter, turbulent fires. However, the transition from laminar to turbulent pool fires occurred at a diameter of 0.2 m in Babrauskas definition of pool fire burning regimes.

Shinoda, Koda and Akita [40] performed a series of pool fire experiments with different fuels and diameters in order to further quantify the importance of radiation heat transfer in large pool fires. They estimated that for a 0.3 m diameter heptane fire, radiation accounted for 65 % of the total heat flux into the fuel. As the diameter increased to 0.7 m and then 1 m, the radiative fraction of total heat to the fuel increased to 80 %. Yumoto [50] performed similar experiments with n-hexane and gasoline using pools of 1.5 and 3 m diameter and showed that, for these fuels, radiation accounted for 60 to 70 % of the total heat feedback to the fuel surface. Using JP-5 aircraft fuel, Alger et al [51] measured the radiative heat flux to the surface of a 3 m diameter pool fire and found it to be 85 %. In all the above results, radiation was shown to dominate heat transfer to the fuel surface of a large pool fire; however the fraction of total energy to the surface attributed to radiation heat flux appeared to depend on fuel type and/or fire diameter. Since the fuel regression rate of a pool fire is dependent on this heat transfer to its surface, this radiative heat flux fraction greatly influences the behaviour of the pool fire.

Other research into the burning rate of pool fires further investigated the distribution of radiative flux back to the fuel surface, although the experiments were conducted on relatively small fires with diameters in Blinov and Khudyakovs transitional regime. Corlett and Fu [34] placed a small test well of fuel at various positions within 0.225 m diameter pool fires and measured the regression rate at each location using two fuels with different luminosity - methanol or acetone. The acetone fire showed decreasing regression rate as the well was placed farther away from the center of the pan. The regression rate in the methanol fire initially decreased with distance from the centre of the pan, but then increased towards the outer edges,

finally reaching a higher regression rate than that recorded in the center of the pan. This led Corlett and Fu [34] to conclude that at the center of the pan radiation is the dominant form of heat transfer, but convection becomes more important farther away from the center of the pan. Blinov and Khudyakov [44] found the same trend during tests with luminous but sooty fuels such as tractor kerosene and diesel oil.

Some attempts have been made to directly formulate an energy balance on the surface of the liquid fuel in a pool fire burner, as well as to develop more general expressions describing heat transfer in pool fires. In this light, Hottel [46] considered contributions from conduction, convection and radiation for fires of various sizes, as shown in Equation 2.1.

$$\frac{q}{\pi D^2/4} = \frac{4k(T_f - T_b)}{D} + h(T_f - T_b) + \sigma F_{f-b}(T_f^4 - T_b^4)(1 - e^{-\kappa D}) \qquad [2.1]$$

In Hottels equation, q is the total heat transfer from the flame to the fuel pool in Watts, D is the pool diameter in meters, T_f is the flame temperature in Kelvin and T_b is the fuel temperature in Kelvin. The right hand side of the equation contains the contributions to the total heat transfer from conduction, convection and radiation. Conduction is represented by the first term, which contains k, a thermal conductivity coefficient with units of W/mK. The next term on the right hand side represents convection and contains h, a convection coefficient with units of W/m^2K. The radiation contribution to the overall heat transfer is calculated in the final term on the right hand side, containing the Stefan-Boltzman constant σ which is given in the units of W/m^2K^4, the geometric view factor between the flame and the fuel pool F_{f-b}, and Beer's law absorption coefficient κ, which is based on the radiation wavelength and has the units $1/m$. In agreement with studies discussed above, Hottel found that contributions from conduction decrease

considerably as the pan diameter increases, since the pool diameter is located in the divisor of the conduction term in Equation 2.1. Convection is not affected by the pool diameter in this equation. Radiative heat transfer begins to dominate, and becomes almost constant, as the pool diameter increases, which causes the final term in the radiation expression to approach a value of 1. When this happens, radiation is solely determined by the view factor between the flame and the fuel pool and the temperatures of the flame and fuel pool to the fourth power.

Hamins et al [28] proposed a similar energy balance at the fuel surface which considered conduction, convection and radiation heat transfer from the fire plume to the liquid fuel surface and is seen in equation 2.2.

$$q_{net} = q_{cond} + q_{conv} + q_{rad} - q_{reflect} = q_{vap} + q_{rerad} + q_{loss} + q_{corr} + q_{water} \quad [2.2]$$

The radiative term, q_{rad}, and convective term, q_{conv}, are the biggest factors in determining q_{net}. The conduction term, q_{cond}, represents heat being conducted through the walls of the pan in which the fire is taking place. Losses take many forms in this equation, including reflection of radiation off the pool surface, $q_{reflect}$, heat being reradiated to the surroundings from the fuel surface, q_{rerad}, heat being lost through the bottom and sides of the fuel pan, q_{loss}, the heat necessary for the growth of a thermal layer inside the liquid fuel, q_{corr}, and the effect on the heat feedback of water condensation on the fuel surface, q_{water}. The energy necessary to boil the fuel and convert it to vapour is represented by q_{vap}. Through this more detailed analysis, Hamins et al concluded that both convection and radiation heat transfer mainly contributed to the energy from the fire plume that reached the surface of the fuel. However, the strength of the convective and radiative fluxes varied depending on the location at the fuel surface. Testing was done with 0.3 m diameter pool fires with various luminous and non luminous fuels. For both luminous and non

luminous fires, radiation was the dominant form of heat transfer at the centre of the pool. As the edge of the pool was approached, the contribution from radiation decreased while the contribution from convection and conduction through the pan walls increased in order to balance out the heat transfer.

When the heat transfer relationships discussed in this section are examined, there is an agreement that in a large, turbulent pool fire, radiation is the dominant mode of heat transfer. Depending on the luminosity of the fuel, the amount of radiative heat transfer to the fuel surface will change, but it will always represent the majority of the heat transfer in a large turbulent pool fire.

2.3.2 Radiation and Fuel Regression Rate

Due to the importance of radiation heat flux to the fuel of large pool fires, attempts have been made to directly relate radiation from the fire with fuel regression rate. These have proven to be reasonably successful. Masliyah and Stewart [54] derived a radiation model using experimental data from Blinov and Khudyakov [45] for gasoline and petroleum fires with diameter greater than 0.3 m which reasonably predicted the fuel regression rate. Burgess et al [29, 55 - 57] developed a fuel regression rate equation for large fires of varying fuel types [Equation 2.3] by simplifying Hottel's [46] heat transfer relationships to reflect primarily radiation heat transfer [Equation 2.1].

$$R = R_{\infty}(1 - e^{-\kappa D}) \qquad [2.3]$$

In this equation, R represents the predicted regression rate in mm/min, D is the pool fire diameter in meters, κ is the refractive index from the Beer-Lambert law with units of $1/m$ and R_{∞} is the

maximum (asymptotic) regression rate for a pool of infinite diameter, which is a constant in this equation. This relationship predicted the burning behaviour of n-butane and n-hexane fires of diameters up to 1.3 m quite well; however, it did not fit data from benzene fires of similar size [57]. The lack of agreement was attributed to the effects convection and ambient air currents in the benzene fires, effects which were not included in the development of equation 2.3.

Initial attempts to quantify R_∞ used the ratio of the heat of combustion of the fuel over the heat of vaporization of the fuel at ambient temperatures, q_{comb}/q_{vap}. This under predicted the regression rates of large LNG (liquid natural gas) fires, prompting the development of a new relationship based on the mass rate of burning per unit area of fuel, $\dot{m}''$ with units of $kg/m^2\,s$. This new relationship is shown in equation 2.4.

$$\rho R = \dot{m}''(1 - e^{-\kappa\beta D}) \qquad [2.4]$$

In this equation, $\dot{m}'' = \rho R_\infty$, and ρ is the density. Values for $\dot{m}''$ and $\kappa\beta$ where β is a correction factor depending on the configuration, were defined by Babrauskas [52].

Again, this equation indicates that radiation is the primary form of heat transfer in large pool fires. Nonetheless, convection is not negligible and a regression rate relationship taking into account both forms of heat transfer may be the most accurate method.

2.3.3 Other Parameters Affecting Fuel Regression Rate

The fuel regression rate is affected by many different factors, including the pan diameter, the type of the fuel and the details of heat transfer to the liquid fuel surface. However, there are

also other factors that may affect the fuel regression rate. These include conduction through the walls of the pan burner, the presence of a floor around the fire, and the lip height of the pan burner itself.

Previously, it was noted that conduction through the walls of the pan can play a large role in governing the fuel regression rate of small diameter pool fires. It is also thought to be a factor in fires where the liquid fuel height is substantially lower than the height of the pan [27, 34, 44]. In either scenario, conduction of heat through the pan walls results in a loss of energy being fed back to the fuel surface and thereby leads to a decrease in the overall fuel regression rate. In both scenarios, however, the effects of conduction on the regression rate will decrease significantly as the pan diameter increases because of increased lengths over which heat transfer has to occur and the role of radiation in controlling the regression rate of large pool fires.

The presence of a floor around a pool fire pan burner is thought to affect fire behaviour, in particular the fuel regression rate of the fire, due to its impact on the availability of air around the fire, as well as secondary heat transfer to the floor itself. In experiments where a floor was built up to the lip of the fuel pan, the fire itself appeared to be less stable, resulting in lateral motions of the fire plume, as well as the formation of swirling vortices [29, 31, 35, 36, 58]. This also resulted in increased fuel regression rate when the floor was even with the lip of the fuel pan. In addition to changes in air entrainment into the fire plume, heating of the floor was thought to have caused convection columns to form around the main fire plume, which were in turn entrained by the fire and increased the amount of ambient air being fed into the fire [31]. When the floor was removed, these phenomena became less prevalent, or even disappeared, and the fire plume became stable again. In one study [29], it was thought that the floor around the fuel pan served as a location for ignited fuel vapours, heavier than air, to diffuse outward from

the fuel pan, and thereby increasing the fuel regression rate as more fuel outside of the pan becomes ignited during this flame instability. Therefore, there is agreement that the presence of a floor flush with the lip of the fuel pan increases the fuel regression rate due to possible flame instability causing some of the fire to leave the fuel pan and increased air entrainment due to floor heating around the fuel pan and subsequent convection columns.

The pan burner lip height, or distance between the surface of the fuel and the top of the fuel pan, is also a factor that affects the fuel regression rate. It is thought that the presence of a 'lip' can result in increased turbulence and mixing within the fire itself, as well as in the fuel vapour zone near the fuel surface. In a 0.38m diameter polymethyl methacrylate (PMMA) fire, the regression rate was found to double as the lip height was increased from 0 mm to 51 mm [59]. Flame thickness within the pan increased and the fire itself became more turbulent as the lip height increased in this case.

In contrast to what is suggested above, however, in fires with diameters of up to 1.2 m fuel regression rates decreased when the lip height was increased [34, 44, 47]. In two of these cases, the diameter of the pool was significantly smaller than its height [44, 47]. In more shallow pool fires, fuel regression rates in fires with diameters up to 0.15 m was also found to decrease with increasing lip height [31]. These results are not as simple as they seem however. When the heat required to heat the exposed pan and the fuel from ambient to test conditions is taken into account, the regression rate actually increases with increasing lip height.

All of the above factors affect the fuel regression rate of a pool fire and must be accounted for during experimentation and interpretation of the results. Factors like radiative and convective heat flux to the fuel surface obviously contribute a great deal to the resulting fuel

regression rate, but even smaller details like lip height of the fuel pan and the presence of a floor around the fuel pan can noticeably affect the fuel regression rate. Failure to acknowledge these factors will lead to confusing results which may or may not be comparable to previous research data.

2.4 Fires in Crosswind

Since many fires occur outdoors and are greatly influenced by the prevailing winds, it is very important to understand the effects of winds on pool fire behaviour. Previously, research into the effect of wind on solid and liquid fuelled fires has been performed [37, 60 - 62]. The wind is found to affect both the fuel regression rate and the heat transfer processes occurring in the fire.

There are many conflicting studies on the effect of wind on fuel regression rate. Blinov and Khudyakov [44] initially found up to a 40 % increase in fuel regression rate as wind speed across a 1.3 m diameter fire increased from 0 m/s to 3 m/s. The measured flame temperature also increased with the wind speed. This was thought to correspond to better mixing and more complete combustion occurring within the fire itself. The increase in the efficiency of combustion was expected to increase radiative flux to the fuel surface with consequent increase in fuel regression rate.

In agreement with the results of Blinov and Khudyakov, fuel regression rates have also be observed to increase with increasing wind speed in 20 m diameter JP-8 fires [63], 4m diameter gasoline and diesel oil fires [49] and 1m diameter hexane fires [1]. In all cases, the increased wind speed was thought to affect mixing at the base of the fire and convective mass

transfer of vapour near the fuel surface. This increased the overall efficiency of combustion and radiative intensity in the fire, all contributing to the increase in fuel regression rate.

Babrauskas [52] used the results of Blinov and Khudyakov to propose a mass burning relationship that included the effects of wind speed, pool diameter and mass burning rate under quiescent conditions [Equation 2.5].

$$\frac{\dot{m}''_{windy}}{\dot{m}''_{still}} = 1 + 0.15\frac{U}{D} \qquad [2.5]$$

In this equation, U is the wind speed, D is the diameter of the pool fire and $\frac{\dot{m}''_{windy}}{\dot{m}''_{still}}$ is a ratio of the mass burning rates in windy and quiescent conditions. However, equation 2.5 was not derived with extremely high wind speeds in mind. Data from Blinov and Khudyakov [44] extended to wind speeds up to 25 m/s, at which point the fuel regression rate had leveled off after previously increasing with increasing wind speed. This suggests that the wind speed has an effect on the fuel regression rate up to a maximum wind speed where increasing the speed further no longer has any tangible effect.

Burgess et al [29, 55, 56] found that as wind speed increased, the fuel regression rate approached the value R_∞, the value expected for a fire of infinitely larger diameter. This proved particularly true in the smaller diameter fires included in their tests. It was thought that the wind caused the fire to become more emissive, resulting in the exponential term from equation 2.1, $e^{-\kappa D}$ to approach 0. This proved true for hexane, methanol and benzene fires up to diameters of 1.22 m. In the case of benzene, the fuel regression rate approached to within 15 % of R_∞ at a

wind speed of 4 m/s. Tests with methanol and hexane also approached fuel regression rates equal to R_∞ but never exceeded them.

A study was performed to determine the heat flux distribution across the surface of a 20 m diameter JP-8 fire under varying wind speeds. At a low speed of 1.3 m/s, an area of lower heat flux developed at the center of the pan in an area that had become starved of oxygen. When the wind speed was increased to 2.2 m/s, this zone shifted downwind of center and became smaller in extent; however, the measured heat flux was more than double that found in the same zone at 1.3 m/s. At 2.2 m/s and 5.1 m/s winds, two zones of increased heat flux formed, one at the windward and the other at the leeward edges of the pan. The increase in flux at the windward edge was thought to be caused by the proximity of the flames to the fuel surface. At the leeward edge, the increase in heat flux was due to the development of two downwind counter-rotating vortices that followed the central axis of the fire plume [48, 64]. These vortices, which are characteristic in large diameter fire plumes in cross winds, acted to entrain surrounding air, resulting in good mixing, combustion and a high temperature region of gases re-radiating heat back into the pan. Numerical simulations based on these experiments estimated the convective heat flux contribution into the fuel surface at 10% that of the radiation contribution.

The trend of increasing fuel regression rate with increasing wind speed is by no means universally supported by results in the literature. In fires up to diameters of 3 m, there is contrasting evidence that fuel regression rate sometimes decreases with increase in crosswind speed. Apte, Green and Kent [67] recorded a 25 % decrease in fuel regression rate in a 1m diameter aviation fuel fire as the wind speed increased from 0.5 m/s to 2 m/s. Using fixed-quantity pans of 0.9 m and 3 m in diameter and JP-5 as their fuel, Capener and Alger [2] measured decreasing fuel regression rates as the wind speed increased. Careful examination of

data recorded by the load cells that were used to measure the mass of fuel in the pans indicated that the mass was decreasing more on the leeward than on the windward side of the pan. It was thought that this was a result of different radiative heat flux levels to different parts of the pan due to changes in view factor caused by the tilt of the flame in the wind. For a range of diameters between 0.3 m and 0.6 m and wind speeds up to 2.1 m/s, Welker and Sliepcevich [66] found that the fuel regression rate in fires fuelled by various fuels (including n-hexane, methanol and acetone) decreased with increasing flame tilt. Once again, it was thought that under differing wind conditions, the view factor of the fire changed the heat flux distribution across the fuel surface leading to an overall reduction in fuel regression rate.

There have been some experiments performed to investigate the behaviour of pan fires in crosswind that also incorporate a floor built around the pan burner. In direct contrast to the trend seen for fires with a floor under zero wind conditions, fuel regression rates in fires in crosswinds decrease compared to values when the floor is not present [44].

Lip height was previously seen to be another important factor in determining fuel regression rates in fires; no consistent trends have been observed that relate wind speed, lip height and the presence of the floor.

Overall, there is very little agreement between different experiments that have been conducted to examine the relation between wind speed and fuel regression rate. Even very similar experiments conducted under similar wind speeds have produced drastically different results. Therefore, additional research is required in order to fully understand the phenomena that govern the behaviour and fuel regression rates in fires under differing crosswind conditions.

2.5 Objects in Fires

Both experimental and computational studies have been performed to investigate the effect of objects in or near pool fires, in both crosswind and quiescent conditions. Neill, Walker and Sliepcevich [68] examined heat flux from methanol and JP-4 pool fires of 0.3 m to 0.6 m diameter to a 0.11 m diameter, 0.23 m high, water-cooled cylinder. Overall, they found that the heat flux to the object increased with fire diameter, but decreased with time as a layer of soot formed on the surface of the object. They had difficulty in obtaining reproducible results which they felt was due to the fire being too small to fully engulf the cylinder.

Russell and Canfield [69] studied heat flux to a 0.22 m diameter; 0.31 m long stainless steel cylinder placed at a height of 1.2 m above the centre of a 2.4 m by 4.9 m JP-5 fire and aligned with the longer side of the pan. There were problems maintaining full flame engulfment on the object. A crosswind measured at 0.45 m/s caused a slight flame tilt which resulted in asymmetrical heat flux to the surface of the object with the highest heat flux recorded on the bottom leeward side of the object.

Unlike the studies of Neill, Walker and Sliepcevich [68] and Russel and Canfield [69], more recent experiments have focused on industrial or transportation accident scenarios and studied heat flux to thermally massive objects within the fires [3, 71 - 73]. One series of tests involved a 1.4 m diameter, 6.4 m long steel pipe placed inside, and 0.9 m above the surface of, a 9.1 m by 18.3 m JP-4 fire [66, 67]. Additionally, four small cylinders were placed within the fire, each measuring 0.2 m long with diameters of 0.1 m or 0.2 m. These cylinders were oriented in the same fashion as the pipe, with their longitudinal axis parallel to the longer side of the fuel pan. Ambient winds of up to 2 m/s resulted in changes to the time varying heat flux to these

objects [71]. As was seen previously [73], the bottom of the pipe experienced the largest heat flux while the top experienced the least heat flux [69]. The leeward side experienced more heat flux than the windward side due to flame tilt caused by the ambient wind. Variation in heat flux along the rest of the surface of the pipe corresponded to the thickness of the flame at particular locations, with areas that were constantly exposed to flame receiving more heat flux than areas which were only intermittently covered.

Using a 7.2 m diameter JP-8 fire, similar experiments were performed using a 1.2 m diameter, 4.6 m long steel pipe placed 1 m above the fuel surface and oriented with its long axis perpendicular to the ambient wind direction [70, 73]. Wind speeds measured between 0 and 2 m/s in these tests. It was thought that a recirculation zone formed on the leeward side of the pipe when the wind was strongest [70]. This increased local mixing of fuel and air resulting in higher measured heat flux on the bottom leeward side of the pipe. During the experiments, the wind died down; under this condition, nearly equal heat flux was measured on the windward and leeward sides. This also caused the emissivity of the flame beneath the pipe to decrease according to the heat flux results from locations beneath the pipe. This decrease in emissivity was believed to be evidence of the formation of a fuel rich vapour zone, deprived of oxygen, directly under the pipe [70], which was also not receiving as much heat flux from the fire. This has been seen before in fire scenarios with crosswinds and under quiescent conditions [38, 63].

There was no attempt to characterize the interaction between the wind, the fire and the cylindrical object in the fires in the above-mentioned experiments. One experiment did investigate this relationship [4, 69]. An 18.3 m long steel culvert with a diameter of 3.66 m was placed at a height of 0.6 m above the surface of the fuel on the leeward side of a 20 m diameter JP-4 pool fire. The culvert was oriented so that the wind first blew over the pan burner and then

over the longitudinal side of the culvert. During identified steady-state periods, the wind speed varied between 3 m/s and 10 m/s. The fire was heavily influenced by the strength of the wind. At wind speeds up to 3 m/s, the fire stayed on the windward side of the culvert. As wind speed increased to 8 m/s, the fire traveled around the culvert and elevated temperatures were recorded on the leeward side as well as the windward side. A vapour-rich-zone formed between the fuel surface and the center of the windward side of the culvert suggested that not enough oxygen could reach this area for combustion to occur, due to the interaction between the flames and the object. This vapour-zone also extended under the culvert in some cases [69].

As the wind speed further increased to 10 m/s, the flame traveled under and attached to the downwind side of the culvert. Elevated temperatures on the lower windward side of the culvert suggested flame impingement in that region. Heat flux to the fuel surface was greatest directly under the culvert [4] suggesting a region of intense mixing and combustion in that region. Just upwind were multiple vapour zones, indicating that some areas were still starved of oxygen. The fire plume exiting from underneath the culvert was very turbulent, characterized by multiple column vortices. These vortices were thought to increase entrainment and mixing in the plume, resulting in the highest temperatures and heat flux on the leeward side of the culvert. Measured values of heat flux were more than double those at the surface of the fuel and higher than those recorded in any similar study [5, 69, 70, 72]. The fuel regression rate decreased overall, which is suspected to be caused by the redirection of the flames away from the surface of the fuel [4] and towards the object by the ambient wind, changing the geometric view factor from the fire to the fuel surface. Overall, this suggests that the increased mixing and entrainment brought on by the crosswind turbulence may reduce formation of vapour-rich zones and increase

the heat flux of the fire due to more oxygen being available for combustion not only in the fuel pan but also in the fire plume after it has left the pan..

Overall, there is no doubt that an object greatly affects the behaviour of a fire, whether or not the object is engulfed in the fire and whether the object is thermally massive or small compared to the fire. The object greatly affects the amount and distribution of air entrained into the fire and therefore changes the intensity and burning rate of the fire. This can be offset by increased entrainment into the fire plume due to the formation of recirculation zones and other turbulent flow structures created by the presence of the object.

This section demonstrates that if the relationship between the fuel regression rate of a large pool fire and different crosswind and blocking object scenarios is to be further explored, many different contributing factors need to be considered in order not to overlook anything. A properly characterized crosswind is important so that the local velocity and turbulence conditions are known throughout the test enclosure. The physics of a pool fire and the resulting heat transfer modes occurring within the fire, particularly radiation, are also very important in determining the behaviour of a pool fire. The presence of a blocking object can drastically change fire behaviour and its location compared to the fuel pan will greatly influence the fire plume itself. In the subsequent chapters of this thesis, these factors will be explored in order to examine their effect on the fuel regression rate of the pool fire.

Chapter 3

Experimental Methods

Two series of large-scale pool fire experiments were conducted in various crosswind conditions. The first series of experiments involved 23 tests performed with a blocking object placed downstream of the pool fire. The second set involved 9 tests with the same pool fire and wind conditions but without the blocking object. The main difference between tests was the magnitude of the crosswind velocity.

This chapter documents the instrumentation used for measuring crosswind velocity, fuel regression rate, and heat flux during the experiments. The general layout and instrumentation used for each of the two series is also described. The instrumentation is significantly different in the second series of experiments as they encompassed a wider variation in crosswind speed, as well as a different setup around the fuel pan. Where applicable, the theory and justification behind both the setup and instrumentation used is also discussed.

3.1 Large-Scale Pool Fire Experimental Facility

This section presents a general overview of the University of Waterloo Live Fire Research Facility (UWLFRF) where the pool fire experiments were conducted. Details of the wind generation system and the design of the fuel pan are discussed.

3.1.1 Test Enclosure

Figure 3.1 presents a layout of the University of Waterloo Live Fire Research Facility. The pool fire experiments were performed in the test enclosure to the left of the diagram. The test area measured 19.5 m long by 15.4 m wide by 7.6 m high at the walls and 12.6 m high at the central peak in the roof. The gabled roof and the walls of the enclosure were made of corrugated steel. The main control room was located beside the test area and contained the controls for the fans and the five video cameras that monitor the test enclosure, as well as the computers used for data acquisition. An underground pit located at the centre of the test enclosure and six underground conduits routed under the floor to the control room provided a convenient path for routing the data cables to the computers in the control room. The four floor drain trenches in Figure 3.1 contained data acquisition equipment and power and data signal cabling and protected it from the extreme temperatures of the fire.

A right-handed coordinate system was defined for the test area of the UWLFRF (Figure 3.1). The origin of the coordinate system can be seen in the figure, located at the midpoint of plenum exit at ground level. The positive x direction is the direction of the main flow, the positive y direction is away from the control room and the positive z direction is vertically upward from the floor.

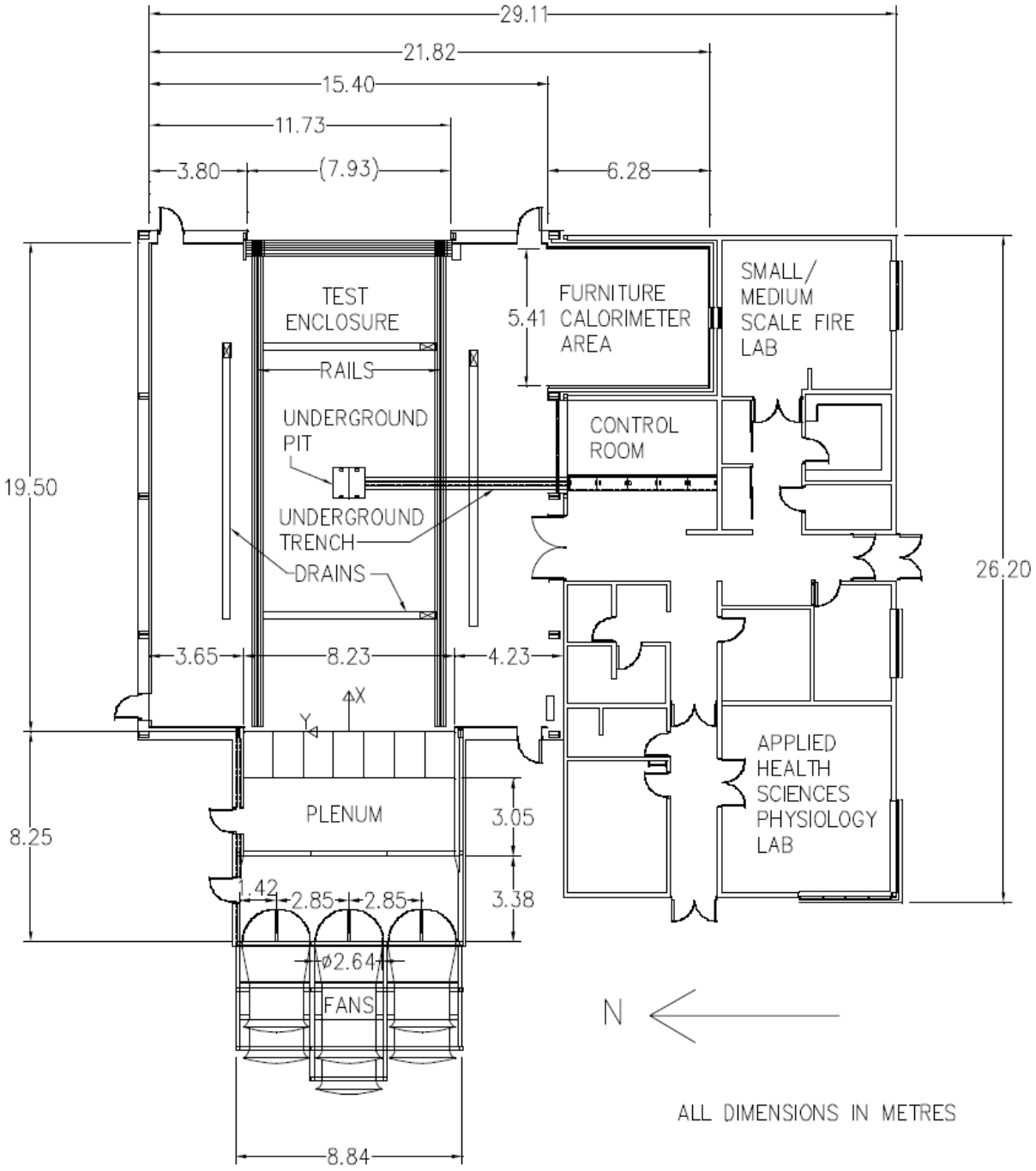

Figure 3.1 Floor Plan of the University of Waterloo Live Fire Research Facility [8]

3.1.2 Wind Generation System

Crosswinds were generated in the test enclosure by the wind generation system. This system was composed of six, 1.98 m diameter, Howden-Buffalo Model 78-26 Series 1000 vane-axial fans arranged two high by three across. An inlet bell and duct extension were installed upstream of each fan. The duct extensions were of different lengths with the middle fans having the longest extensions to prevent them from being starved for air by the adjacent fans. The middle fan was positioned on the centre of the inlet and the outer fans were centered 2.85 m from the centre of the inlet. The centre of the lower bank of fans was 1.27 m above the floor and the centre of the upper bank of fans was 4.27 m above the floor. The fans were rated to generate 78.7 m^3/s at 413.5 Pa with an efficiency of 72 % and a brake horsepower of 100 hp. This translated into a top crosswind velocity of approximately 13 m/s. Each fan was equipped with thirteen stators and sixteen blades to help minimize the rotational velocity in the exit flow, as well as a 1.83 m evasé, a back draft damper and an expansion joint at the outlet. The rotational speed of each fan was controllable using independent variable frequency drives which range from 0 to 60 Hz. Five distinct frequency settings were used in these experiments: 15, 22, 34, 47 and 60 Hz, which translate to crosswind velocities of nominally 3.0, 4.6, 7.1, 10 and 13.5 m/s respectively. Due to the different experimental configurations reported in this thesis, the wind speed will be discussed further in the results section.

The fans discharged the crosswind flow into a plenum before it entered the main test enclosure. The plenum was 8.23 m long by 8.54 m wide by 5.9 m high and contained flow straighteners in the form of two settling screens and an array of rectangular steel ducts. The screens were 3.6 and 3.8 m away from the fans respectively, with a total porosity of 78%. Each screen was made of 0.0032 m galvanized steel wires with a 0.029 m mesh. The screens were

fastened for support to each side of a large "X" structure formed by two diagonal struts with their centres located 2.86 m above the floor. This height was close to the top of the bottom bank of fans. The steel ducts were arranged in an array that is five high by seven wide. Each duct was 1.18 m high by 1.18 m wide and 1.83 m in length in the direction of the flow. The centre of the flow straightening duct array was approximately 0.29 m off the true centre of the crosswind facility in the positive y direction. At the outlet at the far end of the enclosure, the wind exited to atmosphere through a 7.9 m by 7.9 m sectional door, which was always fully open when the fans were in operation.

Each fan was attached to a Cutler-Hammer WF2C5075-OD Sensorless Vector Drive located in the mechanical room adjacent to the plenum. Each three-phase, 575 VAC, variable frequency drive could put out up to 77 Amps of current to a fan, providing a constant torque up to 100 hp and 55 kW. The power and variable frequency of each drive was set using by a Cutler-Hammer EKP enhanced keypad mounted in the control room, which allowed simultaneous control and monitoring of crosswind conditions directly from the test area.

There were several features of the UWLFRF that affect the overall crosswind flow patterns through the test area. These are briefly noted here with further information available in [11].

The furniture calorimeter area shown in Figure 3.1 measured 5.4 m by 6.3 m by 3.6 m and was located adjacent to the east end of the test enclosure. A large tarp covered the opening to this room during testing to minimize any undue influence on the flow through the test enclosure.

A large natural gas heater not shown in Figure 3.1 was installed on the west wall at the north side of the test enclosure to heat and protect the equipment and water pipes from freezing during the winter. This unit was 2.92 m off the ground and measured 1.98 m by 1.18 m by 0.91 m. Past testing indicated it has some effect on the flow conditions on that side of the enclosure [11].

Figure 3.2 The Burn house during a live fire test

As can be seen in Figure 3.2, an 8.8 m by 7.6 m by 7.4 m steel two-storey burn building is situated just outside of the outlet door of the main test enclosure. This burn house, which is used to simulate house fires in a controlled wind environment, rode on railway tracks allowing it to be moved up to 3.7 m beyond the outlet of the test enclosure. Figure 3.2 shows the position of the burn house for the current experiments; the smoke visualizes the blockage effect and influence that it has on the exit flow from the enclosure.

3.1.3 Fuel Pan

The fuel pan used in the experiments, shown in Figure 3.3, was 1.97 m in diameter. It was located with the leading edge 5.0 m from the outlet edge of the rectangular steel ducts in the plenum. The centre of the pan was located at y = 0. The pan base was made of 0.0048 m thick stainless steel and the sides of 0.002 m thick stainless steel. As installed, the top edge of the pan was 0.28 m above the floor. A triangular frame was welded to the bottom of the pan to minimize distortions due to liquid loading and thermal stresses that occur during the experiments. This frame was constructed of an outer triangle of 0.051 m square stainless steel tubing, and an inner triangle of 0.025 m square stainless steel tubing. This configuration also allowed three load cells to be placed at the tips of the outer triangles, which provided one method to measure the fuel regression rate. The fuel pan was placed in an overflow tray to contain any fuel or water from escaping in the event of a boil over. Concrete blocks and firebricks were placed around the pan which created a 2.7 m by 2.7 m raised platform, which sat level with the top edge of the pan. The blocks and bricks were placed no closer than 0.005 to 0.01 m from the side of pan to allow room for distortion of the pan during a fire and so that they would not interfere with the measurement of the fuel regression rate [10]. This configuration simulated a fire occurring at ground level.

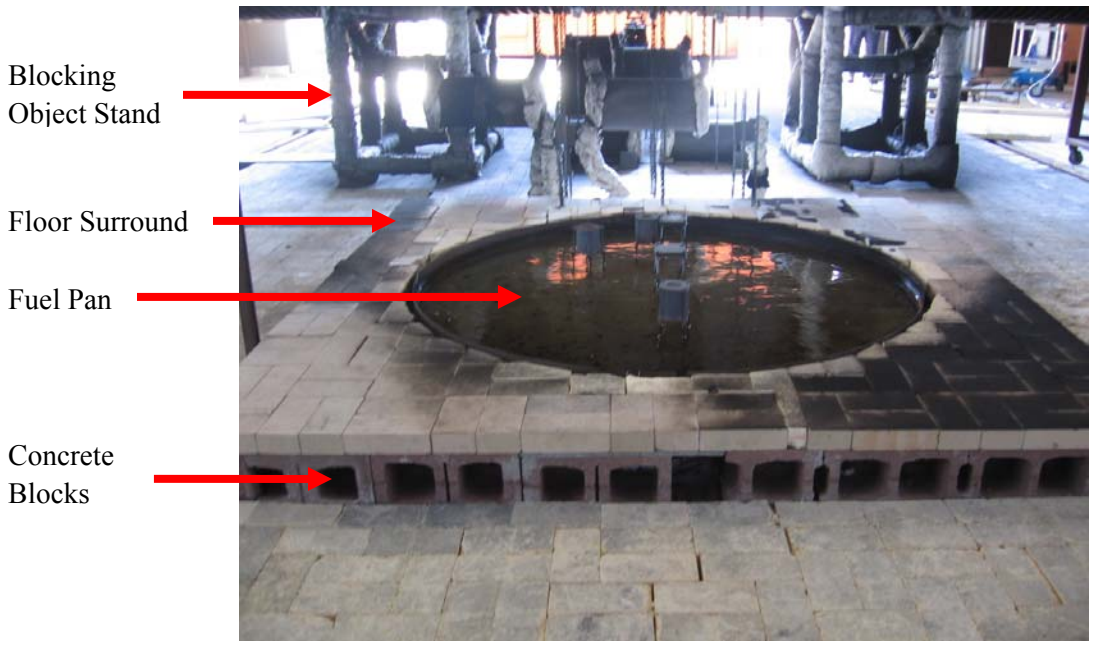

Figure 3.3 View of the bricked fuel pan during the Test Series with a blocking object present

In order to protect the concrete floor of the test enclosure from the intense heat of the fire, the area around the fuel pan was covered in layers of firebrick (Figure 3.3). While some fire brick was laid upwind of the pan, the majority was laid downwind and in the path of the fire plume. The rest was placed to the sides of the fuel pan. Depending on the series of experiments, a different configuration of bricks was used. The configuration of bricks used for the first series of experiments with a blocking object is shown in Figure 3.3. Of note is the configuration of cinder blocks that allow air cooling and flushing of the underside of the pan. This was necessary to minimize the potential for build up and later ignition of heavy fuel vapours that might have accumulated in the regions beneath the pan and the brick platform.

For the second series of experiments when the blocking object was removed, the bricks around the pan were rearranged as shown in Figure 3.4. Instead of placing fire brick to protect the floor from extreme temperatures, durarock sheets were placed upwind of the fuel pan burner while the firebrick was laid downwind of the pan in the path of the fire plume.

Figure 3.4 View of the bricked fuel pan during the test series without a blocking object present

3.1.4 Fuel

For each test, the required amount of fuel was floated on top of 320 L of water, forming a layer approximately 0.102 m thick. This absorbed heat from the fire and resulted in less thermal stress on the pan burner. Most tests in these experiments used only half of a drum (102.5 L) of fuel, resulting in a fuel layer 0.0325 m thick and a freeboard (lip) height of 0.0435 m. The pan burner could also accommodate tests with a full 205 L drum of fuel , and in that case the

freeboard height would be 0.011 m but as of yet no tests have been conducted with this quantity of fuel. In each case, the lip minimized the potential for boil over or spillover during the fire test.

The fuel used in all the tests reported in this thesis was Jet A, a kerosene based fuel used in the commercial aviation industry. Its composition and main thermo physical properties are listed in Table 3.1. It has very similar chemical properties to the military fuel JP-8.

Table 3.1 Physical Properties of Jet A aviation fuel [8, 10]

Density (288 K)	775 - 840 kg / m^3
Boiling Point	433 K - 573 K
Flammability Limits (% vol. by air)	0.7 - 5
Flashpoint (ASTM D56)	311 K
Vapour Pressure	1 kPa @ 311 K
Kinematic Viscosity (253 K)	8 mm^2 / s
Net Heat of Combustion	42.8 MJ / kg
Composition	
Aromatics (% vol)	max 25
Sulphur, Total (% wt)	max 0.30
Sulphur, Mercaptan (% wt)	max 0.003

3.2 Instrumentation

In both series of experiments, it was of interest to characterize the overall behaviour of the fire and the fire plume under different crosswind conditions. This was accomplished using a combination of fuel regression rate, velocity, temperature and heat flux measurements in and around the fuel pan. The main instrumentation used for these experiments is discussed in this section. The two methods utilized to measure fuel regression rate are discussed first. The

methods used to measure velocity including turbulence, are described next. Heat flux measurements, especially those inside the fuel pan, are discussed next, followed by temperature measurements in and around the fuel pan. Finally, the system used for measurement of the ambient conditions and the data-acquisition system for all instruments are discussed.

3.2.1 Fuel Regression Rate Measurements

The fuel regression rate is an integral piece of data when characterizing pool fires. It can be used with crosswind and heat flux data to form a more comprehensive picture of what is occurring in the fire. Key features of the two main fuel regression rate measurement methods used in this work - load cells and a sight glass - are outlined in this section.

Three load cells were used, one placed under each corner of the large triangular support structure under the fuel pan. These load cells were used to measure the weight of the fuel burnt during a test, which then were converted to a measurement of the fuel regression rate. Since the load cells were so close to the fire, they were wrapped in thermal insulation to protect them from the heat. The wires, protected by fire brick, were routed under the pan towards a nearby trench, and then an Ethernet cable transferred the signal to the data acquisition system. In order to level the load cells and the pan together, each load cell had three 1.0 cm x 2.5 cm bolts with locking nuts screwed into the six holes provided by the manufacturer. The pan was leveled before each test by partially tightening the locking nuts. In Test Series 2 through 4, the load cells used were Sensotec model 43A load cells. Each can carry a maximum load of 454.5 kg, with a 0-10 VDC signal linearly proportional to the load. In Test Series 5, one of the load cells was switched to an Omega model LCHD-1K, which had similar characteristics to the Sensotec model that it

replaced. The voltage signals from each cell were transformed into corresponding values of mass using calibration factors supplied by the manufacturer after which the values of the three cells were summed. The weight of the pan plus the water in the pan was subtracted from the measured values, leaving the weight of the fuel remaining in the pan. The surface area and density of the fuel were then used to determine the height of fuel in millimetres (mm) as a function of time throughout the test.

A second measurement of fuel regression rate was made using a sight glass. The sight glass consisted of a burette attached to the side of the fuel pan, positioned under the fluid surface via a piece of copper tubing and a swage-lock on one of the drainage caps in the pan. Once the tubing was far enough away from the heat of the fire, the copper tubing was attached to 1 cm polyethylene tubing with another swage-lock. The polyethylene tubing ran under the fire bricks for further thermal protection, then was fed through a gap in the door leading to the control room and down into the trench under the control room. It was attached to the bottom of a clear glass burette clamped to a ring stand which was carefully positioned such that the fluid level in the burette corresponded to the fuel level in the main pan and remained at a readable level during a fire test. Air bubbles had a tendency to collect inside the tubing; therefore, before each test any air bubbles were cleared from the tubing.

The fluid level in the burette was recorded using a video camera during each fire test. Markings on the burette run from 0 at the top to 21 at the bottom. The burette was placed against a white background and backlit. Red food colouring was added to the fluid in the burette to increase contrast and facilitate recording for later analysis. For tests with a blocking object, the video camera used Hi-8 film, but for tests with the blocking object removed, the video camera used a flash memory card to record the fluid level.

The video recording of the fluid level for each test was analyzed using Videocube [75] to determine the fuel regression rate over time. This method was previously used by Randsalu [10]. Each frame of the video is manipulated into a space-time image cut through the burette markings and a graph of the fluid level versus time is created. The markings on the burette are used as a scale of distance on the video with the 30 Hz framing of the video in order to accurately measure the fluid regression rate [75]. Since the fluid in the burette was coloured water, the regression rate calculated by this method must be divided by the specific gravity of the fuel to represent the true regression rate of the fuel.

3.2.2 Velocity Measurements

The velocity field in the UWLFRF was characterized in order to track the thermal plume of the fire [8,9] and to correlate crosswind velocity with changes in fuel regression rate for this work. Two horizontal bars were fitted with bidirectional probes, each having its own accompanying thermocouple. One of the probe rakes was made to withstand fire plume conditions. This is known as the 'hot flow probe rake'. The other had more distance between bidirectional probes and thermocouples. It was designed to measure wind speeds under ambient temperature conditions and was known as the 'cold flow probe rake'.

Bidirectional probes were selected for general velocity measurements in the studies because of their low cost, ease of alignment, thermal and mechanical robustness and resistance to clogging from debris [11]. Sixteen bidirectional probes were used on each probe rake. In the first series of tests, the probes on the hot flow probe rake were spaced every 0.33 m from -2 m to 3 m along the y-axis. In the second series of tests, the probes were redistributed to span from -2.33 m

to 2.66 m on the y-axis, keeping the same 0.33 m spacing as in the first experiments. The thermocouple mounted near each bidirectional probe provided the local temperature data needed to determine density and, hence, velocity at that position. The bidirectional probes on the cold flow probe rake were spaced differently, spanning from -4.65 m to 4.65 m along the y-axis, with approximately 0.62 m spacing between each probe.

The bidirectional probes were attached to Setra Model 267 diaphragm-type pressure transducers. On the hot flow probe rake, the attachments were made with brass tubing, whereas on the cold flow probe rake PVC piping was used. Like the bidirectional probes, the pressure transducers were chosen for their durability, their acceptable accuracy and their flexibility to provide high-scale and low-scale pressure ranges. There were two transducers for each probe; one was a high-pressure transducer with a measuring range of ± 250 Pa, the other was a low-pressure transducer with a measuring range of ± 25 Pa. Each transducer outputs a signal in the range of 0 to 10.4 VDC. Using these tandem transducers, the probes can accurately measure wind speeds between 2 and 20 m/s in the dominant flow direction. While the high pressure transducer measures a large range of velocities, it suffers from poor accuracy (± 25 %) at low speeds [11]. The low-pressure transducer has good accuracy throughout its range, but can measure a maximum velocity of only 6.5 m/s, one half the maximum velocity of the wind generation system. Thus, for wind speeds up to 6.5 m/s, the signal from the low pressure transducer was used; over 6.5 m/s, the signal from the high pressure transducer provided the desired velocity measurement.

Each probe rake was 12.2 m long and mounted on a stand consisting of two 6.4 m tall vertical poles made of schedule 40 steel pipe with a diameter of 0.11 m. This allowed vertical travel from 0.3 m to 6 m off the ground, allowing measurement of radial profiles of velocity at

multiple heights in a given cross-section of the facility. The horizontal beam was made of 12 gauge square steel tubing, which was double layered in the middle to provide more rigidity and reduce sagging of the beam. Pipe clamps were fitted around each vertical pole and attached to the horizontal bean to maintain stability, allowing the beam to travel vertically while still constrained horizontally in the x and y direction. Each pole was attached to a steel base plate on 4 castors via a flange. Each base was weighted, with four outriggers, and leveling feet to make the assembly less prone to vibrations or other movement while the fans were on [11]. A hand winch attached to the base and pulleys attached to the top and the base of each vertical pipe were used to change the height of the horizontal beam.

Attached to each end of the horizontal beam, outside of the vertical poles, were instrumentation panels which contained a data acquisition backplane, as well as the pressure transducers for bidirectional probes on that side of the horizontal beam. For most experiments, the pressure transducers for the first eight probes (-2 m to 0.33 m on the y-axis), were attached to the panel on the negative y side and the second eight probes (0.66 m to 3 m on the y axis), were attached to the panel on the positive y side. However, for the second series of experiments, the farthest bidirectional probe on the positive y-axis (3 m) was moved to a position at -2.33 m on the y-axis. Therefore, for the second series of experiments, nine probes were connected to the instrumentation panel located on the negative y-axis, and the remaining seven probes were connected to the instrumentation panel on the positive y-axis side. The panels were insulated in ceramic blanket insulation to ensure that any sensitive electronic equipment would not be exposed to thermal loading from the fire plume during the tests.

3.2.3 Turbulence Measurements

The bidirectional probe rake facilitates measurement of mean velocity across a set of horizontal profiles, but does not have a high enough sampling rate or spatial resolution to allow turbulence measurements or measurement of any velocity component besides that in the dominant flow direction. These additional measurements are important, however, to define boundary conditions and realistic flow parameters for computer models of the spill fires in the UWLFRF. The measurement of turbulence quantities in a large scale experimental facility like the UWLFRF is relatively difficult since it is desired to characterize the velocity in all three directions simultaneously at at least one location at a time and at a sampling rate that can resolve mid-scale turbulence fluctuations in the flow. Cup, pressure, or windmill anemometers are not appropriate because they measure mean wind velocity and do not have sufficient spatial or time resolution for turbulence measurements. Although Laser Doppler anemometer (LDA) systems are available and do have sufficient temporal and spatial resolution, this method is not appropriate because of the necessity for seeding the flow throughout a very large area in the facility. It is limited by the difficulty of traversing an LDA system from point to point across such large areas. Hot wire anemometers are too fragile for the dust laden environment of the UWLFRF [77]. Particle Image Velocimetry (PIV) can be applied to measure velocity over a large area; however it suffers many of the same problems as LDA since the measurement area must be seeded and the seed particles illuminated for accurate PIV results. PIV has been used to measure velocity at multiple locations over areas as large as 1 m^2 but measurement at this large scale suffers from difficulties with seeding and signal intensity and the interpretation of measurements taken over even 1 m^2 adjacent areas in a large facility like the UWLFRF would be very challenging [78].

Given the limitations of the above velocity measurement devices, a sonic anemometer was chosen to provide three-dimensional velocity and turbulence measurements in this study. Although still limited in time and spatial resolution, and constrained to measurements at a single location, the sonic anemometer is cheaper than PIV, LDA or hot wire anemometer systems and perhaps most importantly, it is much more rugged for use in live fire experiments in the large test area at UWLFRF.

A sonic anemometer works by sending ultrasonic pulses from a transmitting to a receiving head in the device. The time each pulse takes to pass between the heads correlates directly to wind speed [79]. Multiple heads allow measurement of wind speed in two or three dimensions. Simultaneous measurement of the temperature of the flow to determine air density allows instantaneous calculation of the speed of sound which improves the accuracy of the final velocity measurements. Unfortunately, the sonic anemometer cannot match an LDA or a hot wire anemometer in terms of sampling rate or measurement resolution. The maximum sampling rate for sonic anemometers can be as high as 200 Hz, in comparison to hot wire anemometers or LDA, which can sample at thousands of Hz. While the faster devices allow for measurement of the smallest scales of turbulence, this sort of time resolution is not required for the turbulence measurements in this work. In terms of spatial resolution, the measuring heads of the sonic anemometer create more of a flow disturbance than either a hot wire anemometer or the non intrusive LDA and PIV methods. When properly placed however, this disturbance can be minimized so as to have little effect on the final velocity measurements.

Figure 3.5 The CSAT 3 sonic anemometer [79]

The sonic anemometer selected for these experiments was the Campbell Scientific CSAT3 sonic anemometer shown in Figure 3.5 [79]. It measures the instantaneous speed of sound as well as the wind speed along three non-orthogonal axes, which are then converted into wind speeds in the x, y, and z directions. Unlike other sonic anemometers, it self-corrects for variations in the local speed of sound due to crosswind effects. The CSAT3 has a measurement path length of 10 cm vertically by 5.8 cm horizontally with a maximum sampling rate of 60 Hz, somewhat slower than the fastest sonic anemometers on the market. The transducer head is large, 47.3 cm long by 42.4 cm high and 1.59 cm wide, but was oriented in such a way as to minimize the overall disturbance to the flow. The transducer, powered by 10 VDC, is attached to an

electronics box by a 2.13 m cable, then to the data logger running custom CSAT3 software by a 22.86 m RS-232 cable. Due to the extra cable length required to facilitate CSAT3 velocity measurements at many different locations in the UWLFRF, this cable is actually longer than the recommended length of 15.24 m. After consultation with Campbell Scientific [80, 81], it was determined that this extra length would not affect the accuracy of the measurements. The CSAT 3 has a maximum measurable velocity of ± 65.33 m/s along the flow direction, with four distinct automatic ranges. In the vertical direction, assumed to be perpendicular to the flow, the maximum measurable wind speed is ± 8.19 m/s. These are both well within the expected measured velocity values at the UWLFRF.

The CSAT3 was purchased after the first series of experiments with the blocking object and therefore was only available for the second set of experiments without the blocking object. Velocity measurements were made at two different points in the facility, taking care to keep the measurement head at temperatures below its 50 ° C recommended maximum operating temperature [79]. The first position provided preliminary measurements of turbulence boundary conditions on the crosswind flow entering the test area during a fire test and the second was to characterize turbulence during cold flow measurements in the facility with no fire present. During live fire tests, the CSAT3 was placed on a tripod upwind and to the side of the fuel pan, at y = -3.54 m, 0.81 m downwind of the plenum outlet and 1.77 m above the ground. This corresponded to the vertical centre of the second row of grids above the floor, and the centre of the farthest column in the grid in the – y direction. It was positioned more than 1m away from any solid surfaces, to eliminate interferences that might introduce error into the velocity measurements [79].

For the cold flow tests the CSAT3 was placed between the eighth and ninth bidirectional velocity probes on the probe rake, approximately on the center plane of the facility. Measurements were made at several vertical locations and planes downwind of the fans. Specifically, the CSAT3 was placed at x = 2 m, 5 m, 11 m and 15 m at heights between z = 1 m and 6 m off the ground, increasing the height by 0.33 m for each measurement. To counterbalance the added weight of the probe and electronics on the velocity probe rake, and to reduce vibrations of the rake, unistrut supports were attached to the probe rake and clamped to one of the support poles of the existing unistrut frame for each set of measurements. This reduced vibration and allowed for improved measurement of both the mean wind speed and turbulence characteristics.

3.2.4 Heat Flux Measurements

Complementary to the measurement of fuel regression rate of the fire under different crosswind conditions is the measurement of heat flux to the fuel in the pan burner. The heat flux gauges used inside the fuel pan in these experiments are the Hemispherical Heat Flux Gauge (HFG) and the Directional Flame Thermometer (DFT). More details on other heat flux gauges (i.e. Gardon gauges) as well as a more general heat flux measurements and discussion on heat flux in the fires of interest in this thesis are available in Lam [8, 9].

Sandia National Laboratories in the United States developed the HFG as an instrument for performing heat flux measurements in pool fires. The time-temperature history of a thin metal plate in this gauge is used to deduce steady state heat flux to the surface of the gauge, using a dynamic thermal model [82]. The advantages of using an HFG are that the thermal

analysis model is well validated [82], and the gauge, while not being prohibitively expensive, is designed to survive inside a pool fire.

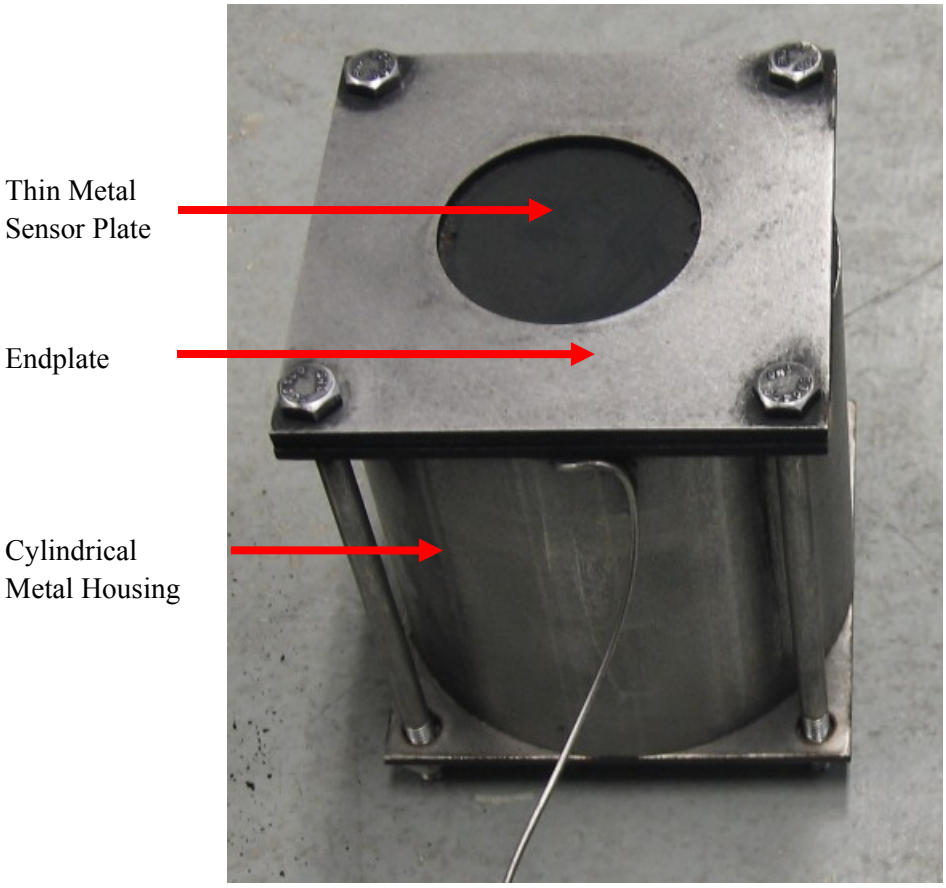

Figure 3.6 A fully assembled HFG

Figure 3.6 shows a photograph of the HFG. The thin metal sensor plate of the gauge is of 0.00025 m thick stainless steel shim-stock, cut into a square measuring 0.102 m in each direction. The endplate, a 0.0032 m thick steel square of the same size as the sensor plate, has a 0.05 m diameter hole centered on it to expose a portion of the sensor plate to the incident heat flux. The exposed part of the sensor plate is painted with Pyromark paint, rendering it a diffusive

grey surface. A back plate, which is the same size as the end plate, attaches to the top of the 0.102 m diameter cylindrical steel body of the HFG. Insulation is placed on top of and beneath the sensor plate to isolate the sensor plate surfaces from the rest of the HFG. The cylindrical body is also filled with Fibrefrax blanket insulation cut into 0.102 m diameter circles. A flat plate of the same size as the plate at the top of the gauge is placed on the bottom of the HFG and the entire assembly is bolted together with four 0.14 m assembly bolts. The thin metal sensor plate of the gauge is assumed to be exposed to a one-dimensional heat flux, as all other sides are insulated. A single 0.0016 m diameter Inconel sheathed type-K thermocouple is spot welded to the back of the sensor plate using small 0.0001 m thick retaining straps and is used to record the time evolution of the plate temperature which, in turn, is employed to calculate the incoming heat flux.

One issue that has been encountered with live fire heat flux measurements using the HFG is conductive losses in the housing of the HFG decreasing the accuracy of the results [83]. Transmission of heat flux data from the thin sensor plate into the gauge housing is assumed to be a one-dimensional process, but in reality there are considerable losses, with conduction inside the gauge being the main source of error. During steady-state testing with a known incident heat flux, the HFG recorded 35 - 48 % less heat flux than the more well established Schmidt-Boelter gauge [83].

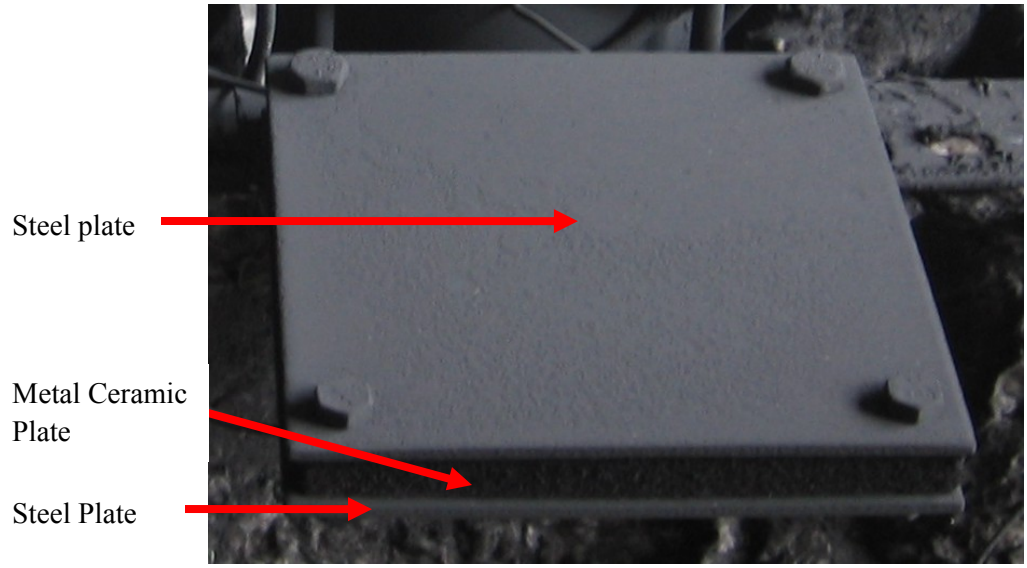

Figure 3.7 A DFT heat flux gauge covered in soot after a fire test

The DFT, shown in the Figure 3.7, was originally developed by AEA technologies in the United Kingdom in order to estimate flame thickness in pool fires by calculating an 'effective radiation temperature'. It has since been adapted by Sandia National Laboratories for use in large pool fires [84]. The double-sided version, which measures the heat flux in two opposite directions, was used in these experiments. When placed in the pan at a position slightly above the surface of the fuel, a DFT can measure the heat flux onto the fuel surface, as well as the heat flux reradiated from the surface of the fuel. Similar to the HFG, the DFT uses a time-temperature history as input into an inverse heat conduction program called IHCP1D to calculate the transient heat flux [85].

The DFT gauge consists of a sandwich construction of a plate of 0.11 m thick metal ceramic between two 0.0016 m thick steel plates. A thermocouple is mounted to the back of each plate to measure the temperature time history of that plate. The back of each plate is insulated so the front of the plate reaches thermal equilibrium with the environment on that side of the plate.

When negligible convection is assumed, the temperature measured by the thermocouple is approximately equal to the black body temperature that corresponds to the heat flux incident on that side of the DFT [6]. If convection effects are important, DFT correction factors can be used to correct measured values of heat flux [7]. One issue with the DFT is that the time lag of the thermocouple, combined with the thermal mass of the plate and thermocouple and contact resistance between the thermocouple and the flat plate, can cause errors in the heat flux measured using a DFT.

Even though the DFT is not as accurate in mixed heat flux environments due to convective losses, testing suggests it is more accurate than the HFG in these scenarios. During steady-state testing with a known incident radiative heat flux, the DFT recorded within 12% of the heat flux recorded by the more well established Schmidt-Boelter and Gardon gauges [83], whereas the HFG recorded 35 - 48 % less heat flux than the two well established gauges as mentioned in the previous section.

In each fire test, HFGs and DFTs were mounted in the fuel pan to record the heat flux onto the pool surface as well as the heat flux from the surface of the fire upwards. The location of these heat flux gauges differed depending on the configuration of the test enclosure. During the first series of experiments with the blocking object involved, three HFGs and two double-sided DFTs were positioned in the fuel pan among other measuring instruments, as seen in Figure 3.8.

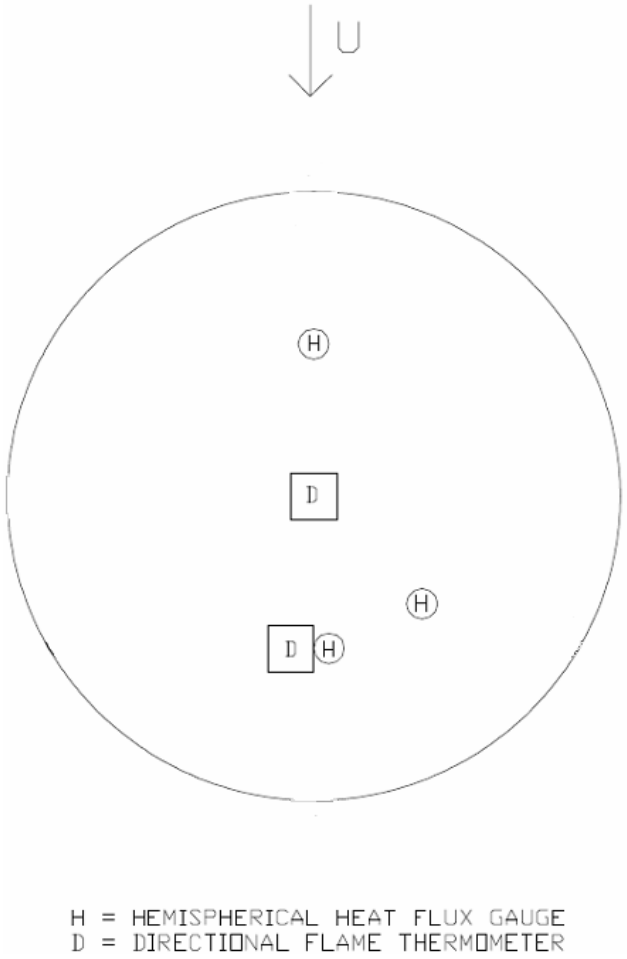

Figure 3.8 Arrangement of heat flux gauges in the pan during the series of tests with the blocking object present [8]

As can be seen in Figure 3.8, the first HFG was placed 0.48 m upwind of the center of the pan on the mid-plane of the test enclosure and 0.27 m above the base of the pan. The second HFG was placed 0.49 m downwind of the center of the pan, at an angle of 45 degrees from the mid-plane of the facility on the +y side of the y-axis and it was 0.269 m above the base of the pan. The last HFG was placed 0.51 m downwind of the center of the pan, 0.08 m away from the

mid-plane of the facility on the +y side of the y-axis. It was 0.271 m above the base of the pan. The first DFT was placed directly on the pan center, 0.267 m above the base of the pan. The second DFT was placed 0.51 m downwind from the center of the pan, 0.05 m away from the mid-plane of the facility on the -y side of the y-axis and 0.268 m above the base of the pan.

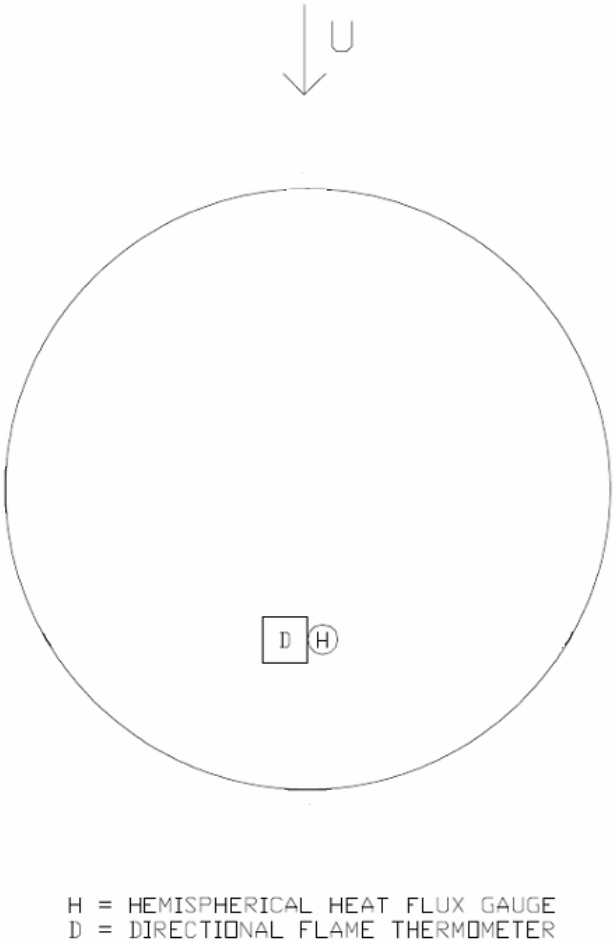

Figure 3.9 Arrangement of heat flux gauges in the pan during the series of tests without a blocking object present [8]

In the second series of experiments with no blocking object, only one HFG and one DFT were placed in the pan, as seen in Figure 3.9. The HFG was placed 0.5 m downwind of the center of the pan, 6 cm away from the mid-plane of the facility on the +y side of the y-axis and at a height of 0.262 m from the base of the pan. The DFT was also placed 0.5 m downwind of the center of the pan, 0.07 m away from the mid-plane and at a height of 0.262 m from the base of

the pan. Justification for the locations of these HFG in all the experiments can be found in Lam [8].

3.2.5 Thermocouples

Characterization of the temperature field in the fire, fire plume and other parts of the experimental facility was an extremely important part of these pool fire experiments. Thermocouples are the most viable temperature measurement device in fires [38,51,69,72,86 - 88]. Therefore, in these experiments temperatures were measured using 24 gauge (0.00051 m diameter) Type K thermocouples with Nextel ceramic fibre insulation and Inconel braiding. Local temperature is measured at either an intrinsic junction, when the thermocouple is mounted on the blocking object, or at an exposed junction when located elsewhere in the experimental facility. For thermocouples directly downwind of the pool fire in either setup, blanket insulation and metal sheathing were used to increase the survivability of the thermocouples.

3.2.6 Weather Station

Ambient conditions outside of the test enclosure during an experiment, especially the prevailing winds, can affect both the crosswind flow and the fire plume development. Therefore, two separate weather stations were used to monitor prevailing ambient conditions. The first, a solar powered Wireless Vantage Pro2 Integrated Sensor Suite (ISS), shown in Figure 3.10, measured the wind speed and direction, humidity, barometric pressure, rainfall and temperature [89]. This weather station was purchased after the first series of experiments with a blocking

object was completed and therefore, data is only available for the second set of experiments without the blocking object. It was placed 65 m upwind of the crosswind fan intakes. This location was selected so the fans, as well as any large buildings, would not interfere with the measurements. The temperature and humidity sensor are 2 m above the ground, and the 3 cup anemometer with a wind vane is placed slightly higher at 2.4 m. Data was sent via a Wireless Vantage Pro2 Repeater, to the Vantage Pro2 Console and data logger. For the present experiments, the Console was set to its maximum data recording rate, once a minute.

Figure 3.10 The Wireless Vantage Pro2 Integrated Sensor Suite [89]

The other weather station used in these experiments was operated by the Region of Waterloo. It is a Campbell Scientific model HMP45C, situated approximately 185 m north of the

ISS. Ambient temperature and humidity are recorded by this station at a height of 2 m above the ground, while the wind speed and direction are recorded at a height of 10 m. Data from this station was used to verify and check the consistency of data recorded by the ISS.

3.2.7 Data Acquisition

The National Instruments Compact Fieldpoint data acquisition system was used for all the experiments reported here. The Fieldpoint system collected data from a series of backplanes, each with up to eight data modules which in turn could each measure eight signals. Different modules are used for the thermocouple readings and the analog signals. In each case, the raw signal was converted to a digital signal via a 16-bit analog to digital converter before being sent to the data acquisition system. Digital transmission of the signal greatly improved the final signal to noise ratio on all channels. In the first series of experiments with the blocking object, 448 channels of data are collected; 344 of them dedicated to thermocouple signals and 104 of them dedicated to analog signals. The system collected data at a rate of 1 Hz and refreshed data at a rate of 0.88 Hz.

In the second series of experiments without the blocking object 486 channels of data were collected; 444 dedicated to thermocouples, and the remaining 42 dedicated to analog signals. Due to the increased number of channels being sampled during these tests, the sampling rate decreased to approximately 0.4 Hz. This was the maximum sampling rate possible using the existing data acquisition system without encountering problems in the quality of the data.

3.3 Large-scale Pool Fire Tests

3.3.1 Test Setup

The fire and instrumentation layouts used in the two different large-scale experimental test series conducted for this thesis are described in this section. During live fire tests with the blocking object present, the blocking object itself took up a sizeable portion of the test enclosure, so the instrumentation was positioned on and around the blocking object. In contrast, for the layout of the second series of experiments, the blocking object was removed while keeping the fuel pan in the same location. The additional room after removal of the blocking object necessitated a change in the layout of the instrumentation, as discussed later in this section. An alternative configuration of the layout with no blocking object included an extension of the floor surround upwind of the fuel pan, moving the step increase in floor height farther away from the actual fire. This will be discussed later in this section.

3.3.2 Layout of the Test Series with no Blocking Object Present

For this series of experiments, the blocking object was removed and in its place, chains of thermocouples were hung from two open cage frames made of unistrut (Figure 3.11). Chains were hung in seven rows progressively farther from the fuel pan, at 7.5 m, 8 m, 9 m, 10 m, 12 m, 14 m and 15.2 m downwind of the plenum. The first row consisted of seven chains spaced 0.5 m apart on the y-axis, with the fourth chain centered on the fuel pan. These rows of thermocouples were close enough to the fuel pan to be of importance to this thesis. The thermocouples on each

of the front row of chains were spaced apart vertically from z = 0.14 m to z = 1.5 m. Each chain was then secured to the ground to prevent movement during a fire test.

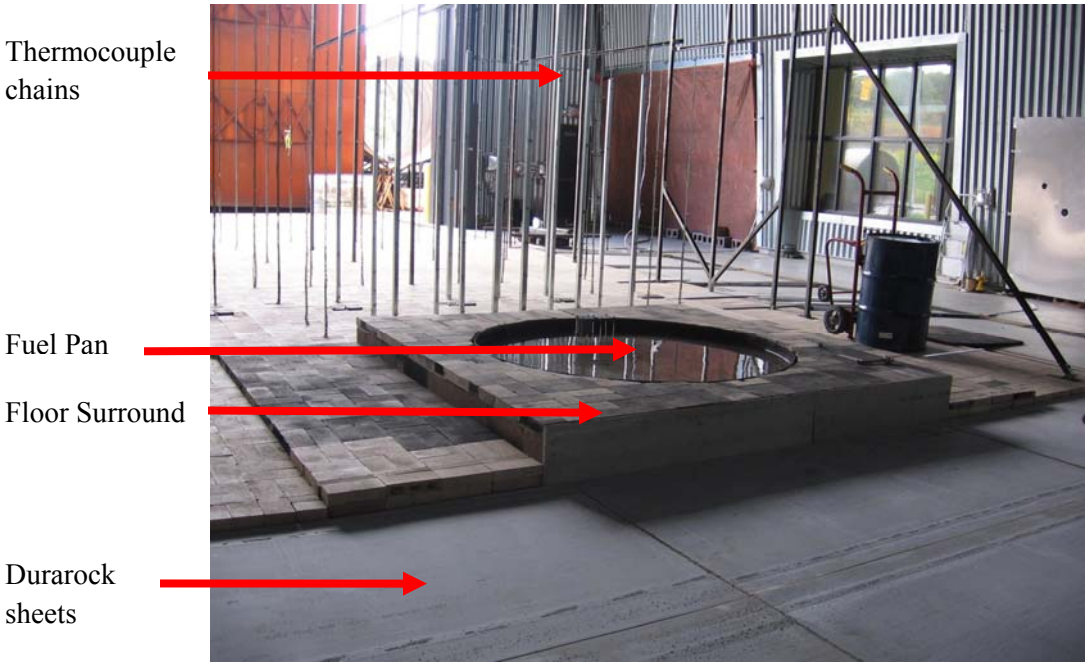

Figure 3.11 The fuel pan and the thermocouple chains during the test series with no blocking object present

Figure 3.11 shows a visual representation of the thermocouple chains and cage frames. Each cage frame was bolted to the ground and then the two were bolted together to make the whole assembly sturdier. In front of the cage frame, two diagonal unistrut pieces ran along the x-axis towards the plenum and were bolted into the ground to further prevent the cage from moving towards the plenum. Behind the cage, cables were attached to the facility and secured to the cage to finish bracing the entire assembly. Since each piece of unistrut is 0.0413 m thick and the cage is never thicker than two pieces of unistrut stacked together, the cage does not provide a significant amount of blockage to the flow.

At the very back of the facility, just above the top of Figure 3.11, was the bidirectional velocity probe hot flow rake at x = 15 m. The height of the rake was adjusted depending on the fan speed of the test (Table 3.2). The relationship between the fan speed and wind speed in the test enclosure will be explored in the next chapter.

Table 3.2 Bidirectional probe rake heights and fan speeds of the test series with no blocking object present

Test	Rake Height (m)	Fan Speed (Hz)
36	3	22
37	3	34
38	3	22
39	1	47
40	4	15
41	1.5	34
42	1	47
43	1.5	34
44	3.5	15

This description does not represent all of the instrumentation present during these experiments without a blocking object; instead it focuses on that which is most relevant to the present results. For a complete description of the setup of the series of experiments without the blocking object present refer to Lam [8].

3.3.3 False Floor Configuration of the Test Series with no Blocking Object Present

In the series of experiments without the blocking object present, a new configuration of floor was also tested. The ground plane around the pan was extended towards the plenum outlet

in order to move the step on the leading edge of the floor surround farther away from the fuel pan (Figure 3.12). It was suspected that turbulent structures generated by this step could greatly affect the fire, therefore this new configuration (the "false floor" configuration) was used in an attempt to determine the effect, if any, of the forward step. The false floor was 2.7 m long and 5m long created by sheets of durarock concrete board suspended on pieces of wood lying on top of cinder blocks. This configuration still allowed full air cooling and ventilating of the underside of the pan, while moving the step increase in floor height well upwind of the pan.

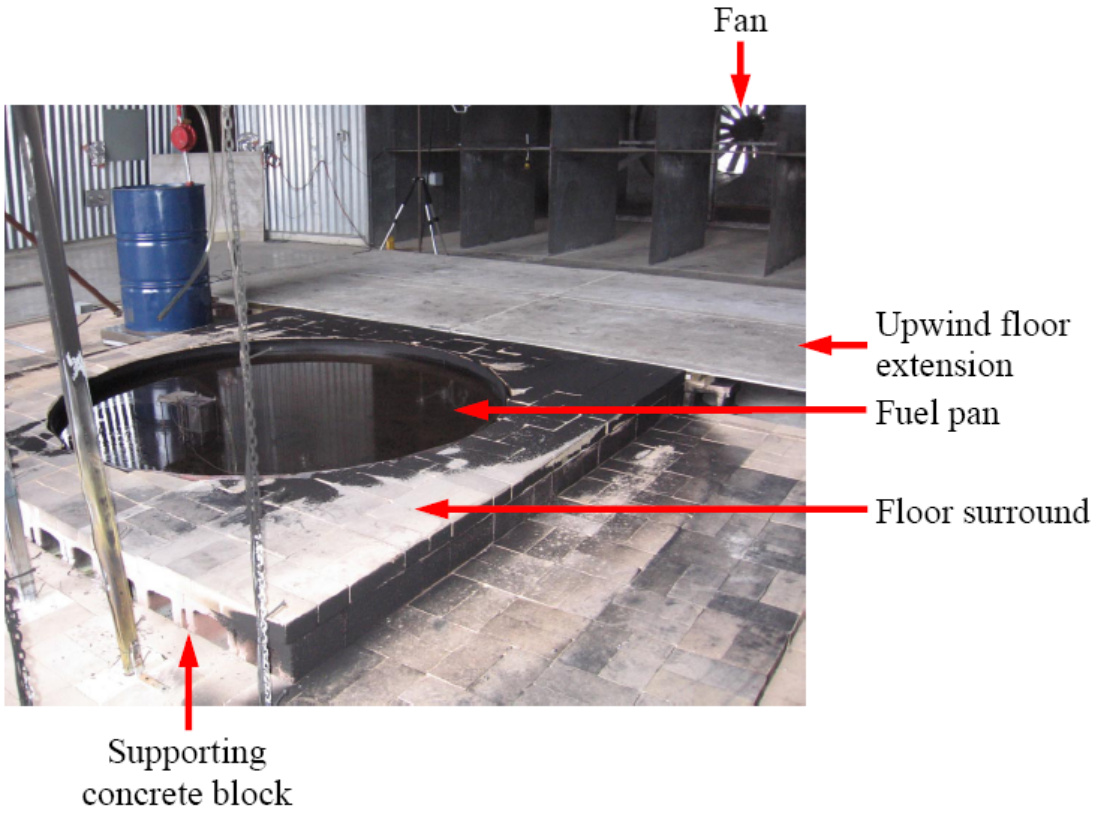

Figure 3.12 The 'false floor' Upwind Floor Extension next to the fuel pan [9]

3.3.4 Layout for the Test Series with a Blocking Object Present

A key feature of the layout for the series of experiments with the blocking object is the object itself as shown in Figure 3.13. It is a 10.7 m long, 2.7 m in diameter cylindrical object made of two culvert sections, one 4.6 m long and the other 6.1 m long, joined by a 0.68 m wide steel band. The windward edge of the object is placed 1 m downwind of the leeward edge of the fuel pan as shown in Figure 3.13. The culvert is mounted on four V-shaped stands such that the bottom edge is 1 m off the floor. The stands are designed to minimally interfere with the flow and protected from the heat of the fire by a layer of ceramic fibre insulation.

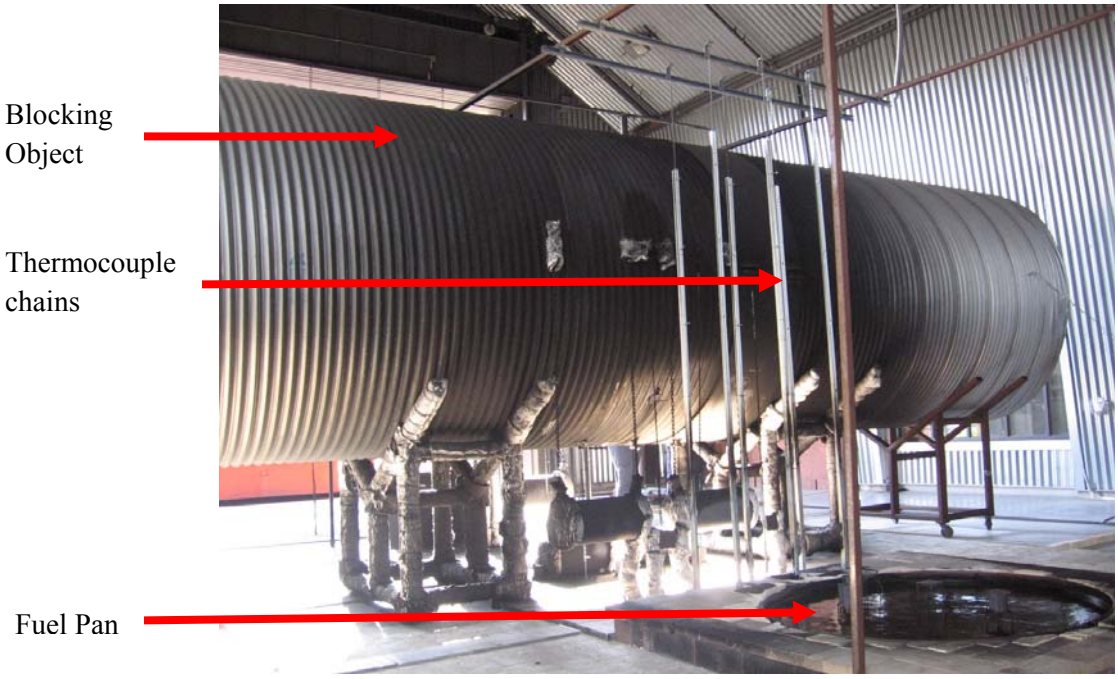

Figure 3.13 The fuel pan and the blocking object during the test series with a blocking object present

Thermocouples and heat flux gauges were mounted along the surface of the blocking object to observe local conditions around the blocking object. Large cylindrical calorimeters were hung off the side of the object exposed to the fire to investigate coupled radiative and convective heat flux to thermally massive objects. Chains of thermocouples were hung both in front of and behind the blocking object in order to record the temperatures inside the fire in front of the blocking object and to record the temperatures of the plume once it had passed the blocking object. Since this thesis is focused on interactions occurring in and near the fire, the only row of thermocouples examined are those closest to the fire, at x = 7.03 m. This row consisted of chains on the centre-line (y-axis) and 50 cm in each direction along the y-axis. The thermocouples placed in the chains varied in height from 0.3 m to just above 3m above the floor, in order to capture temperatures throughout the entire fire no matter what the prevalent crosswind conditions were. These chains are made visible in Figure 3.13.

The bidirectional probe rake was placed behind the blocking object at a distance of x = 15 m in order to capture crosswind data as it left the UWLFRF. The 'hot flow' probe rake was used and mounted at different heights depending on the speed of the fans (Table 3.3). For a more complete description of the setup of the first series of experiments with a blocking object present, refer to Lam [8], Randsalu [10] and Weisinger [11]. The fan speed and how it equates to the wind velocity will be presented in the next chapter.

Table 3.3 Bidirectional probe rake heights and fan speeds of the test series with the blocking object present

Test	Rake Height (m)	Fan Speed (Hz)
5	0.66	60
6	0.66	60
7	1.33	60
8	1.33	60
12	2.58	47
13	2.58	34
14	2.58	22
15	2.58	34
16	2.58	47
17	2.58	22
18	2.58	47
19	2.58	34
20	2.58	22
21	2.58	60
22	2.58	60
25	1.5	60
26	1.5	47
27	5.0	22
28	5.0	34
29	1.5	47
30	1.5	60
31	5.0	34
32	5.0	22

3.4 Calculations and Uncertainty

This section outlines details of the calculations and theory behind each of the measuring instruments, to provide insight into interpretation and analysis of the signals. Estimates of the bias and precision uncertainty involved in each measurement are also included.

3.4.1 Bidirectional Probes

Bidirectional probes operate on the principle of using measured stagnation pressure to determine the local raw velocity. The side of the probe facing the oncoming flow measures the true stagnation pressure, while the backside of the probe provides an approximate measurement of the static pressure in the probe wake. Since it is in the wake, the measured static pressure is lower than the static pressure of the flow field; however, conversely, the measured dynamic pressure will be higher as it combines with the static pressure to equal the stagnation pressure. In order to determine the true static and dynamic pressure, Weisinger calibrated each probe in the University of Waterloo main wind tunnel against a calibrated pitot probe [11]. The calibration factor, k, was determined as the ratio of the measured velocity (Equation 3.1) to the actual velocity, which is also equal to the square root of the ratio of the measured dynamic pressure and actual dynamic pressure(Equation 3.2) as density is assumed constant.

$$V = \sqrt{\frac{2P_{dyn}}{\rho}} \tag{3.1}$$

$$k = \frac{V_{meas}}{V_{actual}} = \sqrt{\frac{P_{dyn\,measured}}{P_{dyn\,actual}}} \tag{3.2}$$

A maximum bias uncertainty of ± 0.5 % was determined for all the probes when properly aligned in the flow [11]. A list of the calibration factors for each probe is available in Appendix A.

3.4.2 Pressure Transducers

The pressure transducers connected to the bidirectional probes were supplied with individual calibration certificates. Each certificate provided 11 known voltages and corresponding velocities, which were fit with a second-order best fit line to determine an individual equation relating the dynamic pressure, P, to the voltage output from the pressure transducer, V. These equations are found in Appendix B with typical equations for the high-pressure and low-pressure transducers in equation 3.3 and 3.4 respectively.

$$P = -252.6 + 50.36V - 0.03043V^2 \tag{3.3}$$

$$P = -25.38 + 5.245V - 0.02002V^2 \tag{3.4}$$

The coefficient of determination (R^2) for each equation is at most 0.0001 away from the ideal value of 1, with most equations being more accurate than that. Given the constraints of the large-scale experiments conducted in this work, these curve-fit equations are accurate enough to be used to calculate dynamic pressure. The dynamic pressure is then used with equation 3.1 and air density calculated using the local temperature and atmospheric pressure to calculate the uncorrected velocity. The uncorrected velocity is then divided by the previously determined calibration factor, k, to determine the corrected velocity. If the velocity is below 6.5 m/s, the dynamic pressure measurement from the low-pressure pressure transducer is used; otherwise, the dynamic pressure is found based on the signal from the high-pressure pressure transducer.

The calibration certificates for each pressure transducer included estimates of uncertainty due to hysteresis and non-repeatability. The maximum hysteresis effect was reported to be

0.10 % and uncertainty due to non-repeatability effects was reported as 0.05 % of the total pressure range. This level of uncertainty should allow repeatable wind velocity measurements.

Weisinger [11] performed a thorough uncertainty analysis combining the uncertainty values of each of the measurements required to determine velocity using the bidirectional probes. The bias and precision error are determined for each measurement and combined using the root-sum-squared (RSS) method outlined in Equation 3.5 [90].

$$\delta R = \sqrt{\frac{\partial R}{\partial x_1}\delta x_1 + \frac{\partial R}{\partial x_2}\delta x_2 + \ldots + \frac{\partial R}{\partial x_n}\delta x_n} \tag{3.5}$$

This method assumes that all errors are normally distributed. It was determined by Weisinger [11] that measurements made closer to the centerline were more accurate than those taken near the edges of the flow. This makes sense intuitively as the velocity fluctuates more towards the edges of the facility, wall effects become more prevalent and the mean wind speed decreases. For the majority of measurements, the maximum bias and precision error was found to be ±4.3%, mostly attributed to bias errors. For regions near the edge of the flow field, the maximum error is found to jump from ± 15 % to ± 45 %, prompting Weisinger to caution against using measurements from the edge region of the flow without significant caution in the interpretation of results [11].

The Campbell Scientific CSAT3 Sonic Anemometer was used to measure turbulence components of velocity aligned perpendicular to the mean flow direction. This device is calibrated at the factory before shipping and directly outputs corrected velocity data. According to the literature supplied by Campbell Scientific [79], errors in the measurements taken by the

CSAT3 include the offset error and the bias error. The offset error arises because it is assumed that the CSAT3 is oriented facing directly into the wind. Therefore, this error varies depending on the direction of alignment of the orthogonal axis. In the x and y direction, the error is less than ± 0.04 m/s while in the z direction this error shrinks to less than ± 0.02 m/s. The bias error also varies depending on the direction of the wind vector relative to the measurement axis of the CSAT3. In the present tests, the CSAT3 is mounted with its axis parallel to the floor of the test enclosure. It is assumed that the bulk of the wind also travels relatively parallel to the floor so that it is fair to assume that the wind vector is within 5 degrees of parallel to the CSAT3. The bias error is then less than ± 5 % of the velocity reading.

Using the CSAT3 sonic anemometer, it is possible to perform certain turbulence measurements during live fire tests as well as cold flow tests. The turbulence intensity is the main turbulence property measured during these experiments as it is commonly used during computer modeling. The turbulence intensity (I) in the dominant flow direction is calculated using the following equation. (Equation 3.6)

$$I = \frac{u'}{U} \tag{3.6}$$

In this equation u' is the root-mean squared of the turbulent velocity fluctuations and U is the mean velocity. The precision error of this measurement was calculated to be ± 1.2 % while the bias error is still less than ± 5% of the turbulence intensity reading, and therefore the total uncertainty of the turbulence intensity measurements is approximately ± 5.1 %.

3.4.3 Fuel Regression Rate

The fuel regression rate (FRR) is measured using the load cells under the fuel pan and the sight glass attached to the fuel pan. Each calculates the regression rate differently and therefore has differing sources of error.

Each load cell measures up to 454.5 kg; each 45.5 kg equates to a reading of 1 VDC from the load cell, once the voltage is corrected by calibration factors supplied by the manufacturer. Since there are 3 load cells under the fuel pan, the instantaneous total mass in the pan is represented by this equation (Equation 3.7) [10].

$$M = ((LC1 \times cal1) \times (LC2 \times cal2) \times (LC3 \times cal3)) \times \frac{454.5kg}{10V} \tag{3.7}$$

In this equation M represents the mass in the pan, LC1,2 and 3 are the voltage readings of the individual load cells and cal1, 2 and 3 are the calibration factors supplied by the manufacturer for each load cell, with a conversion from volts to lbs added at the end of the equation. This measured value includes the weight of the fuel, of the pan itself and of the water substrate in the pan. To determine the mass of fuel in the pan, Equation 3.8 is used.

$$M_{fuel} = M_{Panwithfuel} - M_{Panwithoutfuel} \tag{3.8}$$

The measurement of the weight of the pan and water without fuel is obtained from an ‘ambient’ trace at the beginning of every fire test. From the mass of the fuel, it is possible to determine the instantaneous height of the fuel in the pan using Equation 3.9.

$$H_f = \frac{M_{fuel}}{\pi r^2 \times \rho} \times \frac{1000mm}{1m} \tag{3.9}$$

This equation uses the measured mass of fuel from Equation 3.7 and divides by the circular area of the fuel pan and the density of the fuel to determine the instantaneous height of the fuel in the pan. The fuel height is then converted to millimetres since regression rates are most often reported in mm/min. The height of the fuel is graphed versus time resulting in a downward sloping line representing the burning of the fuel. After identifying the period of steady state burning from other sources (most often thermocouple traces in the fire plume itself) [8,9], the steady state fuel regression rate can be determined by calculating the slope of fuel height with time during the steady state period.

The sight glass was used as an alternate way to measure the fuel regression rate during large scale pool fire experiments. The water in the sight glass is directly connected to the water substrate in the fuel pan via the sight glass tubing. Depending on the amount of fuel on top of the water substrate, the level in the sight glass will change. This change in level is filmed throughout a test and used to determine the fuel regression rate.

Since the fuel used in this experiment is Jet A (Table 3.1), it has a different specific gravity than water and a correction factor is needed to determine the instantaneous level of Jet A fuel in the pan. The following formula is used to determine the fuel height in the pan based on a change in the level in the sight glass (Equation 3.10).

$$H_f = \frac{(B_i - B_x) * \frac{220mm}{21}}{S.G._{fuel}} \tag{3.10}$$

In this equation B_x represents the instantaneous burette mark (gradations are numbered 0 to 21 from the top to the bottom of the burette) aligned with the fluid level, while B_i represents the initial burette mark before fuel was added to the burner pan. The conversion factor of 220 mm over 21 converts the 21 burette markings into a vertical measurement in mm; with the total distance between mark 0 and mark 21 being 220 mm. The final result is divided by the specific gravity of the fuel to give the actual height of fuel in the pan. When this instantaneous height is placed on a graph versus time, a downward slope will appear when the fire is burning. In the same fashion as with the load cell results, the steady state burning time and the corresponding instantaneous heights enables determination of a steady state fuel regression rate.

Randsalu [10] performed an uncertainty analysis of the above two methods used to measure the height of the fuel in the pan. Using the RSS method, the uncertainty in the fuel regression rate measured using the load cells is ± 0.4 mm/min, while the measurement of fuel regression rate by the sight glass method was slightly more accurate, with an uncertainty of ± 0.3 mm/min.

3.4.4 Thermocouples

Throughout the test enclosure, type K thermocouples are used. These thermocouples are attached to the data acquisition system using modules specially designed to accept thermocouple

signals and convert the thermocouple voltages into temperatures. According to the literature [90], these thermocouples have an inherent bias uncertainty of ± 2.2 °C.

3.4.5 Heat Flux Measurements

Two different heat flux instruments are used in the fuel pan during these experiments. They are the heat flux gauge, known as the HFG, and the directional flame thermometer, known as the DFT. Calculations and uncertainty for each instrument are presented in this section.

The HFG was used to measure heat flux in the extreme conditions encountered near the fuel surfaces inside the pool fires. Calculations of heat flux from the thermocouple data for this gauge involve solving an idealized one-dimensional heat flux equation [84]; a heat balance on the sensor surface (Equation 3.11).

$$\alpha q_{surf}(t) = \varepsilon \cdot q_{rad}(t) + q_{conv}(t) + q_{steel}(t) + q_{insul}(t) \tag{3.11}$$

The term on the left hand side of equation 3.10, q_{surf}, is the desired heat flux value. The terms on the right hand side of the equation represent heat loss by re-radiation, convection, heat stored in the steel of the HFG and heat conducted into the insulation inside the HFG. For the analysis, the thickness of the plate is assumed to be 0.000254 m thick, the emissivity, ε, to be 0.85, the density and specific heat of the plate are those of 304 stainless steel and the insulation is 0.0076 m thick Kaowool blanket insulation. The whole equation is divided through by the absorptivity, α, then the right hand side terms are taken at time t_N and with a temperature at

location ι = 1, which corresponds to the surface of the sensor plate , $T_{\iota=1}$. The terms transform into the following equations.

$$\frac{q_{rad}(t_N)}{\alpha} = \frac{\sigma \cdot \left(T_1^N\right)^4}{\alpha} \tag{3.12}$$

$$\frac{q_{conv}(t_N)}{\alpha} = \frac{h(T_1^N - T_{amb})}{\alpha} \tag{3.13}$$

$$\frac{q_{steel}(t_N)}{\alpha} = \frac{\rho \cdot C_p\left(T_1^N\right) \cdot L}{\alpha} \frac{dT_1^N}{dt} \tag{3.14}$$

$$\frac{q_{insul}(t_N)}{\alpha} = \frac{k\left(T_{1+1/2}^N\right)}{\alpha} \cdot \frac{\left(T_1^N - T_2^N\right)}{dz_1} \tag{3.15}$$

The radiation term in this equation (Equation 3.12) is modeled using the Stefan-Boltzman law, where σ is the Stefan-Boltzman constant. The convection term (Equation 3.13) is based on a one-dimensional heat convection equation for which the heat transfer coefficient, h, must be calculated at the location of the gauge with the ambient fluid temperature and the flow conditions over the surface taken into account. The storage term (Equation 3.14) is modeled using a central difference formulation for the time derivative of the surface thermocouple temperature measurement. The thickness of the sensor plate is considered and the dependence of the specific heat and density on the local temperature are also modeled. A one-dimensional heat conduction equation with internal heat generation and temperature dependent properties is used to model heat transfer to the insulation in the gauge (Equation 3.15). Blanchat, Humphries and Gill [82]

obtained the insulation term relationship by considering the response of the surface of a thick wall subjected to a time varying temperature, when the back-side is perfectly insulated.

Blanchat, Humphries and Gill [82] performed careful experiments to validate their model for analysis of the heat flux to the HFG. They applied step inputs of radiant heat flux to the gauge and compared results to those from a calibrated and well-validated Gardon gauge. Sampling frequencies were also changed to determine their effect on the measured heat flux. Based on the results, an uncertainty model was proposed, including the effects of time lag seen throughout the validation experiments, as well as the incomplete model of the true heat balance on the gauge surface. The authors [82] determined errors on the order of ± 5 % for most applications; however, they suggested that any data collected be graphed first with uncertainty bars, to determine which data appears reasonable and which data might be discarded.

The DFT is also used to measure heat flux in the fuel pan during these Jet A pool fire experiments. Similar to the HFG, analysis of the temperature signals from the DFT is based on a one-dimensional inverse heat conduction analysis. Temperatures from the thermocouple inside the DFT are used as input into the one-dimensional inverse heat conduction analysis program, IHCP1D, by Beck Engineering [85] to determine surface temperatures on the gauge. The resulting surface temperature is approximately equal to the effective blackbody temperature, assuming that absorptivity equals emissivity and convective heat transfer is negligible or a small correction factor can be added [84]. (Equation 3.16).

$$\alpha Q''_{incident} = \varepsilon Q''_{blackbody} \tag{3.16}$$

Uncertainty analysis is still a work in progress for the DFT, but some preliminary work has been done. Keltner et al. have published several papers based on using DFTs as Furnace Characterization Units [84,91]. Since multiple steps are involved in calculating the heat flux to a DFT, it is difficult to determine the uncertainty associated with each element. Uncertainty as high as ± 25 % [84] has been estimated, but this is thought to be an overestimate due to three-dimensional effects and the low lateral heat transfer capability of the plate exposed to the fire. Other tests [84] estimated uncertainty as low as ± 3 % for the total heat flux over an hour long test, but this involved use of a cold-wall correction factor unique to the test performed.

3.4.6 Weather Station

Two weather stations are used for these tests. The first station, mounted upwind of the air intakes of the fans, is a Wireless Vantage Pro2 Integrated Sensor Suite (ISS), which measures barometric pressure, humidity, temperature, wind direction and wind speed. The signals from these transducers are sent to the system console and all calculations done internally prior to being recorded.

Each of these measurements has associated uncertainties. According to the manufacturer's specifications, the barometric pressure has an uncertainty of ± 0.8 mm Hg. There is a ± 3 % uncertainty in the relative humidity, unless the measured value is above 90 % relative humidity in which case the uncertainty raises to ±4%. The temperature probe has an uncertainty of ± 0.5 ° C. The wind speed has a variable uncertainty; it is either ± 1 m/s or ± 5 % of the reading, whichever is greater. The wind direction has an uncertainty of ± 7 °.

The second weather station, the Campbell Scientific model HMP45C operated by the region of Waterloo, does not have manufacturers listed uncertainty values. It is assumed however, that any values retrieved from this station would be at least as accurate as the ISS, therefore any uncertainties in measured values from the Campbell Scientific weather station will be assumed to be the same as the uncertainties for the same parameter from the ISS weather station.

Chapter 4

Results

4.1 Introduction

This chapter describes the results of the large scale wind characterization and crosswind fire experiments undertaken in this research. All were performed at the University of Waterloo Live Fire Research Facility. The discussion will focus on measurements of wind speed, both cold flow through the facility and during large-scale fire tests, as well as fuel regression rate and heat flux from the fire entering and leaving the fuel. As a first step, results of characterization of the cold flow in the facility (i.e., without a fire present) are presented, then the data used to determine appropriate inlet conditions for wind speed during live fire tests. Cold flow turbulence data is also presented to further describe the flow through the test enclosure. In terms of characterization of the fire, fuel regression rate data is examined and discussed, along with issues encountered during the regression rate measurements. This data is analyzed in concert with wind speed results to determine any relationship between the two, also taking into account the role of ambient conditions and their effect on measurements within the test enclosure. Turbulence data collected during the fire tests is presented next, to provide more details about the characteristics of the flow seen during fire testing. Heat flux data from the fuel pan is analyzed together with wind speed and fuel regression rate to examine the role of heat flux in determining the regression rate and the effect of the crosswind on the heat flux and therefore fuel burning rate, in the various crosswind fire situations. The combined results should lead to better understanding of the relationship between fuel regression rate, crosswind speed and heat flux to the fuel in the pan for fires in crosswind situations.

4.2 Wind Characterization

There have been two series of experiments conducted to characterize the cold flow inside the UWLFRF test enclosure using the bidirectional probe rake described in the instrumentation section of this thesis. Weisinger [11] conducted the first flow characterization measurements, with and without a Blocking Object, but only for the maximum wind speed generated by the fans. In this section, a second and more detailed series of wind characterization studies is presented, including mean flow distributions for 5 different wind speeds at several planes in the facility. Data include results taken with and without the presence of a Blocking Object, as well as turbulence measurements taken for each wind speed at select locations using the CSAT3 anemometer. Results from different tests at the same location will be compared to determine test to test repeatability. It was expected that differences will exist between the tests presented here and those conducted by Weisinger [11] since there were modifications to the wind generation system and the fire layout between these test series. When the building was constructed, baffle plates were attached to the fan outlets. These were intended to close and seal the fans during inclement weather. For the present tests, these baffle plates were secured in a fully open position in which they were aligned at angles of approximately ± 10 degrees from the vertical x-z plane down the center of each fan, whereas during tests reported in [11] the baffle plates were forced open to varying degrees by the flow through each individual fan. This affected the flow distribution and also introduced uncertainty as to the exact position of the plates during the earlier tests. In terms of changes to the fire layout, the fuel pan and a large unistrut cage were present and caused some flow blockage during the present wind characterization tests; whereas during the initial tests reported in [11], the test enclosure was completely empty.

4.2.1 Wind characterization without a Blocking Object present

Mean velocity distributions throughout the Facility were measured for five wind (fan) speeds: 3 m/s (15 Hz), 4.6 m/s (22 Hz), 7.1 m/s (34 Hz), 10 m/s (47 Hz) and 13.5 m/s (60 Hz). A grid of velocity measurements was made using the 16 probe rake of bi-directional velocity probes at vertical heights of between 1m and 4.8m, over four different y-z planes: positions x = 2 m, 5 m, 11 m and 15 m downstream of the test enclosure inlet. The first plane, x = 2 m, was the closest physical position to the flow inlet that could be accessed with the bidirectional flow rake. This can therefore be taken to represent inlet flow conditions for fluid flow modeling of the facility. The second plane, x = 5 m, is situated directly in front of the fuel pan burner and would therefore be indicative of the crosswind flow conditions in the immediate vicinity of the fire plume. Both positions, x = 2m and x = 5m, were also in front of the Blocking Object for tests reported in subsequent sections on wind characterization with the Blocking Object present. The final two measurement planes, x = 11 m and at x = 15 m, allowed characterization of the flow at positions downwind of the fire and, for the case of the Blocking Object, downwind of the object as well. Finally, the mean flow velocity distribution was characterized at all planes for two different floor configurations; “false floor configuration”, where the area in front of the bricks around the pan had been extended upwind using concrete sheets at the same height as the bricks, and the “no false floor configuration” where the upwind extension had been removed. Details of these configurations and their geometry are outlined in Sections 3.3.2 and 3.3.3. Velocity data measurement details and methods are also outlined in Section 3.2.2. Using the velocity data measured at the discrete probe locations throughout a given plane, velocity contour maps were constructed for that plane using the Kriging interpolation method [92]. This method had previously been shown to be appropriate for wind velocity data in the facility [11].

Figure 4.1 contains velocity contour maps taken for wind speeds of 3, 4.6, 7.1, 10 and 13.5 m/s at the location x = 2 m downstream of the plenum outlet, when there is no Blocking Object and no false floor in the facility. In each graph, there is a noticeable inner core region where measured velocities vary by several m/s at most, and an outer flow region where the velocity quickly decreases towards zero as the facility walls are approached. The flow within the inner core is relatively consistent from the facility inlet to the outlet, exhibiting large-scale characteristics which are a function of the geometry of the plenum and layout of the fan banks as discussed in more detail below. Flow in the outer region interacts with the layer of relatively quiescent air that lies external to the main crosswind outlet, i.e., between the edge of plenum outlet and the outer walls of the facility. Within the core flow area, there are several separate areas of elevated velocity. For example, at a wind speed of 3 m/s, four such areas can be seen as dark green areas: a small area in the upper left hand corner centered at y = -3.5 m and z = 4.2 m, a large area spanning the entire vertical measurement area at -2.5 m < y < -0.5 m, an area along the floor centered at y = 1 m and z = 1.5 m, and another large area spanning between 0.4 m < y < 3.9 m and from z = 1.1m all the way to the top of the measurement area. As the wind speed increases, these separate regions merge into two larger, more distinct areas of elevated velocity symmetric about the centerline of the measuring area. The elevated velocity regions are believed to be caused by the merging of the flows issuing from each of the six individual fans, and should become more evident downwind of this measuring location.

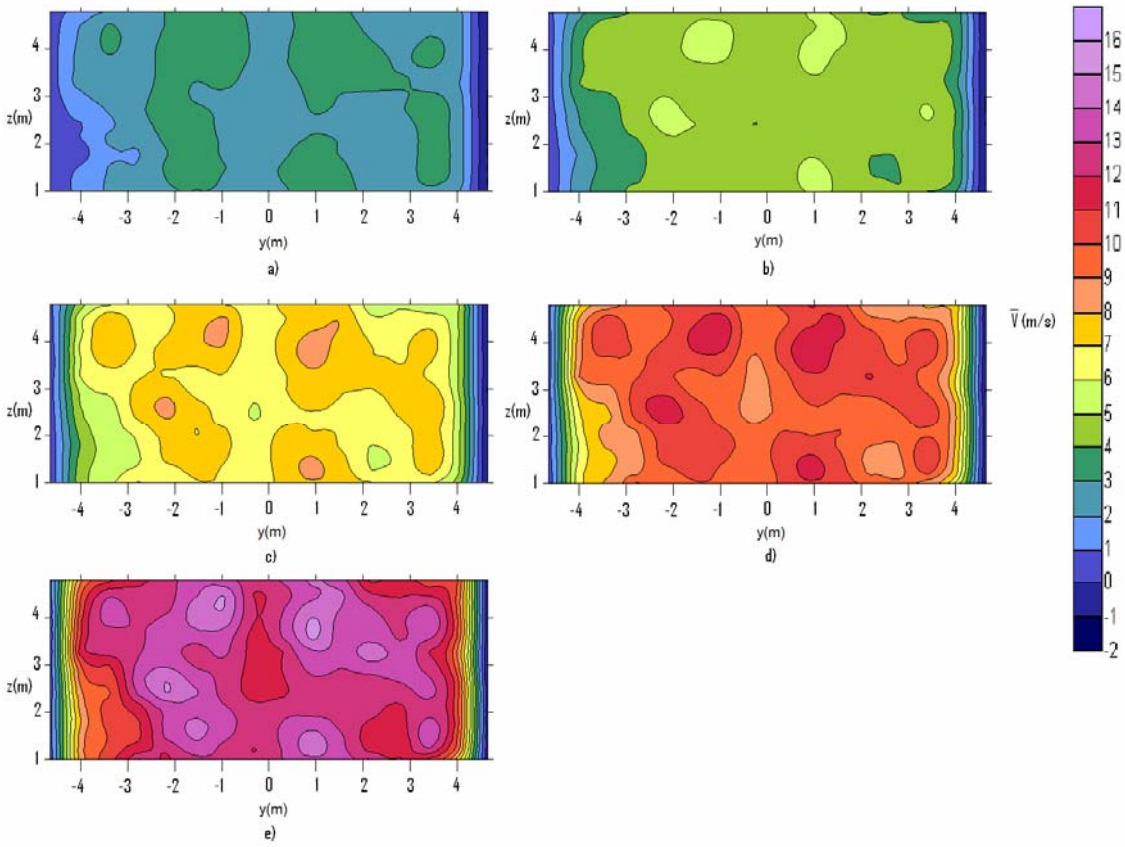

Figure 4.1 Velocity Contour Maps without a Blocking Object or False Floor present at x=2m with an average wind speed of a) 3.0 m/s b) 4.6 m/s c) 7.1 m/s d) 10.0 m/s and e) 13.5 m/s

In contrast, three areas of lower velocity exist within the inner core flow (Figure 4.1 d)): one area on the –y side near the floor of the facility, one between the upper and lower fan bank slightly to the -y side and a third near the facility floor on the +y side. As can be seen in the contour map (Figure 4.1), the first velocity depression on the –y side appears as an extension of the outer slower flow. This depression, initially centered at y = - 4 m and z = 2 m for a wind speed of 3 m/s, extends further towards the middle of the test enclosure with increasing wind speed, to about y = -3.5 m and z = 2 m for a 13.5 m/s wind speed. This velocity deficit was also seen in previous wind characterization measurements at the UWLFRF [11] at the highest wind speed. It is thought to be caused by the asymmetric expansion of the test enclosure downwind of

the plenum outlet. The outlet is offset so that there is more space between the edge of the outlet and the facility walls on the –y side, allowing increased flow expansion and more pronounced interaction with the quiescent layer of air along the walls on that side of the flow.

A second velocity deficit can be seen near the middle of each contour map, centered at y = -0.5 m and z = 2.5 m at a wind speed of 7.1 m/s. This depression persists, and becomes more marked, growing to span from 2.5 m < z < 4.5 m as wind speed increases. It is located in the middle of the "inner region" between the top and bottom centre fans and also in approximately the same location on the y-z plane as the middle of the 'X' formed by the supporting beams inside the plenum area, as mentioned in section 3.1.2. It is believed that this depression is an indication of an understandable flow deficit right in the center of the fan bank, superimposed over effects caused by the wake of the flow around the intersection of the supporting "X" beams in the plenum. A third velocity deficit is evident on the +y side, centered at y = 2.5 m and z = 1.5 m, first at a 4.6 m/s wind speed and persisting with increasing wind speed. This lower velocity region is located between two areas of higher velocity and the floor of the facility.

When examining these areas of elevated and depressed velocity, it is important to remember that the flow originates from six separate fans. In Figure 4.2, the perimeters of the fan outlets are superimposed on the contour maps at x = 2 m with no Blocking Object or false floor present. The areas of elevated velocity discussed above are almost all located either vertically or horizontally between two adjacent fan outlets. Since the baffle plates on each fan are oriented at an angle of ± 10 degrees from the vertical x-z plane that dissects the centre-line of each fan, this suggests that the high velocity flows from adjacent fans are being deflected outward by the baffle plates and merging together in the regions between the fan outlets. Areas of depressed velocity tend to coincide with the center of each fan outlet. This is consistent with expectations since an

area of lower velocity would be expected near the centre of the fan as the high velocity flow has been deflected laterally. It also supports the notion that the flows from the fans are merging together between adjacent fans. One area of depressed velocity that does not coincide with the centre of a fan outlet is the velocity deficit located in the middle of the measurement area. As discussed above, this region of lower velocity is likely caused by a combination of the middle fans being starved for air by the adjacent fans, causing a decrease in velocity at the center of the fan banks, as well as flow wake effects due to the cross support inside the plenum, which has been mentioned previously.

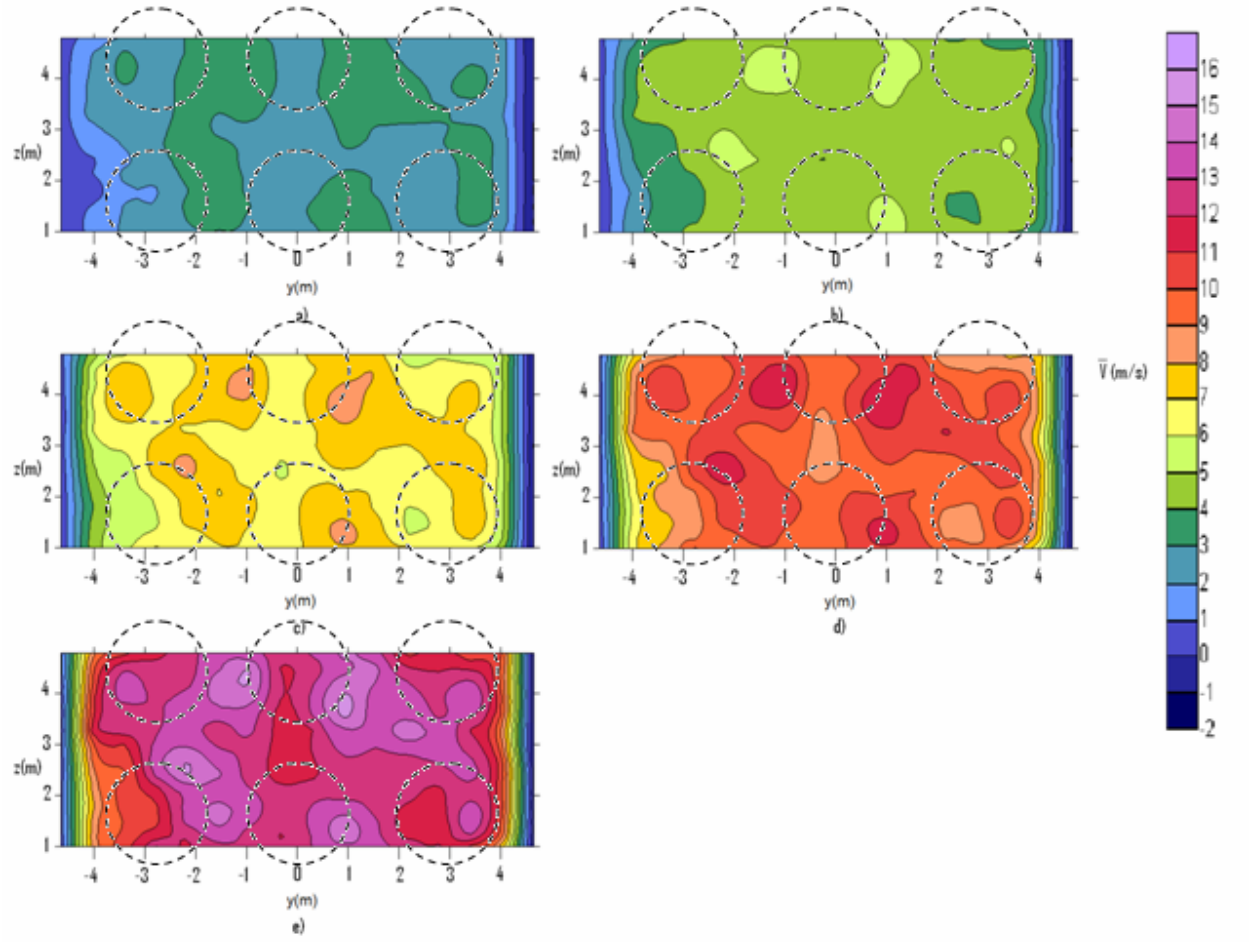

Figure 4.2 Velocity Contour Maps without a Blocking Object or False Floor present at x=2m with fan outlets superimposed for average wind speeds of a) 3 m/s b) 4.7 m/s c) 7.1 m/s d) 10 m/s and e) 13.5 m/s

As the flow travels down the experimental enclosure mixing occurs in the shear layers developed between the high velocity flow in regions between the fans and the surrounding air. As a result, the areas of elevated velocity should become more diffuse. Indeed, when comparing Figure 4.3 and Figure 4.1, the areas of elevated velocity seen at 5 m downwind are in the same relative locations as the areas of elevated velocity that appeared 2 m downwind, but the difference in velocity between the areas of elevated and depressed velocity is much lower at positions 5m downwind of the fan outlet. For example, two of the more pronounced areas of elevated velocity, centred at y = 1 m and z = 3.8 m and y = -1 m and z = 4 m respectively, in Figure 4.1 become much smaller in Figure 4.3, while the area around them becomes more uniform. Peak values of velocity also decrease as the flow becomes more uniformly mixed as well.

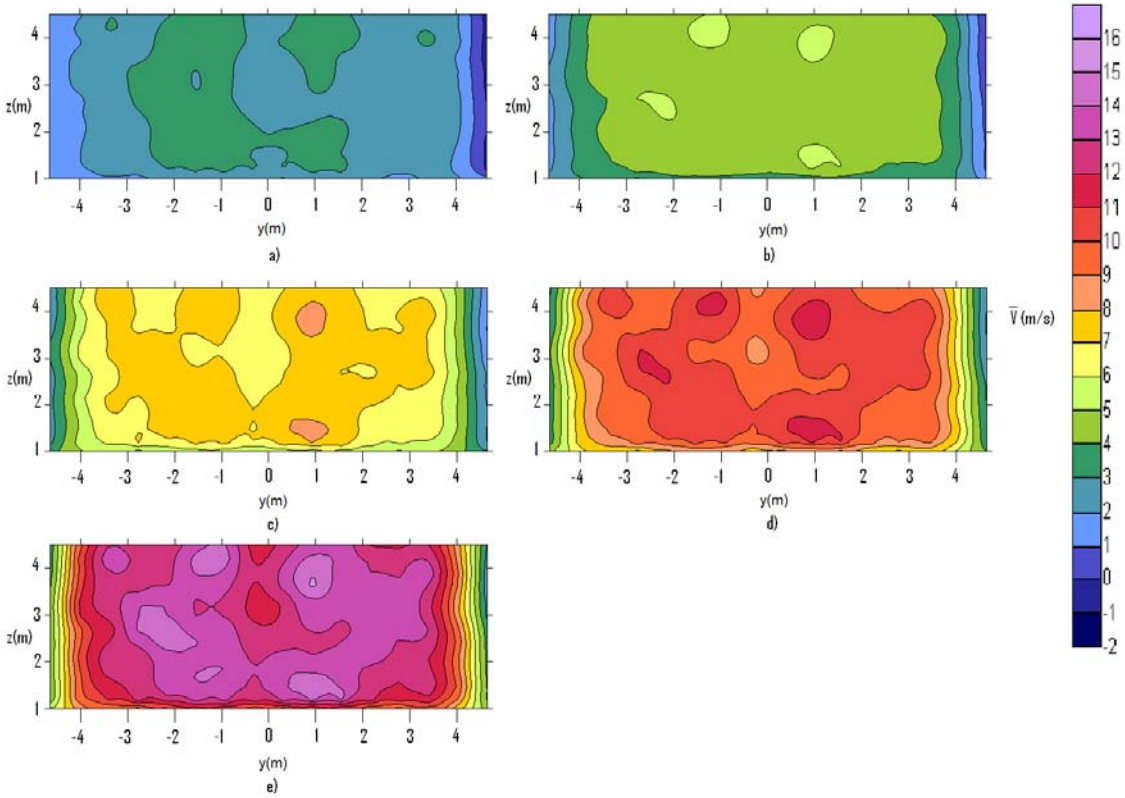

Figure 4.3 Velocity Contour Maps without a Blocking Object or False Floor present at x=5m with an average wind speed of a) 3 m/s b) 4.6 m/s c) 7.1 m/s d) 10 m/s and e) 13.5 m/s

In Figure 4.4, the mean velocity contours measured across the plane at x = 11 m downstream of the plenum exit are presented. While there are still some individual areas of higher velocity evident, the flow in the inner core at this downstream location appears to be much more uniform than for x = 2 m or x = 5 m locations. The overall extent of the inner core is smaller however, ranging between y = -4 m and y = 3.5 m. The outer flow regions along the walls now extend further into the region previously occupied by the inner core and the velocity gradient between the outer and inner regions of the flow is significantly less at this position compared to measurements made upwind of this position, In particular, the outer flow region on the –y side appears to have become more pronounced in the measurement area compared to measurements upwind.

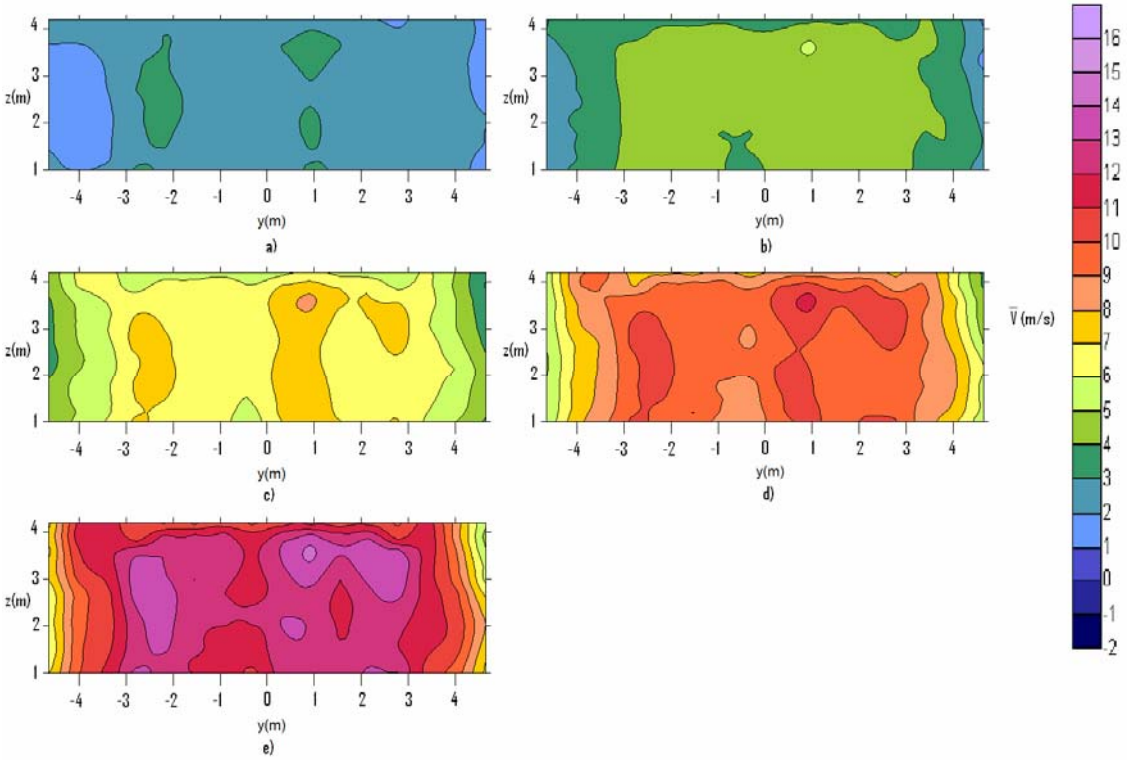

Figure 4.4 Velocity Contour Maps without a Blocking Object or False Floor present at x=11m with an average wind speed of a) 3 m/s b) 4.6 m/s c) 7.1 m/s d) 10 m/s and e) 13.5 m/s

The two large areas of high velocity seen in the contour plots of mean velocity in the inner core of the flow for x = 5 m are still quite distinct at x = 11 m, but they have narrowed in extent and the smaller localized areas of higher velocity appear to have mixed thoroughly with the surrounding slower air. The velocity deficit that was present near the centre of the flow field at x = 2 m and x = 5 m from the plenum outlet is still visible for wind speeds of 10 and 13.5 m/s, but is not nearly as well defined compared to the measurement planes upwind of this location. A new velocity deficit is now evident near the bottom of the measurement area and towards the centre-line of the facility for wind speeds of 4.6 m/s and above. It appears to be centered at y = -0.5 m and extends from the bottom of the measuring area up to z = 2 m.

As the flow travels this far downstream, there is more evidence of mixing between the areas of elevated velocity resulting from the merging flows issuing from the individual fans. Using the previous example of the two areas of elevated velocity that were measured upwind (centred at y = 1 m and z = 3.8 m and y = -1 m and z = 4 m), the area located at y = -1 m has completely mixed with the surrounding flow and does not appear as an area of elevated velocity at x = 11 m. The other area, centred at y = 1 m, has decreased considerably in size with much more uniform velocity in the surrounding flow.

When the results of Weisinger [11], seen in Figure 2.2, from the same location are examined, the two areas of elevated velocity have traversed the centre-line and merged to the point that they were indistinguishable at x = 15 m. This follows the bluff wall jet assumption that Weisinger made when characterizing this portion of the flow of the UWLFRF, as seen in the literature in review section 2.2. At this distance downwind, the jet has begun evolving from the "potential core region" to the "transitional" region and the areas of elevated velocity have mixed with the surrounding air so that the velocity is relatively uniform throughout the region. When

Figure 4.5 is examined, there is some evidence of mixing between the two regions of elevated velocity along the centre-line, but there is consistently an area of lower velocity between the two large areas of elevated velocity, which suggests that the bluff wall jet assumption may not be valid.

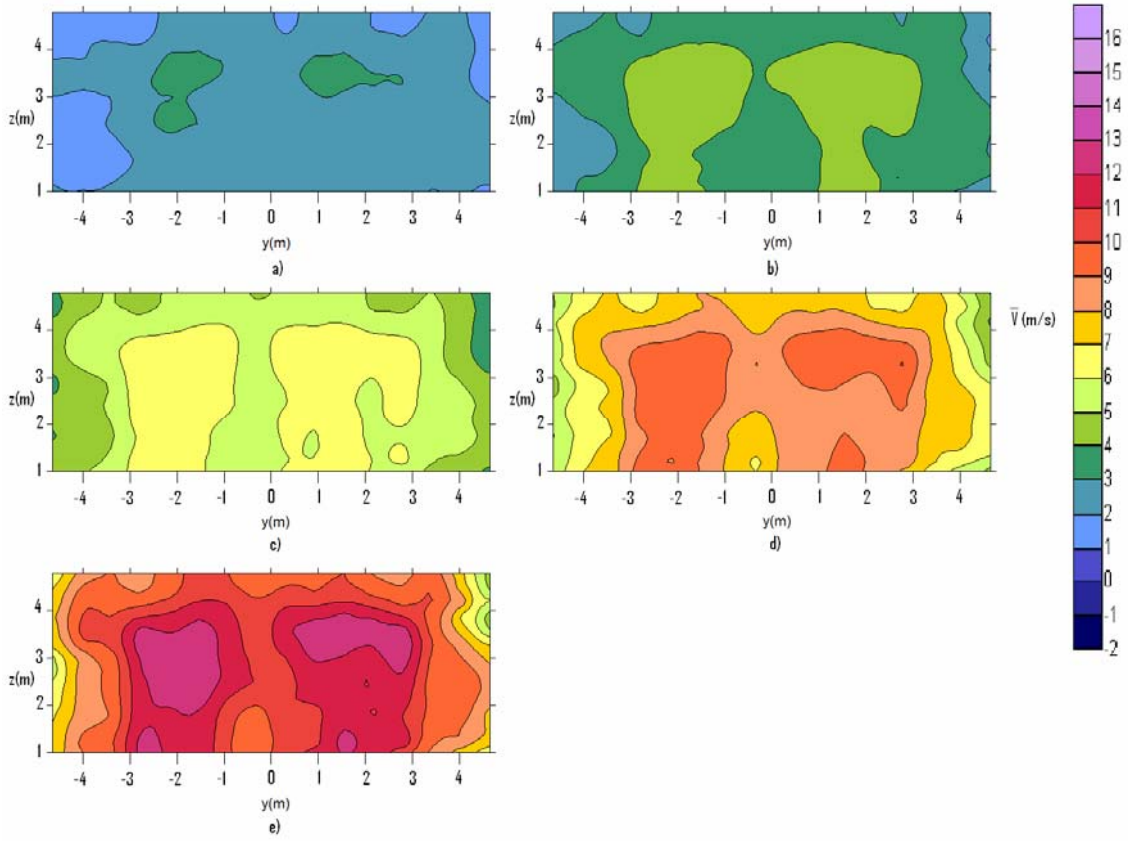

Figure 4.5 Velocity Contour Maps without a Blocking Object or False Floor present at x=15m with an average wind speed of a) 3 m/s b) 4.6 m/s c) 7.1 m/s d) 10 m/s and e) 13.5 m/s

Since the data suggests that the bluff wall jet assumption is not valid, another explanation for the development of the flow is needed. A likely explanation is that the bulk of the flow resembles a rectangular jet flow [14], which is discussed in more detail in section 2.1.2. The two large areas of elevated velocity are initially formed by the flows from the fans merging together due to the angled baffle plates. Once the fan flows have merged, however, they resemble a set of

two parallel rectangular jet flows traveling down the UWLFRF. Shear layers formed between these rectangular jets, areas of elevated velocity situated directly adjacent to the surrounding more quiescent air, promote mixing and expansion of the jets with distance downstream leading to more uniform velocity across the entire flow plane by the x = 15 m downstream location.. At this location, the rectangular jet is still in the "potential core" region, as shown in section 2.1.2. However, one of the more obvious features of the rectangular jet in the "transitional" region is visible, the "saddle shape" profile seen in Figure 4.5, where the maximum velocity is not seen at the centre of the jet, but is displaced laterally to each side. Since the jet has not had enough time to develop the "saddle shape" velocity profile, these areas of elevated velocity are created by the interaction between adjacent jets, as was the cause of areas of elevated velocity found upstream. These results differ from Weisinger, presented in Section 2.2, mostly due to changes in configuration within the test enclosure itself, as well as the installation of extension ducts on the middle fans to prevent air starvation while all fans are operating.

As mentioned in the experimental methods section, several live fire tests were performed with a false floor extension built upwind of the fuel pan as described in Section 3.3.3. With the floor installed, the forward facing step increase in floor level seen at the front of the fuel pan was no longer a factor as the upwind false floor extension was built level with the surface of the fuel pan. Therefore, with the false floor extension in place, any recirculation zone caused by the step would not affect the flow in the vicinity of the fuel pan. Figure 4.6 illustrates the mean velocity contours measured across the plane at x = 5 m downstream of the plenum exit across all wind speeds when the false floor was put into place upstream of the fire pan. The measurement plane x = 5 m was the only plane for which the presence of the false floor noticeably affected the local velocity results.

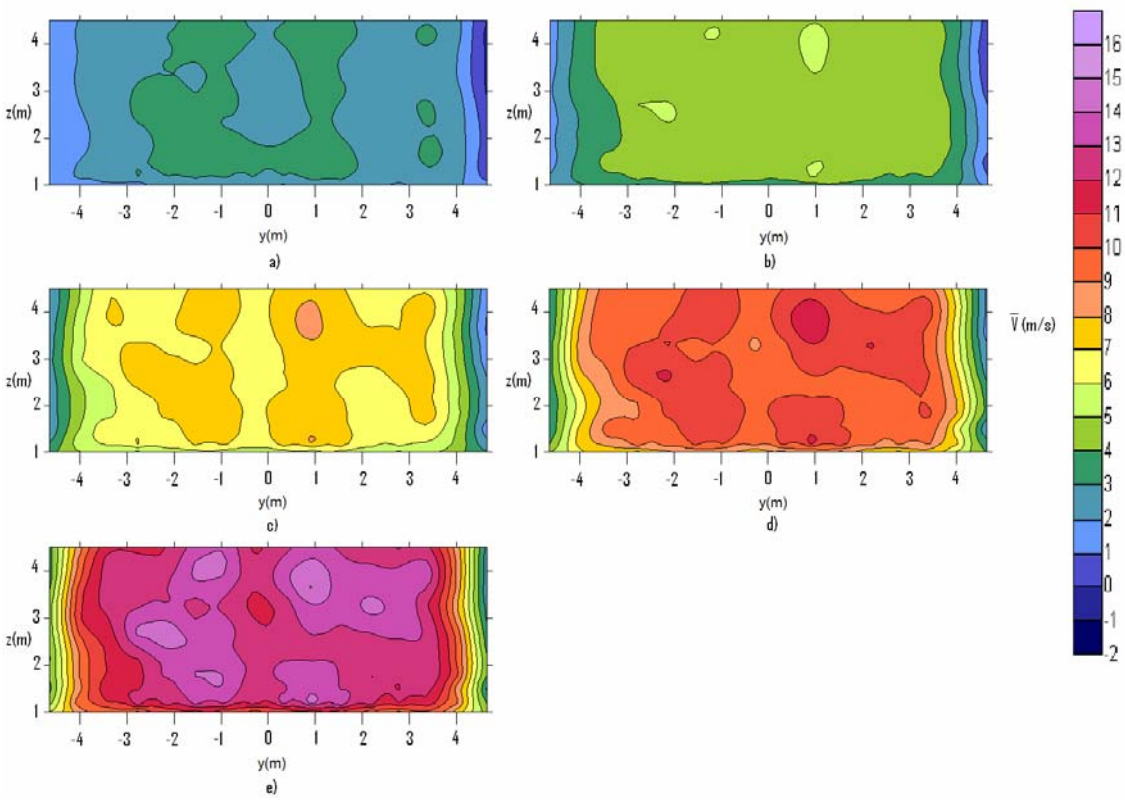

Figure 4.6 Velocity Contour Maps with a False Floor but without a Blocking Object present at x=5m with an average wind speed of a) 3 m/s b) 4.6 m/s c) 7.1 m/s d) 10 m/s and e) 13.5 m/s

When Figure 4.6 is compared to Figure 4.3, which is at the same location but without the false floor present, some differences may be observed. Both figures have similar "outer regions" and "inner regions" in the flow and there appears to be a boundary layer towards the bottom of each of the contour maps caused by interaction of the main flow with the floor. The large areas of elevated and depressed velocity are very similar in Figure 4.3 and Figure 4.6. The main difference between the two is the gradients between the localized areas of higher velocity within the larger areas of elevated velocity, especially closer to the floor of the facility. In Figure 4.3, there are several areas of localized elevated velocity, centred at y = 1 m and z = 1.5 m and y = -1.5 m and z = 1.5 m respectively, which are attributed to the merging of adjacent fan flows as they travel downstream. In Figure 4.6, these localized areas of elevated velocity are not nearly

as large suggesting different flow development and mixing between the fan flow and the surrounding air when the false floor is present, resulting in a more uniform flow. Since the purpose of the false floor was to decrease the effects of floor configuration and flow recirculation near the fuel pan, measurement of a more uniform flow close to the fuel pan with the false floor present is an encouraging sign.

4.2.2 Turbulence Intensity without a Blocking Object present

In order to fully characterize the flow through the UWLFRF it was necessary to measure both the mean flow and the turbulence intensity at all wind speeds. Therefore, levels of turbulence intensity were measured using the CSAT3 sonic anemometer simultaneously with the wind characterization measurements with no Blocking Object present. Mean velocity results have been presented in Section 4.2.1 for the tests in which there was no Blocking Object present. This section will outline results of turbulence measurements taken without a Blocking Object in the Facility.

The CSAT3 sonic anemometer was mounted at the centre of the bidirectional probe rake to simultaneously collect single point velocity and turbulence data for each height and downstream plane at which cold flow measurements were taken without a Blocking Object present. CSAT results are not available for vertical heights above 5.05 m since it was not possible to damp out vibrations of the probe stand at this height, especially for higher wind velocities. The centerline turbulence data provides an indication of the overall levels of turbulence within the flow which may useful in defining inlet boundary conditions for computational modeling of the flow through the facility. The mean velocity data are compared

with values measured by the adjacent bidirectional probes on the rake, with the precaution that the CSAT3 measuring location was on the centerline of the test enclosure and therefore offset 0.3 m vertically and 0.75 m upwind from the nearest bidirectional probe.

Figures 4.7 through 4.11 show vertical profiles of centre-line turbulence intensity measured at wind speeds of 3 to 13.5 m/s and at downwind locations, x = 1.25 m, 4.25 m, 10.25 m, and 14.25 m. In the final figure, Figure 4.11, the turbulence intensity levels measured at x = 4.25 m are presented to indicate the effect of the false floor on centre-line turbulence measurements in the facility.

In Figure 4.7, vertical profiles of turbulence intensity of velocity measured 1.25 m downwind of the test enclosure inlet are presented for flow velocities ranging from 3 to 13.5 m/s. The average turbulence intensity at each fan speed is over 10 %, with a minimum average turbulence intensity of 10.6 % reported at 4.6 m/s wind speed and a maximum average intensity of 11.5 % at 13.5 m/s wind speed. There is not a large variation in the measured turbulence intensity for different wind velocities this close to the inlet. In fact, the trends in turbulence intensity with height above the floor are similar in all of the graphs – the turbulence intensity initially decreases with height to a minimum turbulence intensity at approximately 2.35 m, followed by increasing turbulence intensity with height until the maximum level is reached at a height of 3.55 m (3.25 m for the lowest velocity of 3.0 m/s). Levels of turbulence intensity then decrease again towards the top of the measurement area. These consistent trends in the distribution of turbulence intensity along the facility centre-line for all velocity settings suggest that the key flow phenomena are also very similar for all levels of flow velocity.

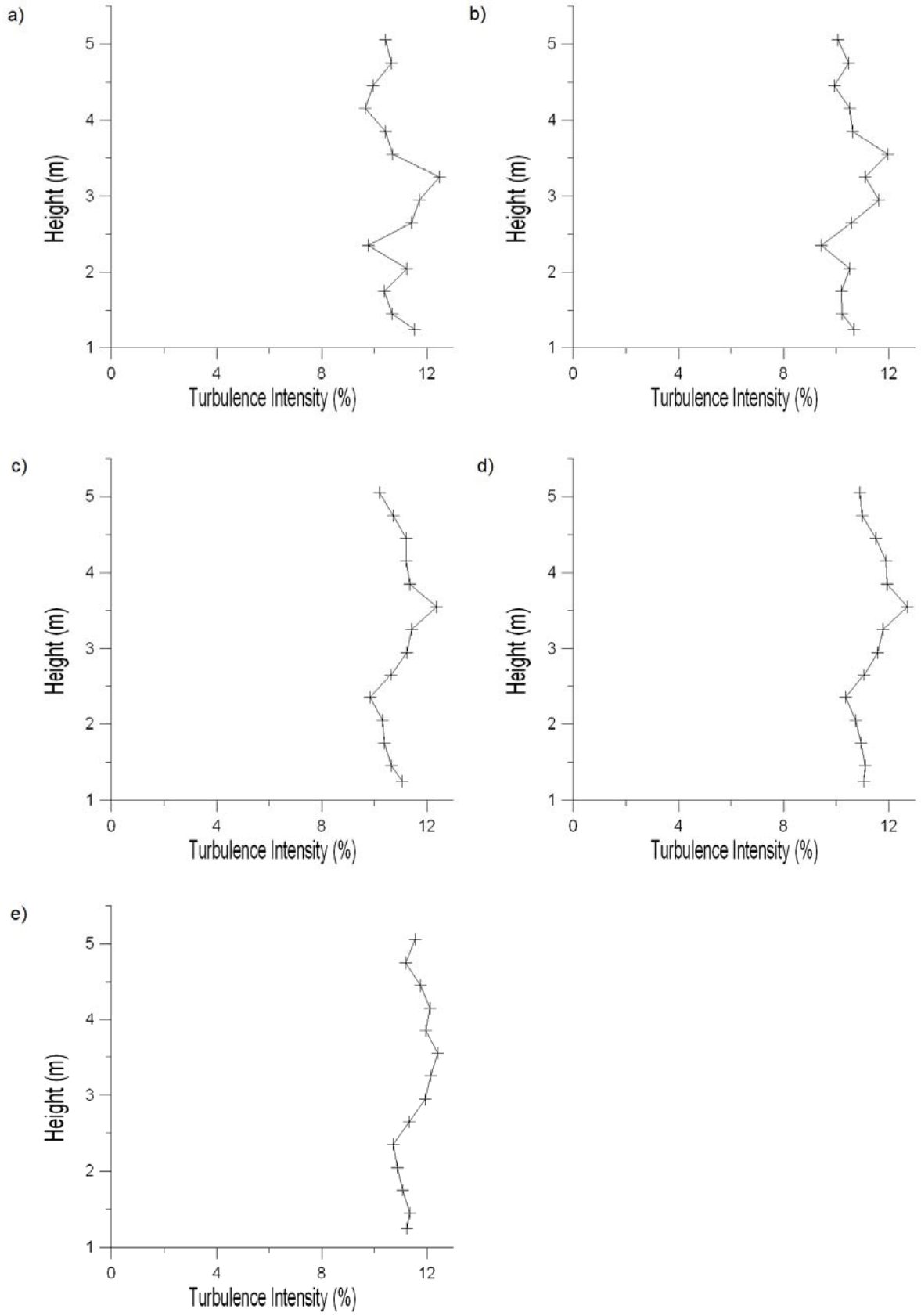

Figure 4.7 Cold Flow Centerline Turbulence Intensity of the Facility with No Blocking Object present at x=1.25m and a wind speed of a) 3.0 m/s b) 4.7 m/s c) 7.1 m/s d) 10.0 m/s and e) 13.5 m/s

In Figure 4.8, the centre-line turbulence intensity of velocity is plotted for positions 4.25 m downwind of the test enclosure inlet. The average turbulence intensity is lower compared to that measured 1.25 m downwind (Figure 4.7), with no values greater than 10 %. The lowest values of average turbulence intensity, approximately 8.5 – 8.6 % occur at the lowest velocities (3.0 and 4.6 m/s). The highest value, 9.6 %, occurs for the velocity of 7.1 m/s. At this position, the turbulence intensity remains fairly constant at levels between 8 and 10 % with height except for an apparent spike in value to as high as 18.6 % (7.1 m/s) at a height of 4.45m. A similar spike at z = 4.45 m also occurs for the 13.5 m/s velocity, although it is not as pronounced at 11.6 %. The greatly elevated level of turbulence intensity at this height may indicate the production of turbulence in the shear layer formed between the inner core of the main wind flow and any quiescent or slower moving air between the upper edge of the plenum outlet and peaked roof of the facility. When the contour maps are examined for this location [Figure 4.3], it can be seen that these measurements at z = 4.45 m occur in an area of depressed velocity directly between two large areas of elevated velocity forming on either side of the centre-line of the facility, which supports the hypothesis that the measurement occurs in a shear, and potentially unsteady fluctuating flow, layer between the faster moving core flow and an area of slower moving flow.

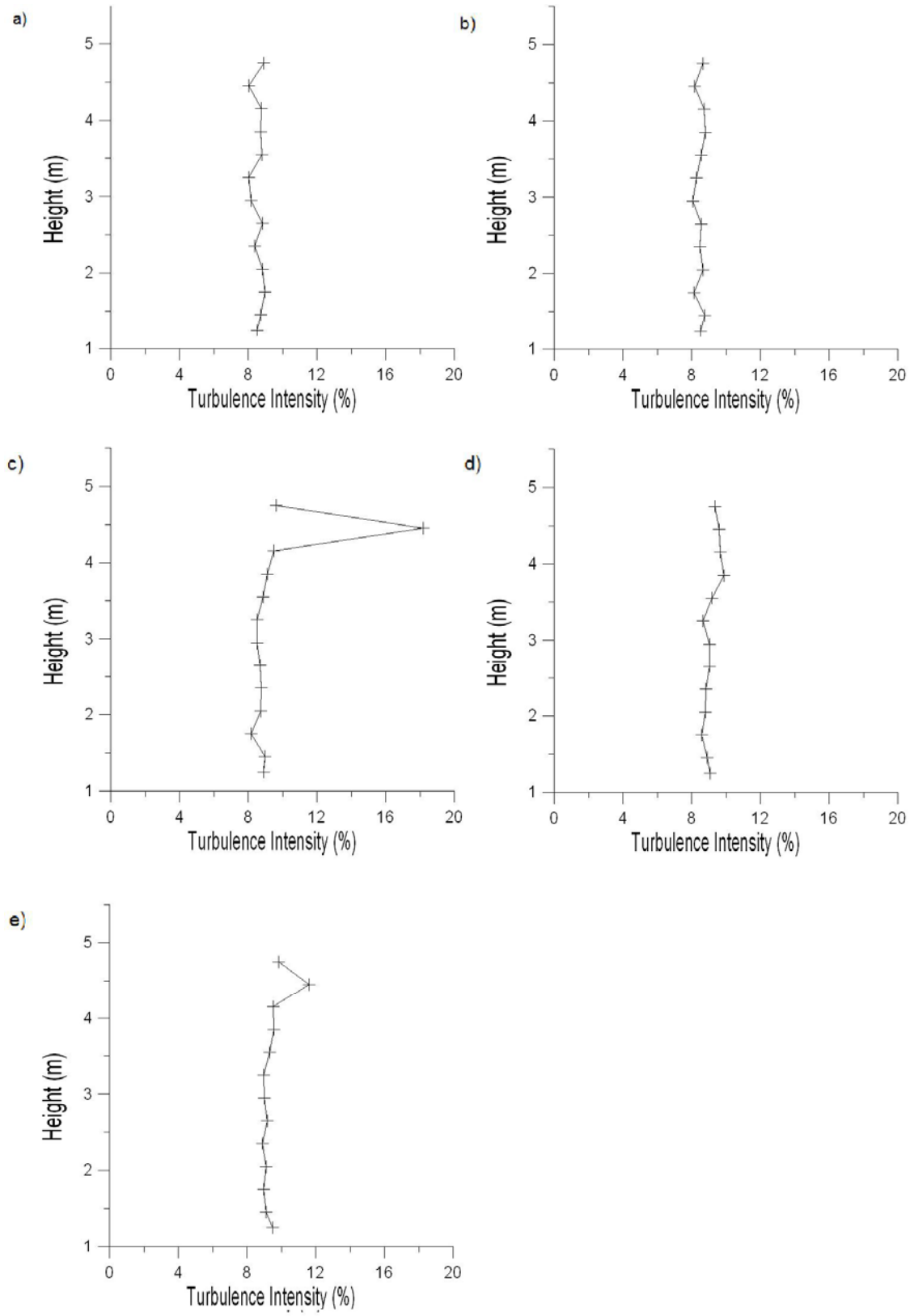

Figure 4.8 Cold Flow Centerline Turbulence Intensity of the Facility with No Blocking Object present at x=4.25m and a wind speed of a) 3.0 m/s b) 4.7 m/s c) 7.1 m/s d) 10.0 m/s and e) 13.5 m/s

Vertical profiles of mean turbulence intensity of velocity are shown in Figure 4.9 for all wind speeds and at a distance of 10.25 m from the test enclosure inlet. Levels of turbulence intensity averaged across the vertical measurement height range from 13 – 14.6 % at wind velocities of 4.6 m/s and 7.1 m/s respectively. The overall trends in each of the plots are similar. Every wind speed except 7.1 m/s fluctuates between 9 – 15 % until a height of 4.15 m is reached, at which point the turbulence intensity begins markedly increasing to the maximum value measured at a height of 4.45 m. This area of increased turbulence intensity is once again thought to be caused by an unsteady flow. The wind speed of 7.1 m/s follows this trend, except the fluctuations measure between 9 – 20 % before z = 4.15 m. The lowest values of turbulence intensity occur at heights that increase with mean flow velocity: from 2.65 m for 3 m/s, 3.25 m for 4.6 m/s, 3.55 m for 7.1 m/s and finally leveling off at a height of 3.85 m (only 0.6 m below the maximum intensity) for flow velocities of 10.5 and 13.5 m/s. The highest value recorded was 50.7 %, for a wind speed of 13.5 m/s. This turbulence intensity is incredibly high given the experimental setup, which leads us to conclude that this must be an area of unsteady flow elevating the measured turbulence intensity unrealistically.

When the contour maps presented earlier are examined [Figure 4.4], measurements taken at z = 4.15 m in the area of unsteady flow occur at the top of the contour map measurement area, in between the two large areas of elevated velocity on either side of the centre-line of the test enclosure. Cold flow contour measurements at a height of 4.45 m are unavailable but according to the CSAT3 data are in this same area of unsteady flow.

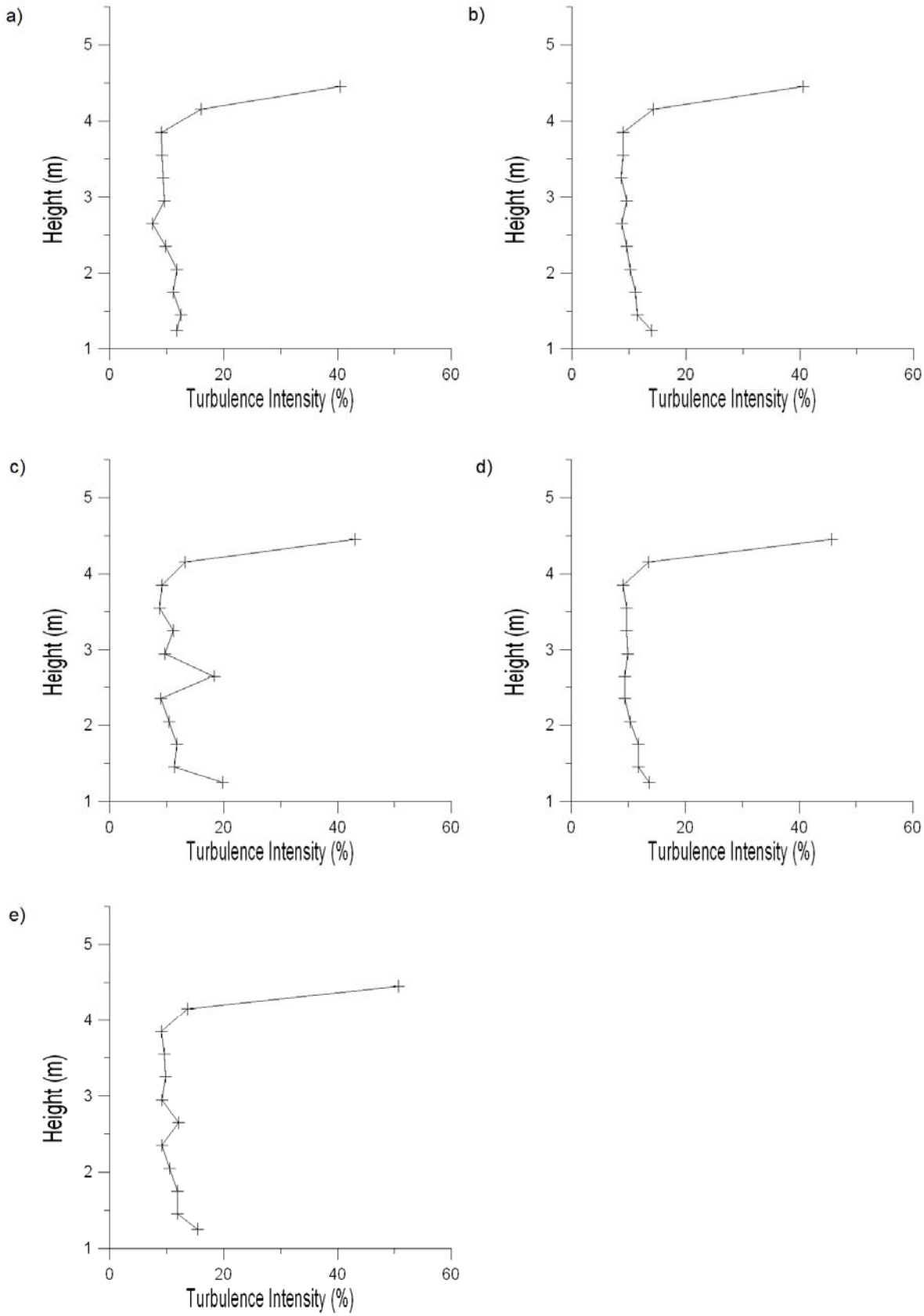

Figure 4.9 Cold Flow Centerline Turbulence Intensity of the Facility with No Blocking Object present at x=10.25m and a wind speed of a) 3.0 m/s b) 4.7 m/s c) 7.1 m/s d) 10.0 m/s and e) 13.5 m/s

Vertical profiles of centre-line turbulence intensity of velocity measured at the farthest downwind measuring point x = 14.25 m, are shown in Figure 4.10. The highest average value of turbulence intensity, 12.4 % occurs at the lowest wind speed of 3 m/s while the lowest average value, 11.2 %, occurs at speeds of 7.3 and 10.5 m/s. Again, similar trends in the change in turbulence intensity with height can be seen for all wind speeds. Until a height of 3.55 m above the floor, values of turbulence intensity oscillate around a mean level of about 8 % with the lowest values occurring at different heights for each wind speed tested. Above a height of 3.55 m, the CSAT3 enters the area of unsteady flow and values of turbulence intensity steadily increase with height until maximum levels are reached for a height of 5.05 m above the floor. At this position, the values range from 22.4 % to 28.5 % with highest value recorded for the lowest wind speed of 3 m/s.

When the contour map of this location [Figure 4.5] is examined, the measurement locations which show the elevated levels of turbulence intensity at a height of 3.55 m and above are all located in a shear layer suspected of unsteady flow, just like the measurement locations upwind. The two large areas of elevated velocity on each side of the test enclosure centre-line are still present at this distance downwind, and the measurements once again take place in an area of depressed velocity directly in between the two large areas of elevated velocity.

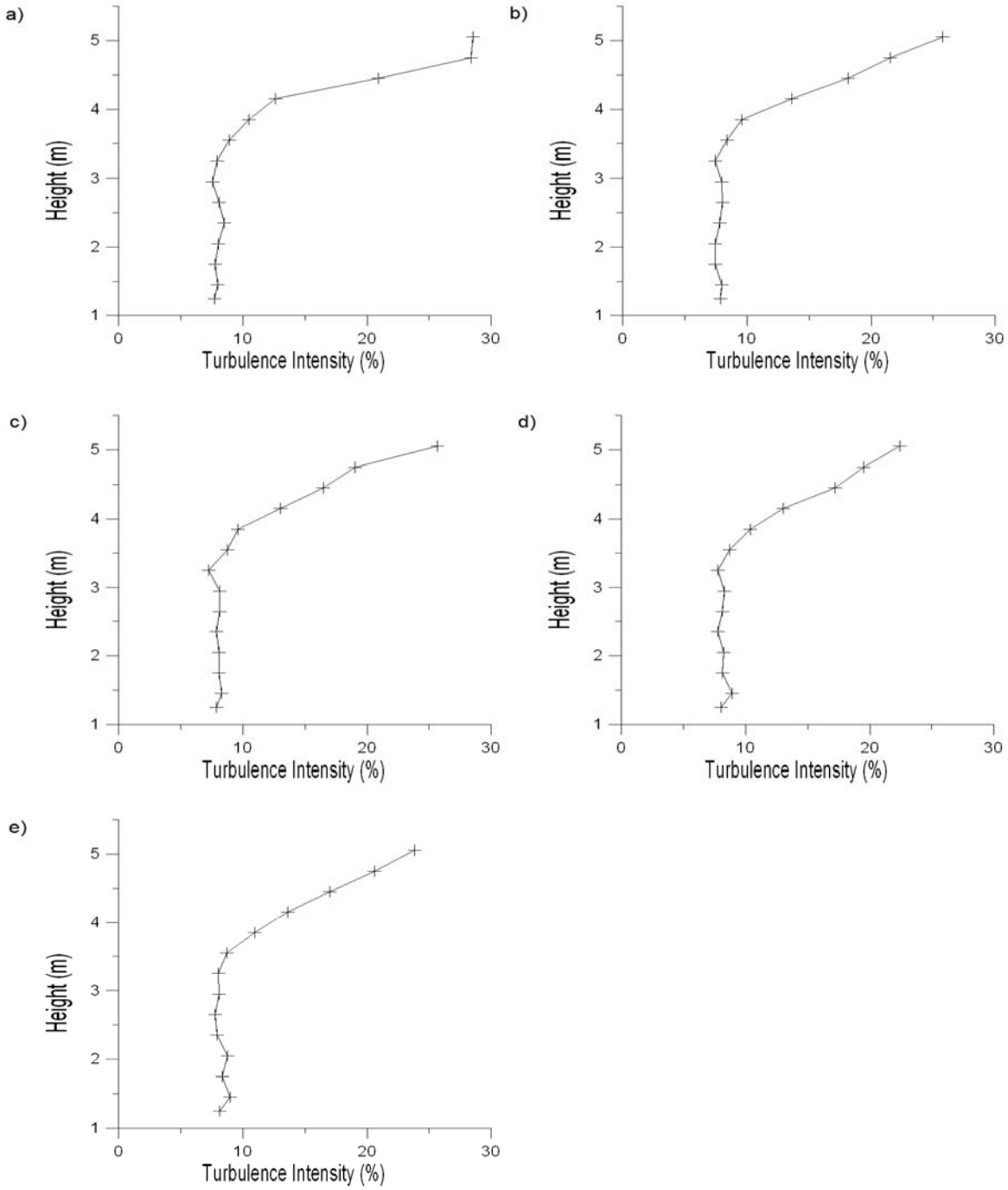

Figure 4.10 Cold Flow Centerline Turbulence Intensity of the Facility with No Blocking Object present at x=14.25m and a wind speed of a) 3.0 m/s b) 4.7 m/s c) 7.1 m/s d) 10.0 m/s and e) 13.5 m/s

Overall, most of the turbulence intensity measurements made on the centre-line of the UWLFRF are on the order of 10 %, which is a reasonable amount of turbulence intensity for such a facility. Areas of extremely elevated turbulence intensity are likely caused due to unsteady flow phenomena, and the results from x = 2 m are promising for providing boundary conditions for computer simulations in the future.

Several of the live fire tests during the test series with no Blocking Object present in the facility were conducted with a false floor built up around the fuel pan. The presence of this false floor moved the step change in floor height further upwind of the fuel pan position, so the effect of this forward step [26] on the flow in the fuel pan area should be decreased. In an attempt to gain some insight into the effect of this false floor on the local turbulence intensity levels near the fuel pan, vertical profiles of turbulence intensity of velocity were measured using the CSAT3 for the configuration with a false floor installed. Measurements were conducted at x = 1.25 m, x = 4.25 m and x = 10.25 m as for the previous turbulence intensity measurements; values were not measured at x = 14.25 m as this location was expected to be far enough downwind so as to not see any persistent effects on the flow due to the presence of the false floor. Initial examination of the results indicated that only the results from the tests at x = 4.25 m showed any significant difference from those taken without the false floor. These are presented in Figure 4.11.

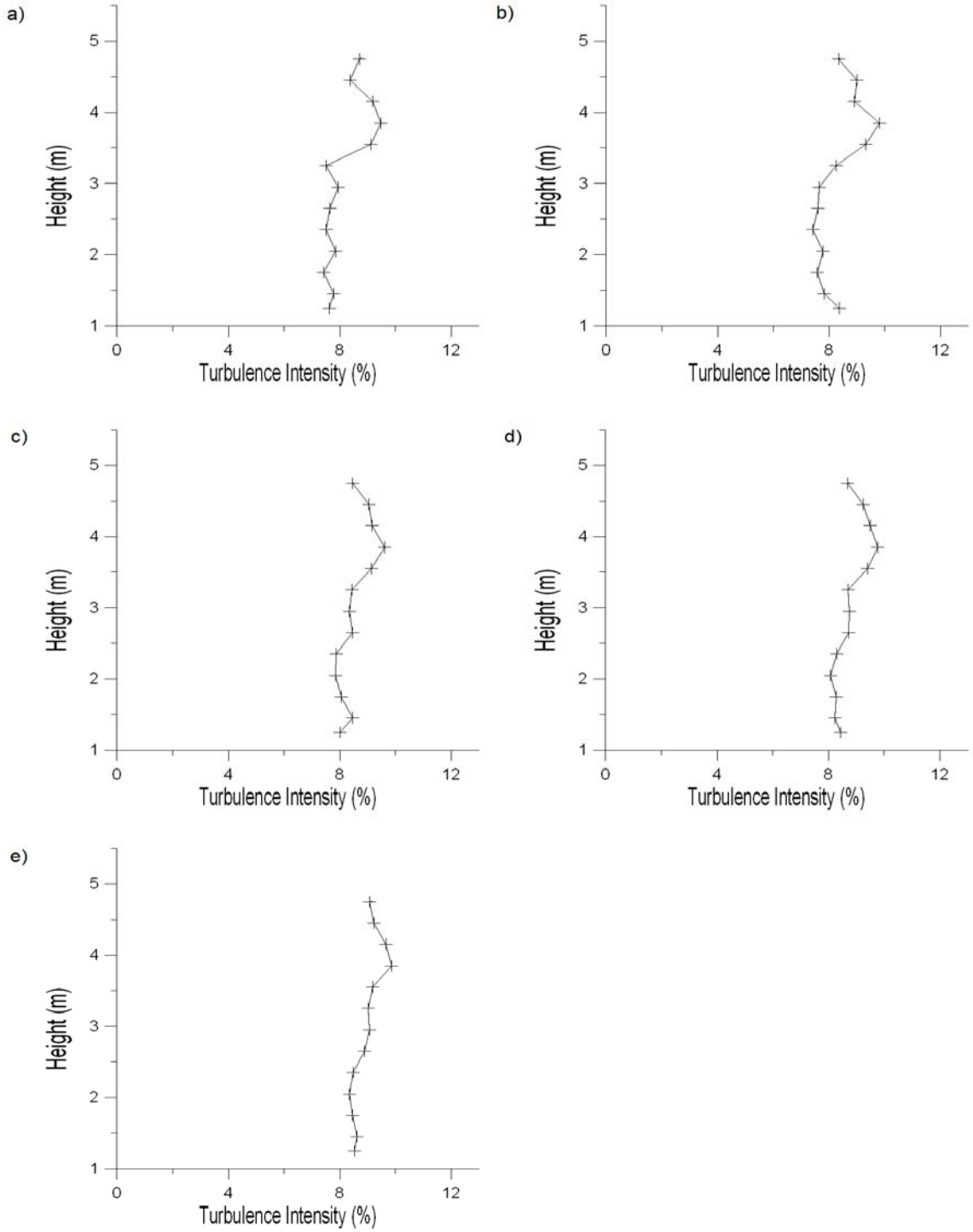

Figure 4.11 Cold Flow Centerline Turbulence Intensity at x=4.25m with a false floor in place and a fan speed of a) 15 Hz b) 22 Hz c) 34 Hz d) 47 Hz and e) 60 Hz

With the false floor in place, the shape of the vertical profiles of centre-line turbulence intensity [Figure 4.11] change considerably over those previously presented for the case without the false floor present [Figure 4.8]. The average levels of turbulence intensity are slightly lower, ranging from a minimum value of 8.2 % at a velocity of 3 m/s to a maximum of 9.0 % at a velocity of 13.5 m/s. They also increase with increasing wind speed, a phenomenon not noted for any of the previously reported measurement positions. In the previously reported measurements without the false floor present [Figure 4.8], the levels of turbulence intensity remain fairly constant with height until 4 m above the floor; however, in the present results [Figure 4.11] maximum levels of turbulence intensity occur at a height of 3.85 m for every fan speed and the turbulence intensity then decreased with increasing height. This may suggest that some of the unsteady flow phenomena are not present when the false floor is in place, as the overall turbulence intensity decreased and the turbulence intensity peaks are greatly decreased. The maximum level of intensity was 9.9 % measured for a wind speed of 13.5 m/s. In contrast, for measurements taken without the false floor in place, the maximum value was almost twice this level and was measured at a height over 4 m above the floor. Therefore, while the false floor does appear to have some effect on the overall levels of turbulence intensity within the test area; they are quite localized and not of sufficient magnitude to greatly influence the overall flow development downwind of the fuel pan area.

When the contour map of this location is examined [Figure 4.6], the locations of elevated turbulence intensity are in between the two large areas of elevated velocity, just like the other CSAT3 measurements which showed elevated levels of turbulence intensity. As seen previously, this area between the regions of elevated velocity and depressed velocity is more turbulent due to the shear layers formed during the mixing of the flow.

4.2.3 Wind characterization with a Blocking Object present

The last section presented results of the facility flow characterization for the reference fire cases when no Blocking Object was used. In preface to live fire experiments with a Blocking Object, this section presents results of the wind characterization in the test enclosure when there was a Blocking Object present. Due to the presence of the Blocking Object and its support structure, the velocity across the y-axis could only be measured at certain locations. For this, two locations in front of the Blocking Object, at x = 2 m and x = 5 m and two locations behind the Blocking Object, at x = 15 m and at x = 17.39 m were chosen. The measurement planes in front of the Blocking Object and at x = 15 m downwind of the plenum match those used for the measurements without the Blocking Object (Section 4.2). The location x = 15 m also corresponds to the position at which wind speed measurements are taken during a fire test. The final measurement plane, x = 17.39 m, is designated as the outlet velocity measurement position in order to characterize the flow as it is leaving the test enclosure. The flow was characterized for four distinct wind (fan) speeds: 4.6 m/s (22 Hz), 7.3 m/s (34 Hz), 10.5 m/s (47 Hz) and 13.5 m/s (60 Hz), covering the range of interest for the live fire tests with Blocking Object as well. Using the data from each of the locations, velocity contour maps were made for each location at each fan speed. These contour maps use the Kriging interpolation method [92] to create the isovels in the computer program Surfer 9 [92].

Figure 4.12 contains contour maps of mean velocity data measured across the region -5 m < y < 5m and at heights z = 0 m to 6 m at a position x = 2 m downwind of the plenum outlet for each wind speed. Overall these profiles are very similar to those already presented in Figure 4.1 for the case when there was no Blocking Object present (note that the contour plots in the previous section extended across heights only from z = 1 m to a maximum of z = 4.8 m). The

inner core (fairly uniform velocity) and outer flow (high velocity gradient) regions are again very distinct at this position. For the lowest wind speed, the flow throughout the inner core is fairly uniform with several small localized regions of higher or lower velocity. As the wind velocity increases, larger areas of higher and lower velocity can be seen.

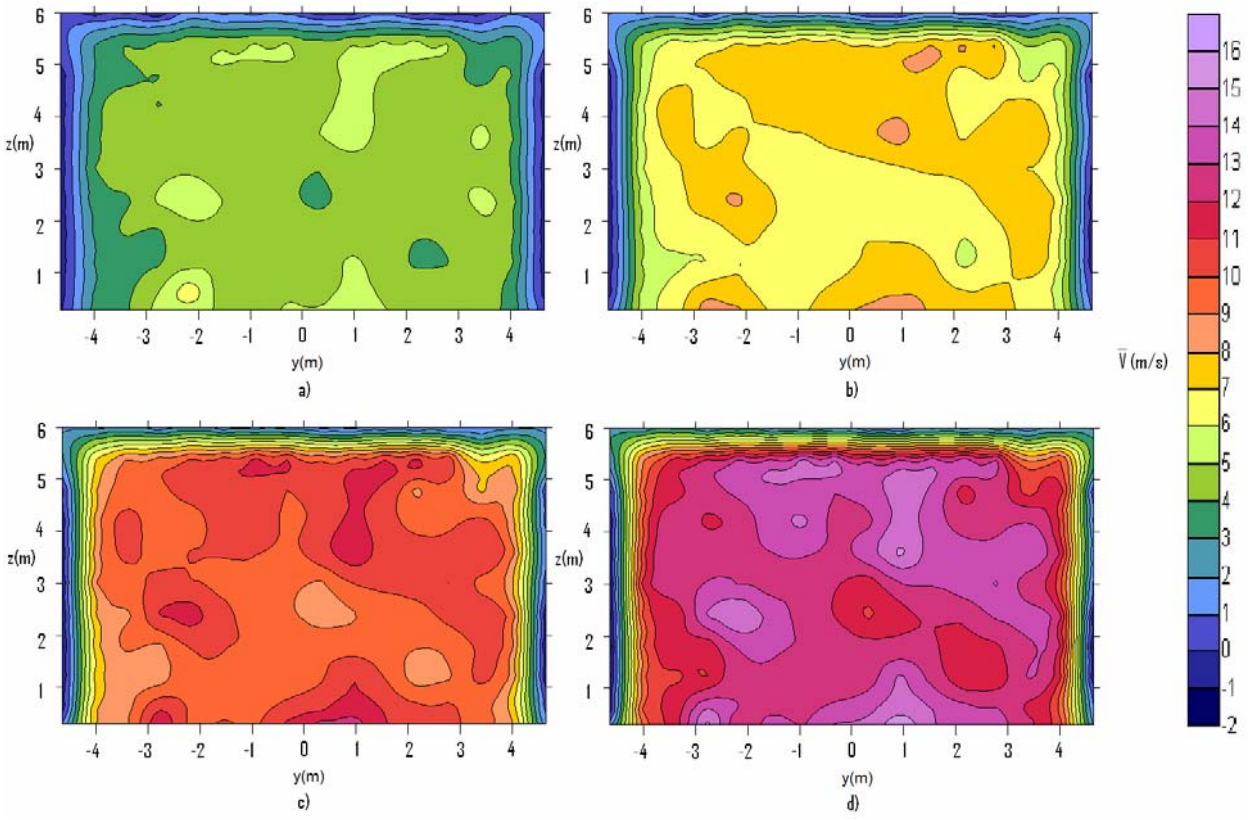

Figure 4.12 Velocity Contour Maps with a Blocking Object present at x=2m with a wind speed of a) 4.7 m/s b) 7.3 m/s c) 10.5 m/s and d) 13.5 m/s

Two areas of elevated velocity are evident near the floor of the enclosure, for all wind velocities tested, at x = 2 m downwind of the plenum outlet. The larger of the two areas is centered close to y =1 m and the smaller is centered at y = -2.2 m.

Areas of velocity deficit are also evident on the top right hand side of the plot, at y=3.5m and above z = 4.2 m, in the middle of measurement plane, z = 2.86 m and y = 0 m and in the

lower corners of the plots, z = 2.4 m and outside of -2 m > y and y > 2 m. For the latter, the deficit on the –y side is more marked than that on the +y side. All the areas of velocity deficit observed in Figure 4.12 correspond closely by location to areas of velocity deficit already noted for x = 2 m downwind of the plenum outlet for the situation where no Blocking Object was present (Figure 4.1). In Section 4.2.1 they have been attributed to interaction between the flow and the facility, as well as blockage in the flow due to the presence of a heater, which is in the top right hand side of the plot.

Since this measuring location is again very close to the outlets of the six individual fans, many of the flow characteristics seen at this location result from a combination of features due to the individual flows from each of the fans as well as initial interactions between them.

For that reason, in Figure 4.13 the outlines of the individual fan outlets have been superimposed over the contour maps shown in Figure 4.12 for a position 2m downwind of the plenum outlet. The angles of the fan outlet baffle plates (discussed in Section 4.1) again force the bulk of the flow away from the centers of the fans towards the regions between the fan outlets, leaving areas of reduced velocity towards the fan centres. This trend appears at all wind speeds, and to some extent at every fan location, but is most visible at the two higher wind speeds.

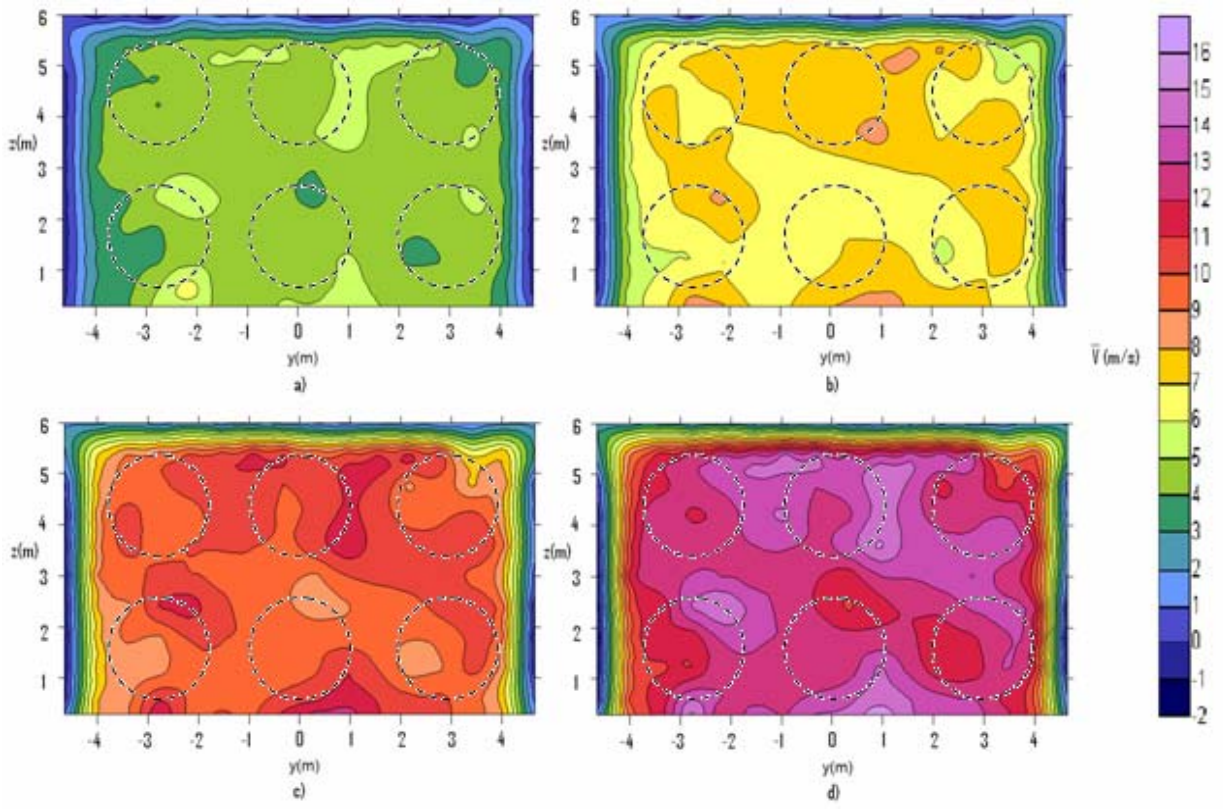

Figure 4.13 Velocity Contour Maps with a Blocking Object present at x=2m with superimposed fan outlets with a wind speed of a) 4.7 m/s b) 7.3 m/s c) 10.5 m/s and d) 13.5 m/s

The two areas of elevated velocity near the floor of the enclosure were previously seen in the work of Weisinger [11]. They were also seen when the Blocking Object was not present in the test enclosure, as seen in the previous section. This is consistent with expectation since the Blocking Object is not expected to affect the flow this far upwind. These regions are much better defined in this figure than in the previous section, due to the measurement area extending much closer to the ground. In the previous section, only the top of these areas of elevated velocity was visible in the contour map because the bidirectional probes were not lowered as close to the floor due to the presence of the CSAT3. In Figure 4.12, the two areas of elevated velocity mentioned in the previous paragraph are located beneath the outlets of the bottom middle fan and the bottom

fan on the –y side. All the other areas of elevated velocity appear between the fan outlets, and are thought to represent the merging of the flows from two adjacent fans.

The velocity depression on the top +y corner of the measurement area was previously thought to be caused by the interaction with the large box heater located in the test enclosure, and has been seen in previous measurements as well [11]. However, it did not appear in the previous section where the Blocking Object was not present, but the heater was. This suggests that while the heater may contribute to the flow pattern it is not likely the sole cause of this depression. Similar depressions exist in two other corners of the measurement area at all wind speeds, at y = -3.5 m and z = 4.8 m and y = -3 m and z = 1.3 m respectively. Finally, at the highest wind speed, another similar depression occurs in the fourth corner of the measurement area, at y = 3.5 m and z = 0.8 m. A likely explanation is that these areas of depressed velocity are due to the expansion of the flow coming from the plenum into the test enclosure, as these depressions occur on the corners of the rectangular flow issuing from the six fans as it mixes with the surrounding air. The depression in the middle of the measurement area was previously mentioned in section 4.2.1 [11]. It is located in the middle of the "inner region" between the top and bottom centre fans and also in approximately the same location on the y-z plane as the middle of the 'x' formed by the supporting beams inside the plenum area, as mentioned in section 3.1.2 as well as the previous section with no Blocking Object. Overall, the velocity results at x = 2 m resemble flow distributions measured during previous attempts to characterize the wind flow at the UWLFRF [11]. The good comparison between flow profiles at x = 2 m independent of the downstream configuration of the facility suggests that they do indeed constitute reasonable inlet flow boundary conditions to use for modeling various scenarios in the UWLFRF.

Figure 4.14 contains contour maps of mean velocity data measured across the region -5 m < y < 5 m and at heights z = 0 m to 6 m at a position x = 5 m downwind of the plenum outlet for each wind speed. Some of the notable features of the contour maps of the velocity at x = 5 m [Figure 4.14] trace their origins to phenomena seen in the x=2m velocity plots [Figure 4.13]. Most of the areas of elevated velocity located between the fan outlets are still visible in this figure. However, these contour maps have some significant differences compared to the contour maps at x = 2 m, which will be further outlined in the following paragraphs.

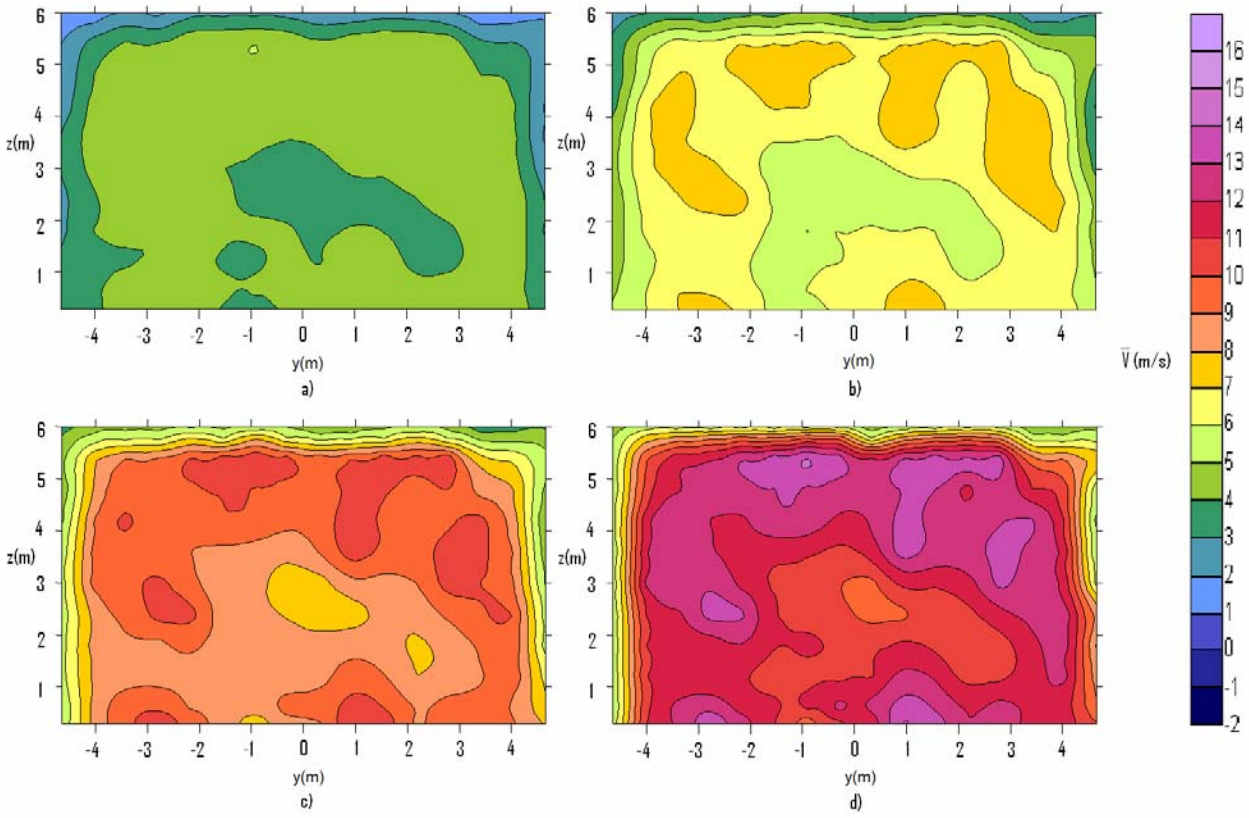

Figure 4.14 Velocity Contour Maps with a Blocking Object present at x=5m with a wind speed of a) 4.7 m/s b) 7.3 m/s c) 10.5 m/s and d) 13.5 m/s

The "inner region" and "outer region" are still visible at this measurement location, although the "outer region" has shrunk considerably compared to upwind. The "outer region" is

now mostly visible through higher velocity gradient regions which demarcate the mixing along the edges of the fast moving "inner region" of the flow and the nearly quiescent "outer region" along the walls and towards the roof of the facility. The upper gradients were not seen in previous contours (Section 4.2) since the measurements did not extend to this height above the floor.

The two regions of elevated velocity along the floor of the enclosure, seen in Figure 4.13 for x = 2 m and centered at y = 1 m and y = -3 m respectively persist in these contours as well. They are the only two regions of elevated velocity which are relatively unchanged in size and location from x = 2 m to x = 5 m.

There are several features evident in these contours which were not present for contours measured at x = 2 m with the Blocking Object or for any of the contours presented in Section 4.2 for flow characterization without the Blocking Object. Of particular note is the large velocity deficit that appears for all wind speeds in the middle of the measurement area, extending from -1.5 m > y > 3.2 m and from the ground up to z = 3.5 m. Much of this area is directly upwind of the location of the Blocking Object, which spans the entire horizontal measurement area and from z = 1 m to z = 3.7 m. There are three areas of elevated velocity which have been affected by the presence of the Blocking Object as well. The first region appears at -4 m < y < -1.8 m and 2 m < z < 5 m, and is the most well defined in the 7.3m/s graph. The second region of elevated velocity is at -2.5 m < y < 0 m and 4 m < z < 5.5 m, and has a consistent shape in the 7.3 m/s and higher wind speed graphs. The third region is a very large region of elevated velocity, which appears to break up into two separate regions at high speed. In the 7.3 m/s graph it spans from 0.5 m < y < 4.1 m and 1.8 m < z < 5.5 m. These three regions can trace their origins to areas of

elevated velocity located between fan outlets seen at x = 2 m, but shift away from the large central velocity depression in the "inner region" towards the edges of the Blocking Object in order to travel around it.

Figure 4.15 contains contour maps of mean velocity data measured across the region -5 m < y < 5 m and at heights z = 0 m to 6 m at a position x = 15 m downwind of the plenum outlet for each wind speed. The flow field characteristics shown in the contour maps are completely dominated by the presence of the Blocking Object. Almost none of the regions of elevated or decreased velocity, seen upwind at x = 2 m and x = 5 m, are present in these contour maps. A clear demarcation between the "inner region" and the "outer region" exists in areas of high velocity gradient around the outer perimeters of the contour plots, which mark the transition from the inner flow region to the more quiescent air layers on the perimeter and roof of the facility. These gradients are located near the edges of the measurement area, as the "inner region" encompasses almost the entire contour map at each wind velocity. One of the most notable features of the figure are the marked areas of low to negative velocity that occur under the Blocking Object between the two support stands at -1 m < y < 1 m from the ground to z = 1 m. Other recirculation zones and areas of very low velocity occur directly behind the Blocking Object, centered at y = 0.5 m and z = 3 m, as well as on the –y side of the object, at approximately y = -4 m and z = 1.5 m. A matching area of low velocity exists on the other side of the measurement area, centered at the edge of the +y side at y = 4.65 m and a height of 1.5 m.

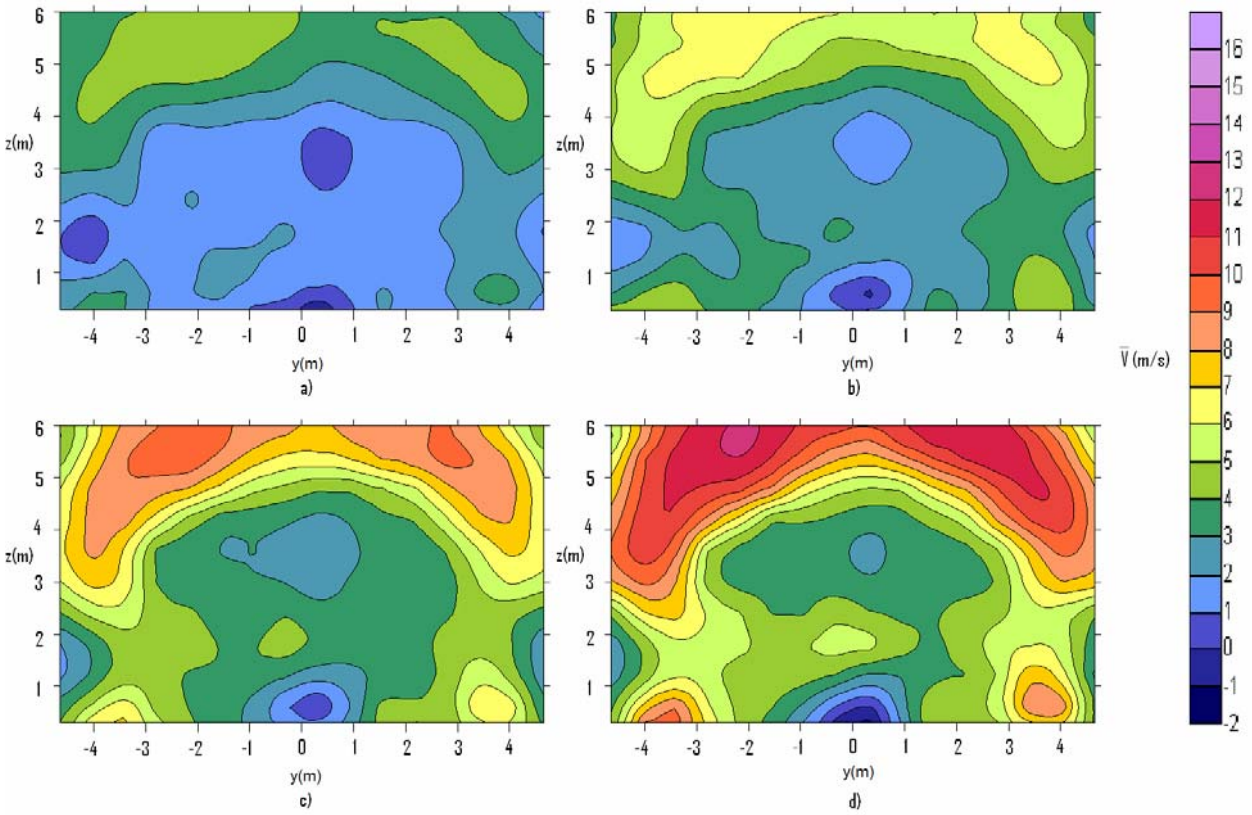

Figure 4.15 Velocity Contour Maps with a Blocking Object present at x=15m with a wind speed of a) 4.7 m/s b) 7.3 m/s c) 10.5 m/s and d) 13.5 m/s

Two regions of elevated velocity exist towards the top of the contour map, becoming better defined as the wind speed increases. At a wind speed of 13.5 m/s, they are centered above z = 5 m and at y = -2 m and y = 2.5 m. Two areas of elevated velocity also form near the bottom of the measurement area, at y = 3.5 m, z = 0.75 m and y = -3.5 m, z = 0.5 m respectively. All these regions have a much higher local velocity than their surrounding flow, and consequently there are large velocity gradients between these and the surrounding flow. The four regions of elevated velocity above and below the Blocking Object mark the region in which the flow is accelerating as it passes around the Blocking Object. It is important to note that many of the phenomena seen here are slightly offset to the +y side, such as the velocity deficits below and behind the Blocking Object, as well as the matching regions of elevated velocity traveling above

the Blocking Object. This may be caused by the geometric offset of the velocity inlet or to asymmetric expansion of the flow into the test enclosure as has been mentioned in previous sections.

The area of negative velocity occurring beneath the Blocking Object is a recirculation zone formed in the wake of the Blocking Object and/or behind one of the numerous pieces of instrumentation placed under the Blocking Object, such as a package calorimeter [8]. In previous studies by Weisinger[11] with the Blocking Object in place, this region of negative velocity was not observed; rather a region of elevated velocity was seen under the Blocking Object. The increased instrumentation under the Blocking Object in the present experiments has most likely led to this recirculation zone. The area of low velocity directly behind the Blocking Object is expected as it is directly in the middle of the wake from the Blocking Object, in a highly turbulent flow area.

Flow conditions at the outlet of the UWLFRF are presented in Figure 4.16, which contains a set of contour plots of mean velocity measured at 17.39 m downwind of the plenum outlet for all four fan speeds tested, spanning across the region -5 m < y < 5 m and at heights z = 0 m to 6 m.

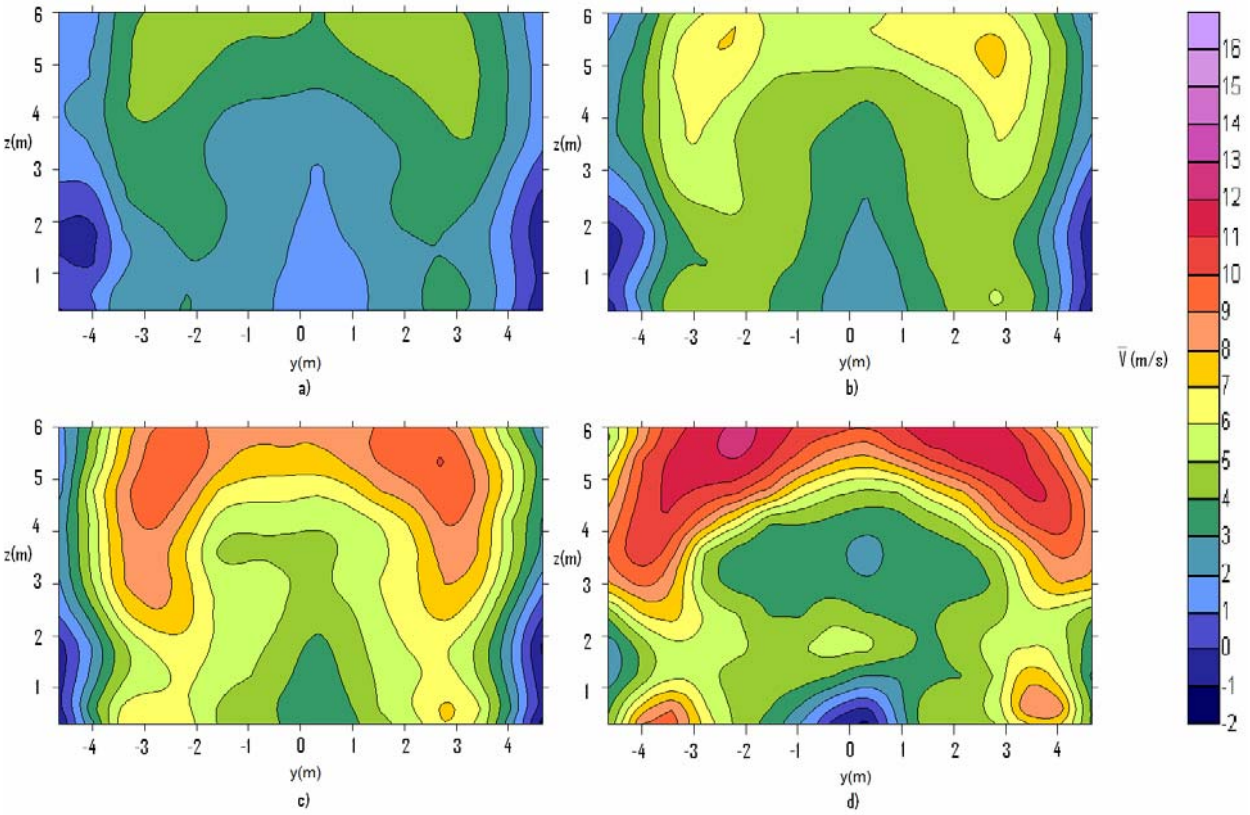

Figure 4.16 Velocity Contour Maps with a Blocking Object present at x=17.39m with a wind speed of a) 4.7 m/s b) 7.3 m/s c) 10.5 m/s and d) 13.5 m/s

Many of the features seen in Figure 4.16 can initially be seen upwind in the contour map at x = 15m [Figure 4.15]. There are four areas of elevated velocity, two above the Blocking Object centered at y = -2 m and y = 3 m at a height of 5.5 m, and two below the Blocking Object close to the test enclosure floor centered at y = ± 3.5 m and approximately 1 m off the ground. There are also two areas of decreased velocity at the lower corners of the measurement area, next to the regions of elevated velocity close to the floor. The area on the +y side has become much more well defined than at x = 15 m, and appears equally as strong as the depression on the –y side, which was more prevalent upwind. The recirculation area under the Blocking Object has become an area of low velocity, and merged with the recirculation area directly behind the Blocking Object to form an area of low velocity centered at y = 0.5 m spanning up to z = 3 m at

a wind speed of 4.7 m/s . At 13.5 m/s wind speed, there is evidence of a recirculation area just above the ground centered in the middle of the test enclosure along the y-axis that is not seen at any other wind speed.

The regions of elevated velocity seen above and below the Blocking Object in contours presented in Figure 4.15 for the position x = 15 m, are also evident in the Figure for x = 17.39 m. As mentioned previously, these regions are a result of the air being forced around the object. Other flow features, such as the velocity gradients observed at the top and along the edges of the measurement area appear to have broadened and smoothed out as would be expected with increasing distance and mixing downwind of the object.

Overall, these contour maps show that the Blocking Object dominates the flow field and causes large recirculation areas, regions of greatly accelerated flow velocity and other regions of lower flow velocity. In front of the Blocking Object, the flow is much more uniform but there are still some areas of elevated velocity. The flow at x = 2 m which is closest to the plenum, and least affected by the Blocking Object, is very similar to the results from the no Blocking Object contour maps. Therefore, these contour maps represent a reasonable estimate of the inlet flow for computer modeling of the facility at all wind speeds. As the flow approaches the upwind side of the Blocking Object, at x = 5 m, the effects of the object can be seen, as the flow adjusts and begins to accelerate above and below the object. Downstream of the Blocking Object, flow patterns are dominated by flow in the wake of the object with high gradient regions gradually expanding and smoothing out with increasing downstream distance. These persist all the way to the outlet of the facility. There are also local effects beneath the object that result from the large calorimeters and other instrumentation that was necessary for the fire experiments simultaneously being conducted by Lam [8].

4.3 Large Scale Fire Test Results

Now that the flow through the facility has been characterized, the 2 m diameter jet fuel spill fire tests were conducted under varying ambient and crosswind conditions, with and without a false floor installed and with and without a Blocking Object present in the UWLFRF. In the next sections, results of the fire tests conducted without the Blocking Object present will be discussed first, followed by those for fire tests with the Blocking Object present. Cross wind velocity is known to have a significant effect on fuel regression rate and fire plume development in 2 m diameter liquid fuel fires [37, 60 - 62]. In addition, ambient temperature has previously been seen to have a discernable effect on measured fuel regression rates in fire tests conducted in the UWLFRF [10]. The effects of additional factors, such as ambient wind conditions, turbulence intensity of the crosswind flow and the floor configuration around the fuel pan, have not been previously investigated. They are included here in attempts to quantify their effects, if any, on the present results, as well as to gain more insight into the various factors that may in future affect fire testing at the UW Facility. To this end, weather data from the Region of Waterloo was used to determine ambient wind and temperature conditions for each of the tests. In addition, for the tests in which there was no Blocking Object present, turbulence intensity measurements were made using the CSAT3 anemometer system described in the cold flow wind characterization measurements in Section 4.2.2 above.

4.3.1 Turbulence Measurements and Ambient Conditions During Fire Tests without a Blocking Object present

Nine 2m diameter JP-8 spill fire tests were conducted under crosswind speeds ranging from 3 – 10 m/s without the Blocking Object present in the facility. As can be seen from Table 4.1, two fire tests were conducted for each cross wind speed: one with a false floor present and one without, while three tests were conducted for a crosswind velocity of 7.1 m/s, one with a false floor and two without. Due to the extreme angle of tilt of the fire plume observed in tests conducted in crosswinds of 10 m/s, seen in subsequent sections in this chapter, no tests were conducted at the highest cross wind velocity of 13.5 m/s.

Before describing the results of the live fire tests, it is important to document the key conditions under which each test was conducted. Table 4.1 summarizes the ambient conditions, cross wind velocity, turbulence intensity and geometric floor configuration used for each of these fire tests. Effects of each factor on the final test results are presented in later sections. For ease of analysis, the rows in the Table are ordered from lowest to highest crosswind velocity, although in reality this was not the order in which the tests were conducted.

The first column in Table 4.1 contains the reference test number for a particular fire experiment while the final column indicates the floor configuration used for that test. In Column 2 , the crosswind velocity conditions for each test are documented, as determined by the average steady state velocity measured by the span of bidirectional probes mounted directly upwind of the fuel pan at x = 2 m. The turbulence intensity, Column 3, was measured using the CSAT3 anemometer system described in the cold flow characterization experiments above (Section 3.2.2). In order to directly measure the turbulence intensity of the crosswind during each fire test,

the CSAT3 anemometer was mounted upwind of the fire and offset to the –y side. This shielded it as much as possible from the extreme conditions of the fire [Section 3.2.3] Due to the offset of the CSAT3 probe from the facility centre-line, as well as spatial variation in flow conditions outlined in section 4.2 above, however, the results listed in Table 4.1 for turbulence intensity of the crosswind are considered indicative of ambient turbulence intensity levels during the tests, but cannot be directly compared to the centerline turbulence intensity measurements taken during cold flow testing.

As can be seen from the Table, the measured turbulence intensity in the cross wind flow ranged between 11 and 20 %, with an average level of turbulence intensity of 12.8 %. The turbulence intensity measured during test 43 at a crosswind velocity of 7.1 m/s was significantly higher than that measured in the two other tests (# 37, 41) at the same wind speed. Since the ambient wind direction for all three tests was directed from the fan inlets towards the test enclosure outlet (i.e. along the x-axis of the facility) and the ambient wind and temperature are not significantly higher than similar tests where the CSAT3 recorded lower values of turbulence intensity, the ambient conditions during test 43 are not a likely cause for the high values of turbulence intensity measured. In fact, for this test, the wind outside the test enclosure averaged 3.4 m/s, which was higher than Test 37 at 1.8 m/s but lower than Test 41, which measured 3.9 m/s. The ambient temperature during Test 43 was 4.3 ° C, which was higher than Test 41 at 2.8 ° C but lower than Test 37 at 9.9 ° C. Therefore Test 43 is higher than each similar test in one ambient category, but lower in the other while the turbulence intensity is almost double that recorded in either of the other tests. Once again, it appears that the measurement of an unsteady flow by the CSAT3 is occurring, as the measured turbulence intensity is far greater than what is expected from a relatively slow ambient flow.

Ambient temperatures (Column 4) and wind speeds (Column 5) reported in Table 4.1 are average values determined from the Waterloo Region weather data taken over the duration of each fire test. It can be seen that ambient temperature ranged from 1 – 10 º C across all tests. Ambient wind speed ranged from 0.5 – 4 m/s fairly consistently blowing in the E-SE direction.

Table 4.1 Ambient and Turbulent Conditions for Tests with no Blocking Object present

Test #	Wind Speed (m/s)	Turbulence Intensity (%)	Ambient Temperature (C)	Ambient Wind Speed and Direction (m/s)	False Floor Present
40	3.0	11.0	5.8	2.5 E-SE	No
44	3.0	11.2	1.4	0.6 E	Yes
36	4.6	12.5	9.6	1.4 E-SE	No
38	4.6	12.0	8.9	2.6 SE	Yes
37	7.1	12.7	9.9	1.8 E-SE	No
41	7.1	11.0	2.8	3.9 SE	No
43	7.1	19.2	4.3	3.4 SE	Yes
39	10.0	12.1	5.3	2.1 SE	No
42	10.0	13.3	5.2	3.4 S-SE	Yes

4.3.2 Fuel Regression Rate Measurements during Fire Tests without a Blocking Object present

Once the background flow through the facility and ambient conditions were characterized, the live fire test series were conducted. Important fire characteristics such as fuel regression rate, heat flux and temperature were measured under each test condition outlined in Table 4.1 above.

Two different measuring techniques were implemented to determine liquid fuel regression rate, as this is one of the most important parameters for characterizing fire behaviour

and the potential hazard of a fire to its surrounding environment. The first technique, and one employed previously for determining fuel regression rate in large fires [10], involves the use of three load cells positioned under the corners of the fuel pan burner that measure the rate of change of the mass of fuel with time after ignition. The second technique employs a sight glass to monitor changes in the level of fuel in the pan, and hence the rate of change of fuel volume in the pan, as a function of time.

A typical time trace of the decrease in fuel mass as a function of time as determined using the load cells is shown in Figure 4.17. The major features in the figure are similar to those recorded via the time trace of fluid height in the sight glass as well.

The fuelling of the pan is seen in Figure 4.17 as the initial steady upward slope. There is a pause in the fuelling as one barrel was emptied and replaced with a new barrel. At close to -4 minutes, which denotes 4 minutes before ignition, the first fan is turned on to 34 Hz in this experiment. Ignition of the fire occurs at 0 minutes and all fans are on and at full speed soon after a time of 1 minute as marked on the plot. A steady state burning period begins (SOSS) approximately 5 minutes after ignition. The start time of this steady state period is determined using thermocouple data recorded on the rakes positioned downwind of the pan burner to determine when the conditions near the fire have reached steady state. Since the steady state period for the load cells may be out of phase with that seen for the thermocouples, it is important to graph each set of load cell data versus time in order to determine if the steady state period ascribed by the thermocouples is appropriate for interpretation of the load cell data. The end of steady state burning (EOSS) occurs at approximately 7 minutes after ignition. Soon after that, at 12 minutes after ignition, the flame is completely extinguished.

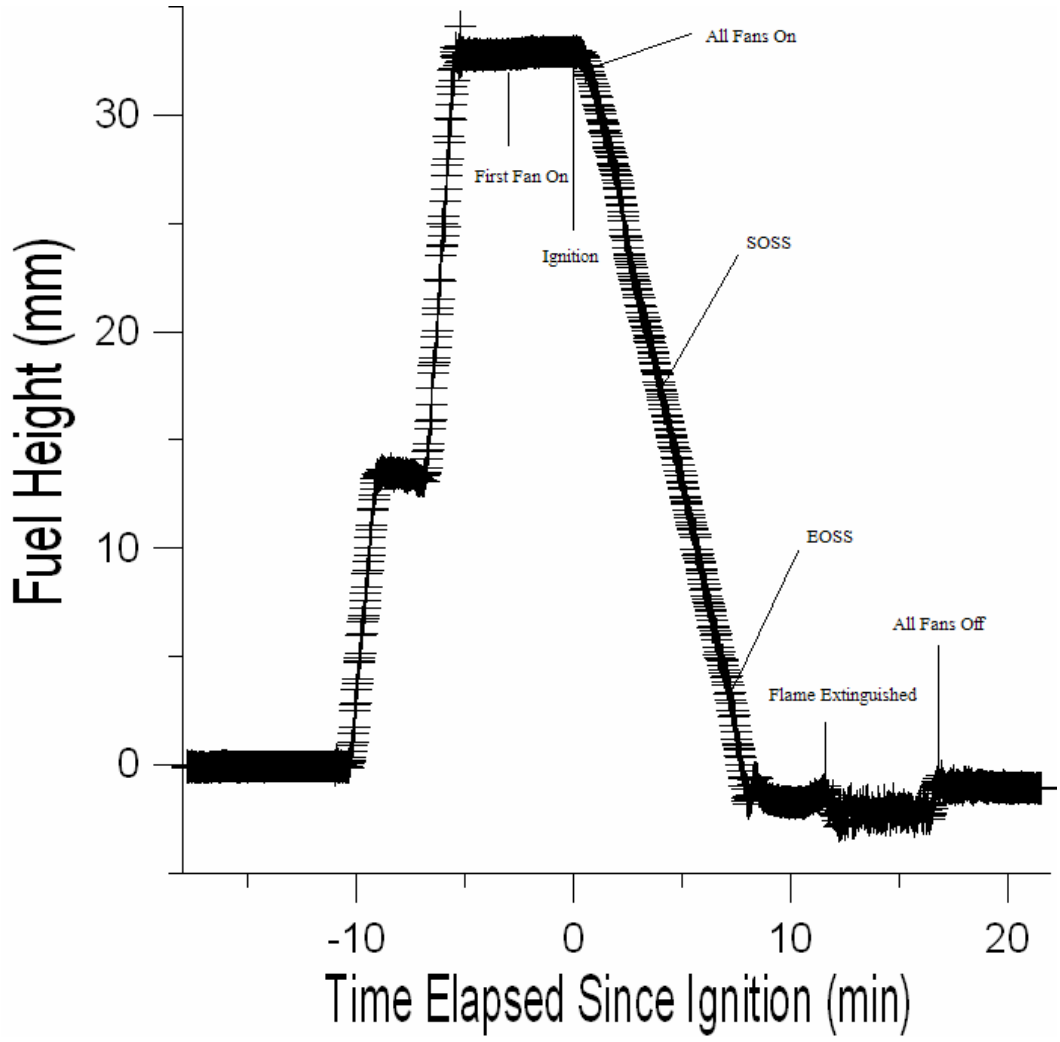

Figure 4.17 Typical Time Trace of Fuel Regression Rate obtained from Load Cell Data

The water mass/level, as measured by the load cells, had not returned to its original pre-test level even after all the fans had been shut off. The deficit was estimated to be an average of 3.3 kg of water. It was assumed that some water evaporated from the water substrate during the fire. Alternately, or additionally, some of the water may have been ejected from the pool due to localized boiling and spattering as the fuel layer became very thin and the fire died down. Such a loss of water is consistent with the observed change in load cell trace. In both cases, also, the change in initial mass of the water plus pan burner, occurs after the end of the steady state burning period and is not expected to affect the fuel regression rate values reported here [10].

Another notable phenomenon in this graph is the apparent increase in fuel depth after the fans have been turned off. This occurs in every test to a varying degree, usually suggesting an increase in fuel level of 1.3 - 1.5 mm. This was also noted by Randsalu [10] who observed that the increase in fuel depth occurred when the fans were initially turned on and remained throughout the steady state burning period. It was determined therefore, that this effect was a constant while the fans were in operation and would not negatively affect the fuel regression rate measurements. The test series with no Blocking Object conducted here provided some insight into the cause for this phenomenon. The configuration of bricks and floor around the fire pan was different for the tests with and without a Blocking Object in order to accommodate the new experimental setup. The setup for the case without a Blocking Object allowed more air to pass underneath the fire pan during a test, as rows of fire bricks in front of the concrete blocks designed to protect the floor were removed. With this new configuration, the fuel depth was observed to increase by 3 to 3.5 mm after the fans were shut off at the end of a test. On the other hand, when the false floor was put into place, even without the Blocking Object present, the apparent increase in fuel depth after the fans were turned off dropped to the values of 1.3 to 1.5 mm seen in earlier tests when the Blocking Object was present. In building the floor up around the pan, the amount of air blockage underneath the pan was increased restricting the free flow of air under the pan. When air was able to freely travel underneath the pan (no false floor, no Blocking Object), the upward force on the pan due to increased pressure from the air flowing under the pan increased, resulting in less weight on the load cells, which, in turn corresponded to an apparent decrease in fuel depth. When the underside of the pan was obstructed, less air flowed through and the upward force decreased resulting in less apparent decrease in the fuel depth. Fortunately, since fan speed is kept constant throughout a test, the upward force exerted on the

pan due to air flow under the pan is expected to be a constant for any given test and any given floor configuration, so should have little effect on the steady state fuel regression measurements of interest here.

Values for fuel regression rate measured using the load cell for all wind and floor configurations are presented in Table 4.2. The average value of FRR from both tests performed with a crosswind of 7.1 m/s and no false floor present is also listed. The total uncertainty in this data is ± 0.4 mm/min as only load cell measurements are used [10].

Table 4.2 Summary of Fuel Regression rate results from the Test Series with No Blocking Object Present

Wind Speed (m/s)	False Floor FRR (mm/min)	Normal FRR (mm/min)
3.0	3.8	4.4
4.6	4.2	3.5
7.1	4.3	3.8
10.0	5.2	4.4

There are no values of FRR listed for the sight glass method in Table 4.2 because they were found to be considerably lower than (as low as half of the value of) those measured using the load cells. It is suspected that serious errors in the regression rates deduced from the sight glass data resulted from air bubbles being trapped in the tube connecting the sight glass to the fuel pan, as well as a "kink" made in the long sight glass connection tube that occurred during cleaning and reinstallation. Therefore, the following discussion is based on data for fuel regression rate measured using the load cells under the fuel pan.

Verification for the integrity of the load cell results was found by comparing the weight of fuel added to the pan determined by the load cell system with the weight of fuel added to the pan found using an independent scale during the fuelling process. The comparative values of fuel weight measured using the load cells and the scale are summarized in Table 4.3 for all tests except Test 44 in which there was a problem with the scale.

Table 4.3 Measured Fuel Quantities using Load Cells and a Scale for each Test during the Test Series with No Blocking Object

Test #	Load Cell Fuel Weight (kg)	Scale Fuel Weight (kg)
36	79.7	79.8
37	80.6	80.0
38	86.5	82.1
39	81.4	81.0
40	88.0	79.8
41	73.8	73.5
42	74.0	73.8
43	63.8	63.7

A comparison of the initial weights listed in Table 4.3 indicate that for most tests differences between the weight of fuel measured by the load cell and by the scale fell within the range of uncertainty of ± 1.5 kg previously reported for the load cell measurements [10]. Exceptions occurred for Tests 38 and 40 in which the load cell measurements suggested that, respectively, 4 kg and 8 kg more fuel was put into the pan than the amount measured by the scale. The reason for this discrepancy is unclear; therefore load cell results from Tests 38 and 40 will be carefully scrutinized in terms of their use in the following discussions. The agreement between load cell and scale measurements seen in most of the tests, however, attests to the integrity of the load cell data for use in determination of fuel regression rate.

It can be seen from Table 4.2 that fuel regression rate is not independent of the detailed geometric configuration in the facility, as the fuel regression rate increases as the wind speed increases when the false floor is present, while no such trend exists when the false floor in not present. Values of FRR measured with the false floor present around the fuel pan appear to be slightly higher than those determined when there was no false floor installed, except at the lowest wind speed. With the false floor present, the highest fuel regression rate was 5.2 mm/min in the 10 m/s wind while that without the false floor was about 15 % lower at 4.4 mm/min. The lowest fuel regression rates occurred at the lowest wind speed of 3.0 m/s - 3.8 mm/min when the false floor was present but at the second lowest wind speed without the false floor present. Fuel regression rates measured at intermediate wind speeds are very close to each other, measuring 4.2 mm/min at 4.6 m/s and 4.3 mm/min at 7.1 m/s with the false floor and 3.5 mm/min at 4.6 m/s and 3.8 mm/min at 7.1 m/s when there was no false floor present in the facility.

The difference in measured fuel regression rate when the false floor is present and when it is not present is caused by changes in the local flow conditions around the fire with and without the false floor and their resulting effects on fire plume behaviour. In the previous wind characterization section, it was shown how the flow around the fuel pan is more homogeneous and the turbulence intensity is lower when the false floor is in place. Consistent with this, from visual observations during a fire test, the fire plume is swept downwind when the false floor is present [Figure 4.18], whereas the plume splits up and there is a great degree of flame attachment to the upwind side of the fuel pan during a test without the false floor present [Figure 4.19].

Figure 4.18 A Fire Plume during the No Blocking Object test with no upwind flame attachment due to the presence of the False Floor

Figure 4.19 A Fire Plume during the No Blocking Object test with upwind flame attachment due to no False Floor being present

Such differences in fire plume behaviour result in the inconsistent fuel regression rate results seen when the false floor is not in place, and the steadily increasing fuel regression rates as the wind speed increases and the false floor is in place due to the difference in heat feedback to the fuel surface, which will be more thoroughly explored in the subsequent section. However, due to a lack of testing performed with a false floor in place, it is not known whether these trends would continue with repeated testing.

In terms of repeatability of the results, two tests were performed at a wind speed of 7.1 m/s without a false floor in the facility. Results differed by 19%, with measured values of 3.4 mm/min and 4.1 mm/min respectively using load cell data. Taking into account the estimated uncertainty of ± 0.4 mm/min in measured fuel regression rate for both values, the lower result could be considered reasonable and within the bounds of uncertainty; however, with the overall consistency observed in other measured values of fuel regression rate, additional factors that could have led to such variability were also examined. Higher ambient and fuel temperatures have previously led to increases in values of measured fuel regression rate [10]; this would not be a factor in these measurements since it is the lower value of regression rate, 3.4 mm/min, which was measured on a day where the ambient temperature was 7.1 ° C higher. The ambient wind conditions external to the test facility were higher during the test that resulted in the higher value of measured fuel regression rate, 4.1 mm/min; however, with the controlled cross wind conditions inside the facility, it is not likely that this would contribute to such considerable changes in measured fuel regression rate values. Load cell time traces for each test have very consistent steady state periods and no other visual anomalies. Therefore, since no known variation in the ambient test conditions appeared to cause the differences in fuel regression rate, and the load cells were functioning properly, the variation between tests at the same wind speed

must be attributed to variations in the nature of the fire plume when the false floor is not in place; however, as mentioned previously the results still fall within the expected range of uncertainty. This is not unexpected, as most large scale pool fire studies produce a large variation of test results with little repeatability in fuel regression rates despite using the same test conditions [64].

4.3.3 Test Conditions during Fire Tests with a Blocking Object present

Twenty-three 2m diameter JP-8 spill fire tests were conducted under four distinct crosswind speeds ranging from 4.7 – 13.5 m/s with the Blocking Object present in the facility. Multiple tests were performed at each wind speed. Table 4.4 summarizes the wind speed as well as the ambient conditions for each of these fire tests. The rows in the Table are ordered from lowest to highest crosswind velocity, although in reality this was not the order in which the tests were conducted. No turbulence intensity data is available for this test series, as the CSAT3 had not been purchased at the time of these tests.

The first column in Table 4.4 contains the reference test number for a particular fire experiment. In Column 2, the crosswind velocity for each test is documented, as determined by the average steady state velocity measured by the span of bidirectional probes mounted directly upwind of the fuel pan at x = 2 m. Ambient temperature and wind speeds, which are listed in the next two columns, are average values of the Waterloo Region weather data over the duration of the fire test. It can be seen that ambient temperature ranged from approximately -1 – 15 º C across all tests. Ambient wind speed ranged from 1.8 – 4.8 m/s with most tests having the wind consistently blowing in the E-SE direction. However, some tests have wind in the W-NW direction due to a change in wind direction during the test.

Table 4.4 Ambient Conditions for Tests with a Blocking Object present

Test #	Wind Speed (m/s)	Ambient Temperature (C)	Ambient Wind Speed and Direction (m/s)
14	4.7	5.4	2.8 E
17	4.7	8.7	2.4 E-SE
20	4.7	12	3.5 W-NW
27	4.7	15.2	4.8 SE
32	4.7	15.3	1.8 E
13	7.3	5.1	2.2 E
15	7.3	8	3.0 E-SE
19	7.3	12	3.9 N-NW
28	7.3	5.2	2.2 S-SE
31	7.3	14.5	1.9 S
12	10.5	5.5	2.6 E
16	10.5	7.7	2.9 E
18	10.5	11.2	4.3 SW
26	10.5	12.9	4.5 SE
29	10.5	10.5	2.1 SE
5	13.5	0.4	3.5 E-SE
6	13.5	-0.2	3.8 E-SE
7	13.5	-0.9	3.3 E-SE
8	13.5	-1.2	3.0 E
21	13.5	13.3	2.8 E-NE
22	13.5	13	3.1 E-SE
25	13.5	8.8	3.3 SE
30	13.5	13.1	2.5 E-SE

Important fire characteristics such as fuel regression rate, heat flux and temperature were measured under each test condition outlined in Table 4.4. The final test results, as well as the effects of each of these factors on the final data are presented in the following sections.

4.3.4 Fuel Regression Rate Measurements during Fire Tests with a Blocking Object present

As in the live fire tests with no Blocking Object in the facility, both load cell and sight glass methods were implemented to determine liquid fuel regression rate for fire tests with the Blocking Object. Values for fuel regression rate measured using both methods for all wind speeds are presented in Table 4.5. Tests are listed according to wind speed, with the test number provided for reference. One test, Test 26, only has fuel regression rate data from the load cells, as there was a problem with the sight glass method in this test.

Table 4.5 Fuel Regression Rate Results of the Live Fire Test Series with a Blocking Object present using the Load Cell method and the Sight Glass method

Test #	Wind Speed (m/s)	FRR (Load Cell Method) (mm/min)	FRR (Sight glass Method) (mm/min)
14	4.7	4.7	4.2
17	4.7	4.7	3.6
20	4.7	4.7	4.1
27	4.7	4.5	3.1
32	4.7	4.5	4.5
13	7.3	4.7	3.9
15	7.3	4.3	3.6
19	7.3	4.4	3.8
28	7.3	4.4	4.3
31	7.3	4.7	3.1
12	10.5	4.7	4.9
16	10.5	5.4	4.2
18	10.5	4.7	4.4
26	10.5	4.6	n/a
29	10.5	5.4	3.0
5	13.5	4.3	3.7
6	13.5	4.5	4.8
7	13.5	4.6	4.8
8	13.5	4.5	4.9
21	13.5	5.5	4.8
22	13.5	5.7	4.2
25	13.5	5.1	3.8
30	13.5	6.0	4.2

In order to compare the fuel regression rate results at each test wind speed, the percent difference from each test compared to the average fuel regression rate at that wind speed is presented in the following table [Table 4.6]. Results from the load cells and sight glass measurements are presented. The total uncertainty in the load cell fuel regression rate data is ± 0.4 mm/min, while the sight glass data is slightly more accurate with an uncertainty of ± 0.3 mm/min [10].

Table 4.6 Percent Difference of Load Cell and Sight Glass Fuel Regression Rate measurements from the Test Series with a Blocking Object Present

Test #	Wind Speed (m/s)	Percent Difference (Load Cell Method)	Percent Difference (Sight glass Method)
14	4.7	1.7	7.4
17	4.7	1.7	8.0
20	4.7	1.7	5.0
27	4.7	2.6	22.9
32	4.7	2.6	14.3
13	7.3	4.3	4.2
15	7.3	4.5	3.8
19	7.3	2.2	1.6
28	7.3	2.2	13.9
31	7.3	4.3	18.7
12	10.5	5.4	17.2
16	10.5	8.5	1.8
18	10.5	5.4	6.5
26	10.5	7.5	n/a
29	10.5	8.5	31.6
5	13.5	15.5	17.3
6	13.5	11.0	8.7
7	13.5	8.8	8.7
8	13.5	11.0	10.8
21	13.5	9.0	8.7
22	13.5	12.6	4.7
25	13.5	1.5	14.6
30	13.5	17.7	4.7

When Table 4.6 is examined, the percent differences are lower overall for the load cell method than the sight glass method. The maximum percent difference seen in the load cell measurements is 15.5 %, compared to more than twice that at 31.6 % for one sight glass measurement. While it is not true in every case, the load cell percent differences increase as the

wind speed increase, going from a maximum of 2.6 % at the lowest wind speed of 4.7 m/s to the previously mentioned 15.5 % at the highest wind speed of 13.5 m/s. At the intermediate wind speeds, the percent difference increases to a maximum of 4.5 % at 7.3 m/s and 8.5 % at 10.5 m/s. The sight glass percent difference results are much more varied, with no real pattern as the wind speed increases. The second highest percent difference of 22.9 % occurs at the lowest speed of 4.7 m/s.

The mean, minimum and maximum values of fuel regression rate measured using the load cells are summarized in Table 4.7 for tests run under the same wind speed with the Blocking Object present. The uncertainty in this data is ± 0.4 mm/min as only load cell data is used [10].

Table 4.7 Statistical Data from fuel regression rates with a Blocking Object Present using Load Cell Data

Wind Speed (m/s)	Mean FRR (mm/min)	Minimum FRR (mm/min)	Maximum FRR (mm/min)
4.7	4.6	4.5	4.7
7.3	4.5	4.3	4.7
10.5	5.0	4.6	5.4
13.5	5.0	4.3	6.0

Mean fuel regression rates measured for each wind speed condition are similar, as are the minimum values. The maximum recorded fuel regression rates covered a much wider range of values however. At the slowest wind speed, 4.7 m/s, the mean, minimum and maximum values of fuel regression rate were very similar: 4.6 mm/min, 4.5 mm/min and 4.7 mm/min respectively. At the next slowest wind speed, 7.3 m/s, the measured mean fuel regression rate was slightly

lower than that for the slowest wind speed, 4.5 mm/min, while the maximum measured fuel regression rate was the same at 4.7 mm/min. The minimum fuel regression rate, however, dropped to 4.3 mm/min. At the next higher wind speed of 10.5 m/s, the mean fuel regression rate increased to 5.0 mm/min, with minimum and maximum values of 4.6 mm/min and 5.4 mm/min respectively. Finally, at the highest wind speed of 13.5 m/s, the mean regression rate was again 5.0 mm/min. For this wind speed, however, the minimum and maximum recorded fuel regression rates were farther apart, at 4.3 mm/min and 6.0 mm/min respectively.

While the mean fuel regression rates reported in Table 4.7 are similar, the values of minimum and maximum fuel regression rate indicate that depending on the wind speed there can be a considerable difference in fuel regression rate measured in two tests conducted at the same wind speed. At the slowest wind speed, 4.7 m/s, mean, minimum and maximum values of fuel regression rates lay within ± 0.1 mm/min of one another, with little test to test variation. As wind speed is increased to 7.3 m/s this range increases slightly. For further increase in wind speed to 10.5 m/s and then 13 m/s, the mean fuel regression rate increased to 5 mm/min, with increasing variability in results for tests conducted even at the same nominal wind speed. For example, at the highest speed, 13.5 m/s, the maximum measured fuel regression rate of 6.0 mm/min is 140 % higher than the minimum value of 4.3 mm/min. Tests at the intermediate speeds of 7.3 m/s and 10.5 m/s vary less than tests at 13.5 m/s, but there is still a marked difference between the minimum and maximum recorded fuel regression rates. These observed test to test differences in measured fuel regression rate will first be compared to those seen in the sight glass measurements, and then correlated against other possible test variables in the subsequent sections.

The mean, minimum and maximum values of fuel regression rate measured using the sight glass are summarized in Table 4.8 for tests run under the same wind speed with the Blocking Object present. The estimated uncertainty in this data is ± 0.3 mm/min as only sight glass data is used [11]. Comparing the data from Table 4.7 to that in Table 4.8 for the same wind speed, it is evident that the values of fuel regression rate measured using the sight glass are lower than those recorded using data from the load cells. In particular, the minimum values of regression rate determined using the sight glass data are significantly lower than those from the load cells - this would clearly also bias mean values calculated based on the sight glass data.

Table 4.8 Statistical Data from fuel regression rates with a Blocking Object Present using Sight Glass Data

Wind Speed (m/s)	Mean FRR (mm/min)	Minimum FRR (mm/min)	Maximum FRR (mm/min)
4.7	3.9	3.1	4.5
7.3	3.7	3.1	4.3
10.5	4.1	3.0	4.9
13.5	4.4	3.7	4.9

Despite the offset in values, overall trends seen in Table 4.8 are similar to those shown in Table 4.7 for the load cell data. Mean fuel regression rates are similar across wind speeds, decreasing slightly for increased speed, from 4.7 m/s to 7.3 m/s, then increasing again for the two higher speeds. Unlike the load cell results, the maximum value of mean fuel regression rate is seen for the highest wind speed, 13.5 m/s. The values of minimum and maximum fuel regression

rates again show considerable variation between wind speeds. The minimum fuel regression rate is relatively constant for the 3 slowest speeds increasing in value for the maximum values of wind speed. The maximum value of fuel regression rate generally increased with increasing wind speed until leveling off at a value of 4.9 mm/min at wind speeds of both 10.5 m/s and 13.5 m/s. For these data, unlike those from the load cell measurements, the difference between minimum and maximum measured fuel regression rates peaks at the wind speed of 10.5 m/s with a 137% difference between the values. In order to more thoroughly understand these observed test to test differences in measured regression rates, the possible influence of ambient conditions on fuel regression rate will first be examined.

4.3.5 Fuel Regression Rate and Ambient Conditions during Fire Tests with a Blocking Object present

In order to determine possible relationships between fuel regression and ambient conditions, the weather data from the Region of Waterloo was used to determine the effects on measured fuel regression rate, if any, of the magnitude and direction of ambient winds external to the facility, of ambient temperature and of the number of tests performed in a day. In previous research, there was some controversy over the relationship between ambient temperature and measured fuel regression rate, since increases in ambient temperature have resulted in both increases and decreases in the fuel regression rate in different live fire tests [10, 37]. Other ambient effects, such as the number of tests performed in a day have also been observed to affect fuel regression rate measurements [10], as both the test environment and the water substrate in the pan burner do not necessarily have the time to cool down completely between tests, and a

subsequent test in a warm environment and with a heated water substrate may appear to have a higher fuel regression rate [10]. Finally, in the UW Facility, it is not known if ambient wind conditions external to the facility will have an effect on measured fuel regression rates. The effect on the present results of each of these factors is outlined in the following sections.

In Figure 4.20, measured fuel regression rate is plotted against ambient wind speed external to the facility for each test at each of the four cross wind speeds. While the test to test scatter in both the load cell data and the sight glass data are evident in these plots, no clear trends can be seen to indicate an effect on measured FRR of ambient wind speed external to the facility. Due to the fact that fuel regression rate data is usually scattered in this manner during similar large scale pool fire testing [64], this does not mean that the ambient conditions are not affecting the pool fires, however the exact effect is difficult to quantify.

The ambient temperature outside the UWLFRF is plotted versus measured fuel regression rate for all tests at all four cross wind speeds in Figure 4.21. From these graphs, it appears that there is no strong relationship between the outside ambient temperature and measured fuel regression rate. For fires in cross winds of 4.7, 7.3 and 10.5 m/s, the ambient temperature does not appear to systematically affect the fuel regression rate. The only visible relationship between ambient temperature and measured FRR appears for the maximum wind speed, 13.5 m/s, in which an increase in ambient temperature corresponded with an increase in the fuel regression rate for the load cell data. At this wind speed, however, the sight glass data does not indicate the same trend. As mentioned previously, the scattered fuel regression rate results are not unexpected, and the lack of a trend in the data does not mean that the ambient wind speed does not affect the fires inside the UWLFRF.

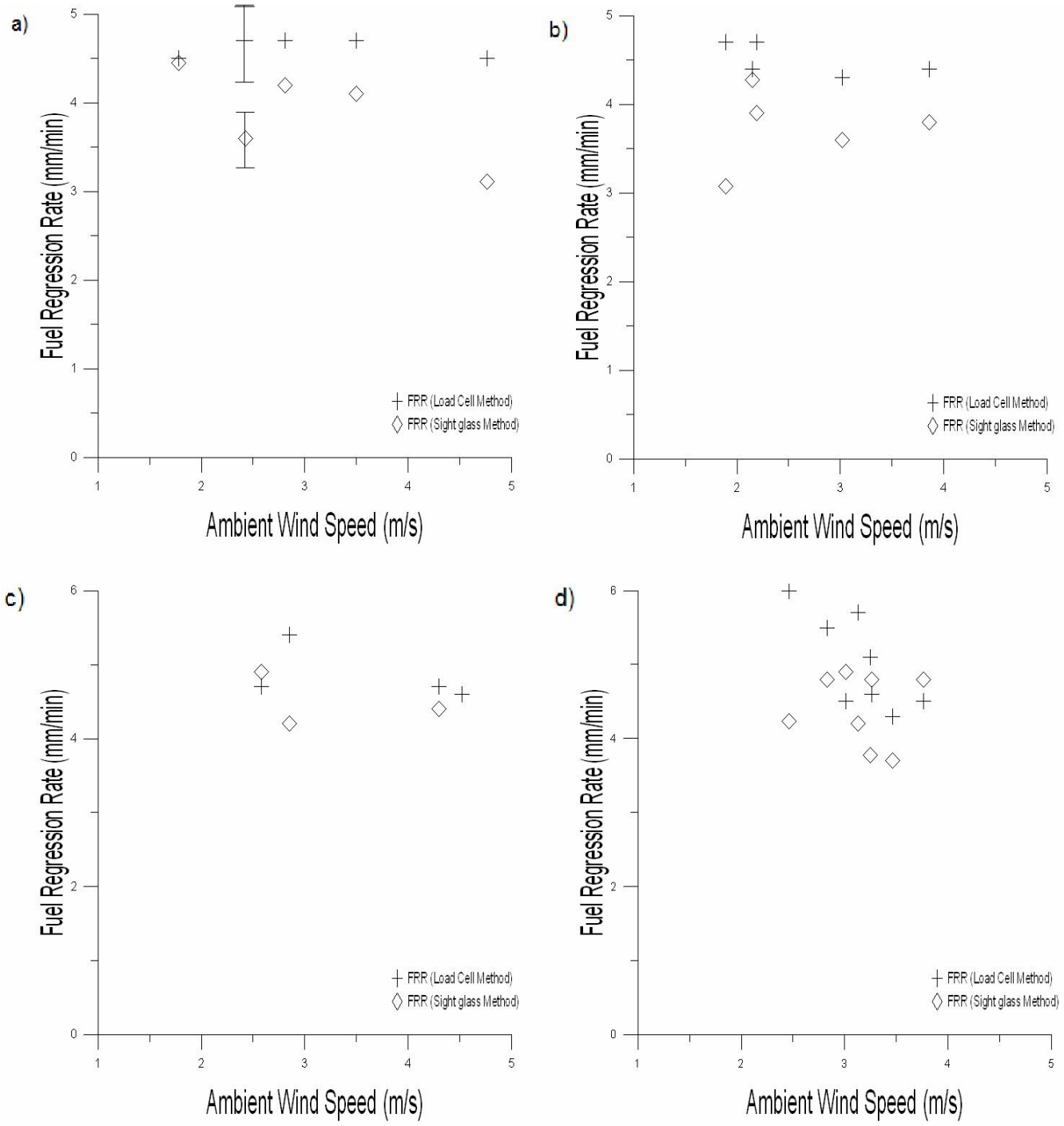

Figure 4.20 Ambient Wind Conditions outside of the UWLFRF compared to the fuel regression rate of the Test Series with a Blocking Object Present at wind speeds of a) 4.7 m/s b) 7.3 m/s c) 10.5 m/s d) 13.5 m/s

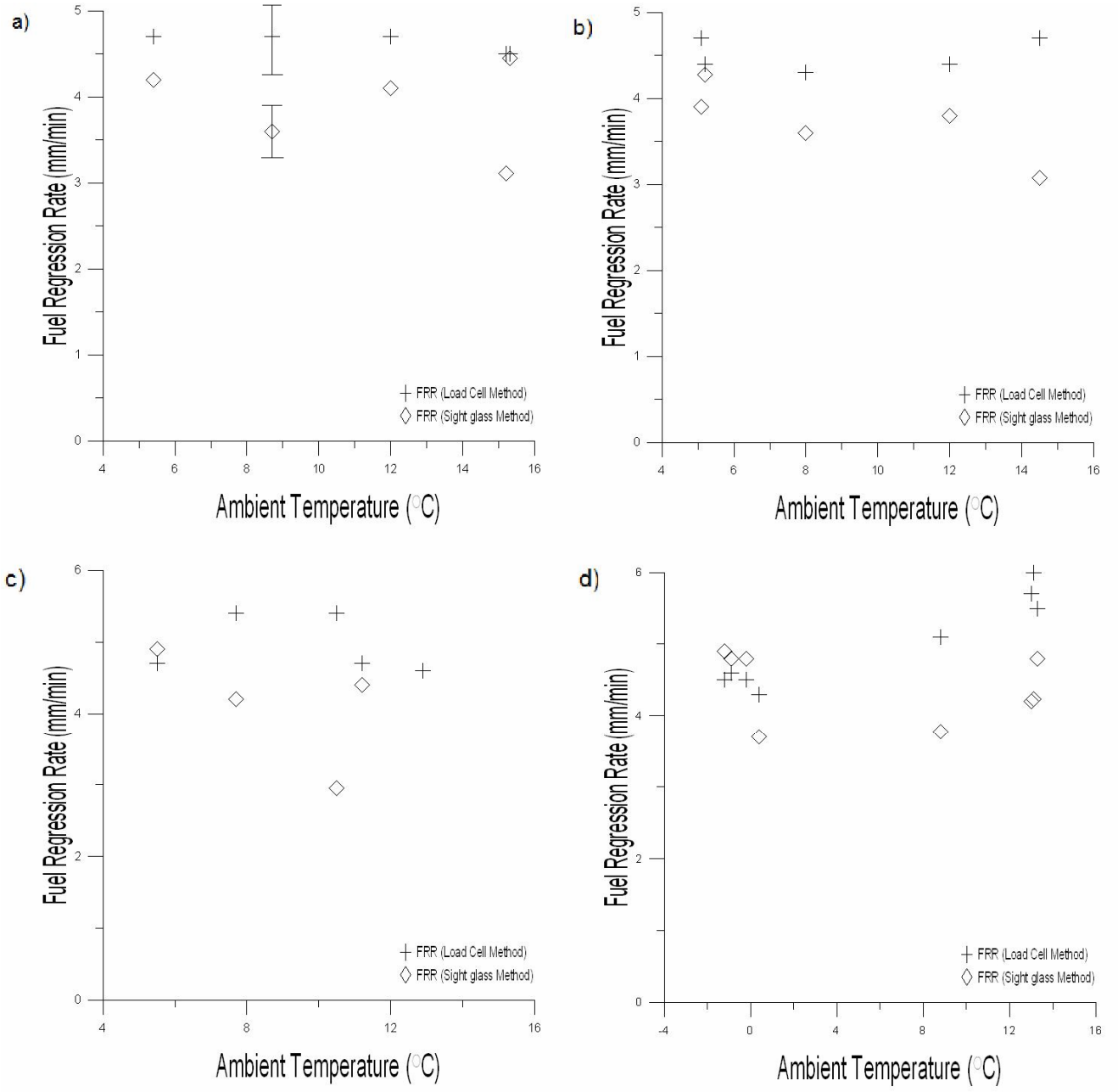

Figure 4.21 Ambient Temperature outside of the UWLFRF plotted against measured fuel regression rate of the Test Series with a Blocking Object Present at wind speeds of a) 4.7 m/s b) 7.3 m/s c) 10.5 m/s d) 13.5 m/s

The number of tests performed in a day has previously had an effect on measured values of fuel regression rate [10], but no strong relationships between the test number and fuel regression rate become apparent here for the fire tests conducted at the same wind speeds. Subsequent tests on days with multiple tests did not appear to result in elevated values of fuel regression rate as compared to other tests conducted with the same setup and wind speed. On some testing days, tests were performed with less than an hour between each test such as Test 18, 19 and 20, whereas on other testing days there were multiple hours between each test, such as Test 29, 30 and 31. Neither case lead to increasing values of fuel regression rate although clearly the water substrate during this second sequence had much more time to cool down between tests even though the same number of tests were performed. Previously, a thermocouple had been present in the water substrate, allowing direct measurement of the temperature of the water before each test. Unfortunately, it was removed for these tests; in order to study this effect further, it should be replaced as it would provide valuable temperature data.

Overall, for the fires reported here, there is no strong relationship between fuel regression rate and ambient wind data, ambient temperature or number of tests performed in a day. Such relationships may exist, but in these experiments other mitigating factors, such as the lack of consistent fuel regression rates at similar testing conditions, are masking the effects so that there is no clear impact on measured values of fuel regression rate.

Since the initial temperature of any objects involved in a fire test is known to have an effect on overall fire behaviour, the ambient temperature at the time of ignition is important. In these tests, however, it may not have been the most important temperature. The temperature of the fuel, the water substrate and the Blocking Object itself were other temperatures which also influenced the behaviour of the fire. Unfortunately, the fuel and substrate temperatures were not

available for these tests. Possible effects of variations in the Blocking Object temperature will be explored more thoroughly in the following section when the heat fluxes in the fuel pan area are examined.

Overall, the ambient conditions did not appear to have a large effect on the fuel regression rate of the pool fires with a Blocking Object present. The negligible effect of the ambient wind is not surprising, as the tests are conducted indoors with large fans generating the wind on the fire. The ambient temperature has been shown to have an effect on the fuel regression rate during previous testing at the UWLFRF [10], but as mentioned previously, there are other factors in the large pool fire which could overwhelm the contribution of ambient temperature. Finally, the number of tests conducted on a given day did not have a noticeable effect on the fuel regression rate, but may warrant further investigation.

Given that the ambient conditions did not appear to fully explain observed variability in values of fuel regression rate measured with the Blocking Object present, the overall fire behaviour was examined to see if there was visual evidence that could explain the effects noted. This forms the subject of the next section.

4.4 Fire Behaviour with the Blocking Object present

When examining the results from the test series with a Blocking Object present, it is useful to break the fire tests down into two different classifications based on the crosswind speed: fast (wind speed > 7.3 m/s) and slow (wind speed ≤ 7.3 m/s). This is done as the fires appear to behave differently in these two situations. Lam [8] and Randsalu [10] have noted that at slower wind speeds, the fire plume attached itself to the bottom of the Blocking Object [Figure

4.22] and wrapped around both the downwind and the upwind sides of the object. This is different than the behaviour of the fire plume under faster wind speeds, where the fire plume did not attach to the Blocking Object, but instead passed cleanly underneath. [Figure 4.23].

Figure 4.22 Slow Speed Fire Attached to the Blocking Object

Figure 4.23: Fast Speed Fire Passing Under the Blocking Object

For the slow wind speed fires in the test series with a Blocking Object present, the fires in a wind speed of 4.7 m/s had slightly higher fuel regression rates than the fires in a wind speed of 7.3 m/s. Through analysis of the videos of the live fire tests, it appears that the 4.7 m/s fires, as seen in Figure 4.22 displayed more attachment to the Blocking Object than the 7.3 m/s fires [Figure 4.24] where more of the fire plume traveled under the object instead of becoming attached to it as seen in the following figures.

Figure 4.24 7.3 m/s Fire passing under the Blocking Object

This flame attachment could result in more heat being radiated back towards the fuel surface from the heated culvert, thereby increasing the fuel regression rate at lower wind speeds. On the other hand, increasing the wind speed will increase the availability of air for entrainment and combustion, leading to a more intense burning which could also increase the fuel regression. Increasing the wind speed did result in more flame tilt as the fire plume passed under the culvert however, as seen in the previous figures. This increased flame tilt results in less heat being radiated back from the fire plume itself to the fuel surface compared to the slower speed 4.7 m/s fire, and therefore a lower fuel regression rate despite the possibility of increased more intense combustion due to increased wind speed. When examining the fires in wind speeds of 10.5 m/s or 13.5 m/s in the Test Series with a Blocking Object present, there is a trend of increasing fuel

regression rate with increasing wind speed. In the load cell data, there appears to be a relatively large variation between individual tests especially at 13.5 m/s wind speed which had a lower minimum, 4.3 mm/min and a higher maximum fuel regression rate, 6.0 mm/min, than fires tested in 10.5 m/s wind, which had minimum and maximum regression rates of 4.6 and 5.4 mm/min respectively. Based on the sight glass measurements, the maximum regression rate was 4.9 mm/min for fires tested at both wind speeds, but the minimum regression rate recorded for tests at 10.5 m/s was 3.0 mm/min, which is quite a bit lower than the minimum sight glass fuel regression rate of 3.7 mm/min from fires tested at 13.5 m/s. Since the fire plume passes relatively cleanly under the object for both cases, it is not expected that the object will have the same effect on FRR seen in the fires tested in low speed winds. Instead, for these cases the proximity of the fire plume to the ground may have some effect on the fuel regression rate. Fires subjected to the 10.5 m/s winds passed under the object but still with a slight degree of interaction with the object [Figure 4.25]. On the other hand, fires in crosswinds of 13.5 m/s pass under the culvert without any visible interaction and lie very close to the ground, as if the flame has been pressed into the ground [Figure 4.26].

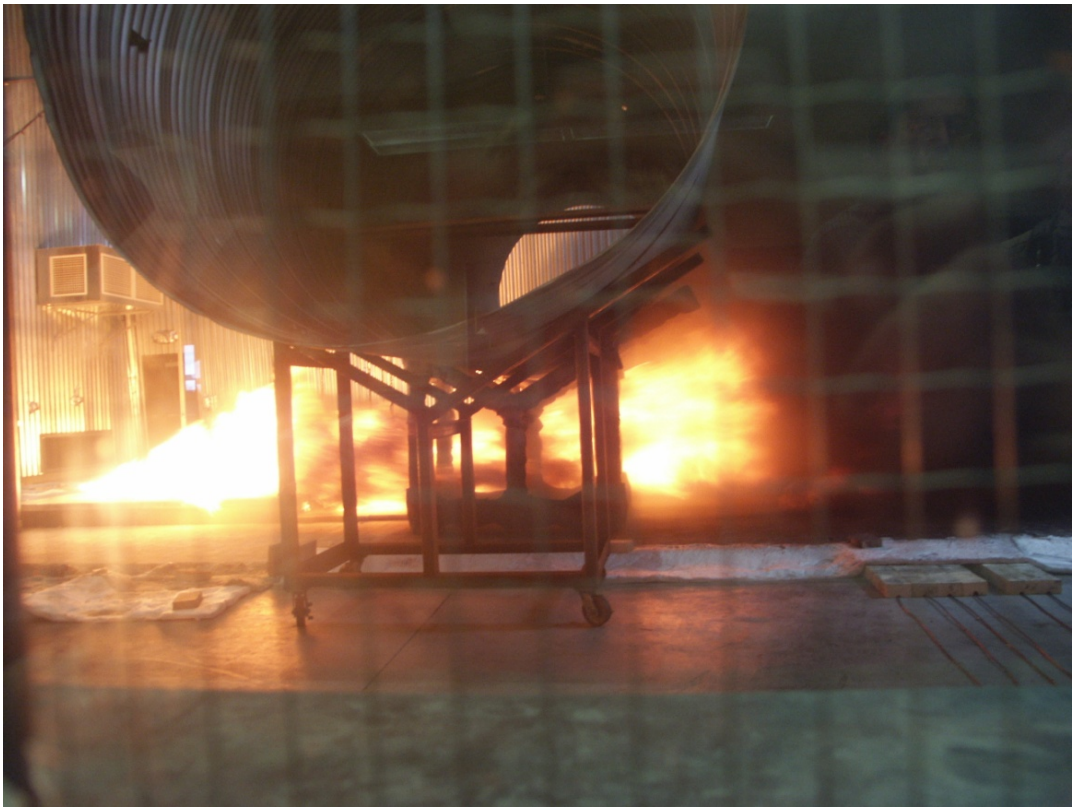

Figure 4.25 Fast Speed Fire with Some Attachment to the Culvert evident

Figure 4.26 Fast Speed Fire with No Culvert Attachment evident

The load cell results will be used while discussing trends seen the fuel regression rate measurements, as the load cell system has proven to be more reliable throughout both testing series. The average fuel regression rate of tests at 10.5 m/s and 13.5 m/s is the same; however, when the individual test data is examined, it can be seen that the 13.5 m/s fires have the highest recorded fuel regression rates, but also the most variance between tests. The primary difference between the two fires at different wind speeds are in the interaction with the Blocking Object and the wind itself. A fire at 10.5 m/s will heat the Blocking Object, increasing radiation back to the fuel surface, and increasing the fuel regression rate. Such heating of the Blocking Object does not occur to the same extent at 13.5 m/s, but the increased wind speed increases mixing between fuel vapours in the fire and the ambient air causing strong combustion near the fuel surface, increasing the fuel regression rate. The flame tilt increases slightly as the wind speed increases to 13.5 m/s, but as seen in the previous figures, fires at both wind speeds are already at a very acute angle compared to a fire in quiescent conditions, and the expected change in radiation due to flame tilt is minimal. The average fuel regression rate of both of these fires is the same using the load cell method, and while the highest fuel regression rates are recorded at the highest wind speed of 13.5 m/s, the results at this wind speed are very inconsistent compared to the results at 10.5 m/s. This could be caused by the influence of the wind on fires at 13.5 m/s, whereas at 10.5 m/s the effect of the Blocking Object is more pronounced and moderates apparent variability due to the wind and its effect on the fuel regression rate.

4.4 Comparison of Fuel Regression Rates from the cases with and without the Blocking Object

Now that both sets of fuel regression rate data have been presented, from the Test Series without a Blocking Object present and with a Blocking Object present, comparing the two sets of results will provide further insight on the effect of the Blocking Object on the fuel regression rate of the pool fire. Data from tests with and without the false floor are also presented, to examine the effect of the false floor compared to the effect of the Blocking Object. Data from the highest wind speed of 13.5 m/s from the Blocking Object tests will be excluded as there is no data at this crosswind speed for tests with no Blocking Object to provide a comparison.

Table 4.9 provides information about the fuel regression rate of three different configurations: tests without the Blocking Object present but with a false floor, tests without either the Blocking Object or false floor present, and tests with the Blocking Object present. The overall uncertainty is ± 0.4 mm/min, as only load cell data is used.

Table 4.9 Fuel Regression Rates of All Three Configurations within the Test Enclosure grouped by Wind Speed

Wind Speed (m/s)	FRR (mm/min) measured by Load Cells		
	False Floor	No False Floor	Blocking Object
3.0	3.8	4.4	4.6
4.6	4.2	3.5	4.5
7.1	4.3	3.8	5.0
10.0	5.2	4.4	5.0

As can be seen in Table 4.9, when the Blocking Object was removed and the false floor was put into place, the fuel regression rate began to consistently increase with increasing wind speed. The overall fire behaviour also changed drastically for this situation. There was no longer evidence of the fire attaching to the upwind side of the pan, as the entire plume was swept downwind. The differences are most clearly seen in the heat flux measurements taken in the fuel pan, which will be presented in the next section. Based on these results, the lack of a false floor in the test series with the Blocking Object may also be one of the causes that contribute to the large observed variations between fuel regression rate data taken in different tests at the same wind speed. Other causes, as mentioned above, may include the temperature of the Blocking Object and the water substrate. The effect of all of these factors on the fuel regression rate of the fire will be further explored in the next section, which will examine the heat flux data measured in and around the fire.

4.5 Heat Flux Results

In previous sections, the wind flow through the UWLFRF was first characterized at several cross-sections for 5 different wind speeds, with and without the Blocking Object present downwind of the fuel pan burner. Then, fuel regression rate measurements made during live fire tests under different wind conditions were discussed. Based on differences in the measured flow distributions and fuel regression rates (Section 4.3.4), it is evident that the large Blocking Object in the facility greatly influences local mixing and heat flux distribution in the fire. For example, since the steady state fuel regression rates measured using the load cells were lower when there

was no Blocking Object present [Table 4.5], it is thought that the object itself absorbs heat and re-radiates it towards the surface of the liquid fuel thereby increasing the heat flux within the fire and, in turn, leading to increased fuel regression rates. Similarly, when the false floor was put into place the upwind attachment mechanism and overall behaviour of the fire changed drastically, which would again change the heat flux distribution around the fire. The different levels of heat flux entering and leaving the fire in each of these scenarios are examined in this section, grouped according to cross wind flow conditions, in order to facilitate comparison between the different configurations tested. Using this data, relationships between heat flux and fuel regression rate of the fire will be explored.

4.5.1 Blocking Object versus No Blocking Object Tests

The heat flux from the fire to the surface of the Jet A fuel has been identified as one of the most important measurements related to fire behaviour in large fuel pan burners [54 - 56]. As mentioned in Section 3.2.4, for this study, Directional Flame Thermometers (DFTs) and Hemispherical Heat Flux Gauges (HFGs) are placed within the fuel pan to measure mixed radiative and convective flux from the fire gases to the surface of the fuel. Both instruments have estimated uncertainties lying in the range of ±5% of measured heat flux [8, 91]. This can be much higher, however, depending on the nature of the environment in which the gauge the immersed under test conditions. During high wind conditions and in the presence of a large, optically thick hydrocarbon fire such as the one presented in this thesis, the DFT uncertainty ranges between 25 - 27 % while the HFG uncertainty ranges from 21 - 31 %. These uncertainties will be used for the heat flux data that follows. During similar heat flux measurements with low-

wind conditions, the uncertainty for the two gauges ranges from 27 - 40 % for the DFT and 24 - 42% for the HFG [9].

Two different layouts of heat flux gauges in the fuel pan were used in these experiments: one for the test series with the Blocking Object present, and a different one for tests without the Blocking Object in place. During tests with the Blocking Object, two HFGs were positioned 0.5 m upwind and downwind of centre, and on the centre-line of the fuel pan. The last HFG was on the +y side, at a distance of 0.5 m and an angle of 45° from the center of the fuel pan. One DFT was placed directly at the center of the pan; the other was adjacent to the HFG 0.5 m downwind of the center. In tests without the Blocking Object, only two gauges - the DFT and HFG situated side by side at 0.5 m downwind of the center of the pan - were used to record heat flux data in the pan. In all cases, the heat flux from the main fire plume and surroundings to the surface of the fuel and the heat flux leaving the surface were measured as functions of time. In the following figures, 'HFG and DFT heat flux' denotes the heat flux from the fire measured by the top plate of either device. 'DFT heat flux up' denotes the heat flux from the fuel surface as measured by the bottom plate of the DFT. Pan heat flux measurements from all the gauges for fires tested at all wind speeds, with and without the Blocking Object present, are discussed in the next several sections.

4.5.2 Heat Flux Results with No Blocking Object Present

In this section, measured values of heat flux from the DFT and HFG located 0.5 m downwind of the fuel pan center are reported for tests conducted with no Blocking Object, with and without the false floor in place. As noted previously, the presence of the false floor visibly

changed the behaviour of the fire [Figure 4.18] compared to the situation with the floor present [Figure 4.19]. In Figure 4.19, the fire attaches to the upwind portion of the bricks around the fuel pan, as seen in the bottom left corner of the figure. The fire plume itself doesn't appear to be smooth, as if there is a great deal of motion occurring in multiple directions. This is in contrast to Figure 4.18, where no evidence of upwind flame attachment exists and the fire plume is being swept back with little evidence of motion in other directions. The flame tilt angle is also more drastic in Figure 4.18 with the false floor present than in Figure 4.19.

Therefore, due to this visual difference in the fires, the heat flux data for each floor configuration will be considered separately. Due to the limited number of tests performed, rather than taking data across a series of different tests, heat flux data is averaged across the steady state burning period for each fire as determined by thermocouple readings [9].

Results of measured heat flux from both gauges for fire tests with no false floor present are plotted in Figure 4.27 against the wind speed employed for each test. Heat flux estimated using temperature data from the DFT are on average 16% higher than those measured using the HFG, but values are relatively consistent across wind speeds, averaging 105.2 kW/m^2 with a maximum of 113.1 kW/m^2 at a wind speed of 10.0 m/s and a minimum of 100.7 kW/m^2 at a wind speed of 7.1 m/s. In contrast to data from the DFT, measurements taken using the HFG suggest marginally increasing heat flux to the surface of the fuel with increasing wind speed, although again the values are quite consistent across the range of wind speed tested. The HFG recorded an average heat flux of 88.8 kW/m^2 across tests, ranging from only 84.1 kW/m^2 at a wind speed of 3.0 m/s to 100.0 kW/m^2at the maximum wind speed of 10.0 m/s used in this configuration. A relatively constant heat flux with increasing wind speed in this case is consistent with the idea that there is upwind flame attachment when the false floor is not present, as seen in Figure 4.19.

An attached flaming zone near the base of the fire would tend to result in a relatively homogeneous 'burning' region near the surface of the fuel rendering heat flux values independent of wind speed. The discrepancies in measured values of heat flux between the DFT and HFG can be attributed to conduction losses internal to the HFG seen in previous tests [9, 83]. To some extent these losses would be mitigated by the fact that the HFG came to equilibrium over the steady burning period; but will still result in a lower measured heat flux when compared to results from the DFT which comes to equilibrium with the surrounding environment much more quickly than the HFG and does not suffer from internal losses due to conduction.

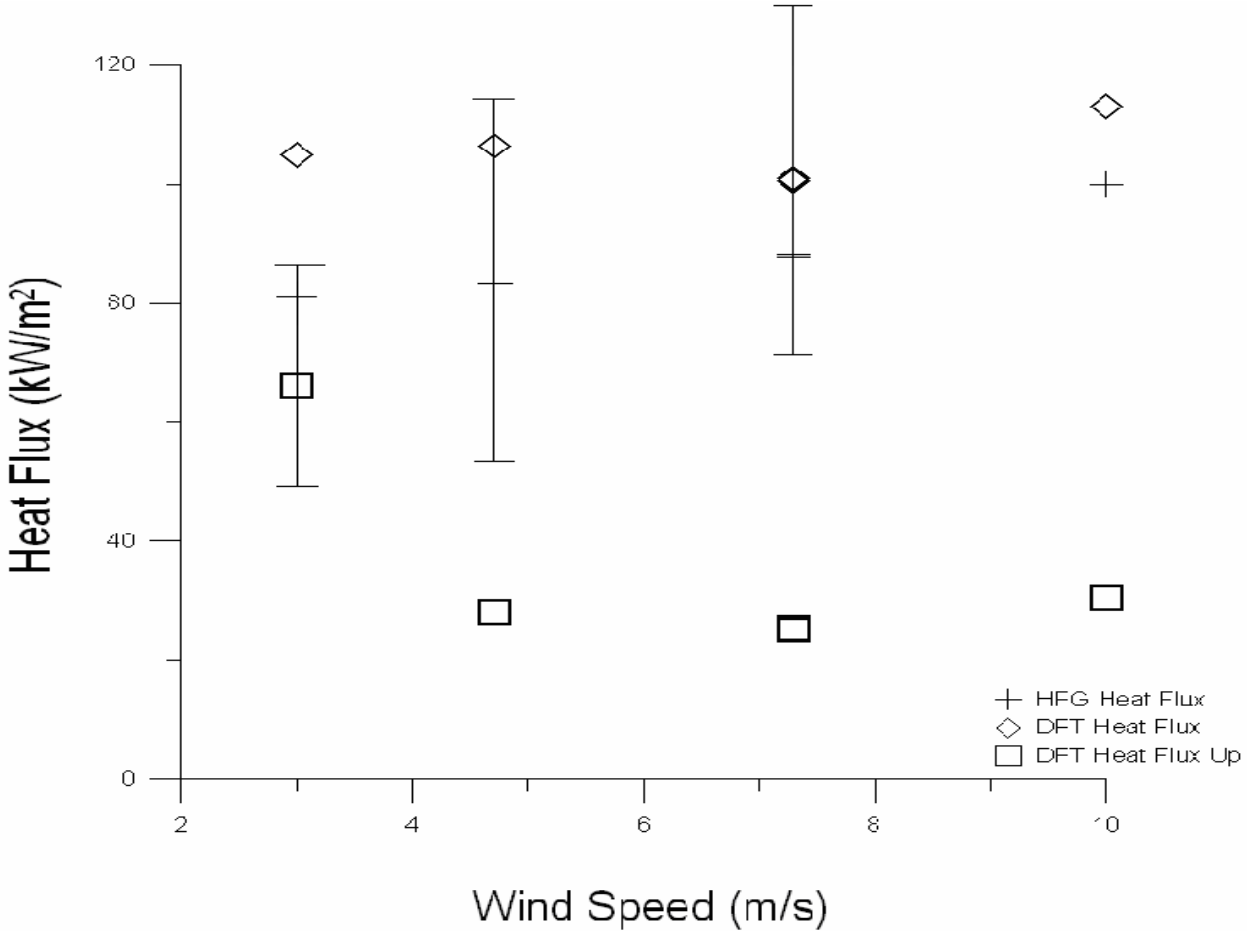

Figure 4.27 Centerline Heat Flux Results 0.5m Downwind from the Pan Center for the Test Series with No Blocking Object and No False Floor

Error bars are positioned on all three measurements, however it can be seen that the top plate DFT heat flux error bar extends outside of the graph range up to a maximum of 131.2 kW/m^2 as the maximum error for the top plate of the DFT is ± 30.5 kW/m^2. The bottom plate of the DFT has considerably less maximum error of ± 17.9 kW/m^2. The HFG has a similar amount of error as the top plate of the DFT, measuring ± 31.0 kW/m^2. The downward facing surface of the DFT located 0.5 m downwind of the pan center is positioned such that it records heat flux from the surface of the fuel back towards the bottom face of the gauge. As shown in Figure 4.27, the average value of heat flux to this face is 35.1 kW/m^2; however, this value will be somewhat influenced by the highest recorded heat flux which corresponds to the slowest wind speed, 3.0 m/s, and is almost twice that level, 66.2 kW/m^2. All other values of heat flux are similar, with the lowest recorded heat flux, 25.1 kW/m^2, found for an intermediate wind speed of 7.12 m/s.

The trend in heat flux values measured on the bottom face of the DFT gauge suggests that with increasing wind speed, the bottom plate is exposed to less heat flux from the fuel. As the wind speed increases, the fire plume tilts towards the ground as the buoyant forces within the fire becomes are dominated by the momentum of the crosswind flow. At the lowest wind speed, the fire is almost off the pan and the bottom plate of the DFT is not engulfed in flames, so directly measures the heat flux leaving the surface of the fuel. As the fire plume tilts over with increasing wind speed, the fire in the pan gets closer to the fuel surface and the DFT is engulfed in flames. Therefore, at wind speeds of 4.7 m/s and faster, the DFT is engulfed in flames and measures a heat flux closer to that of the fire plume than heat flux from the fuel surface.

Results of measured heat flux from both gauges for fire tests with a false floor present are plotted in Figure 4.28 against the wind speed employed for each test. As was seen in the heat flux measured by the two gauges with no false floor present, heat flux measured using the top

plate of the DFT is slightly higher than that recorded using the HFG. The average heat flux measured using the DFT is 56.0 kW/m^2, with a maximum of 67.7 kW/m^2 observed for the slowest wind speed and a minimum 45.9 kW/m^2 at the fastest wind speed. The HFG beside it recorded an average heat flux of 54.1 kW/m^2, with a maximum of 71.2 kW/m^2 at the slowest wind speed and the minimum 45.6 kW/m^2 at the fastest wind speed approximately equal to that recorded by the DFT, at the same speed.

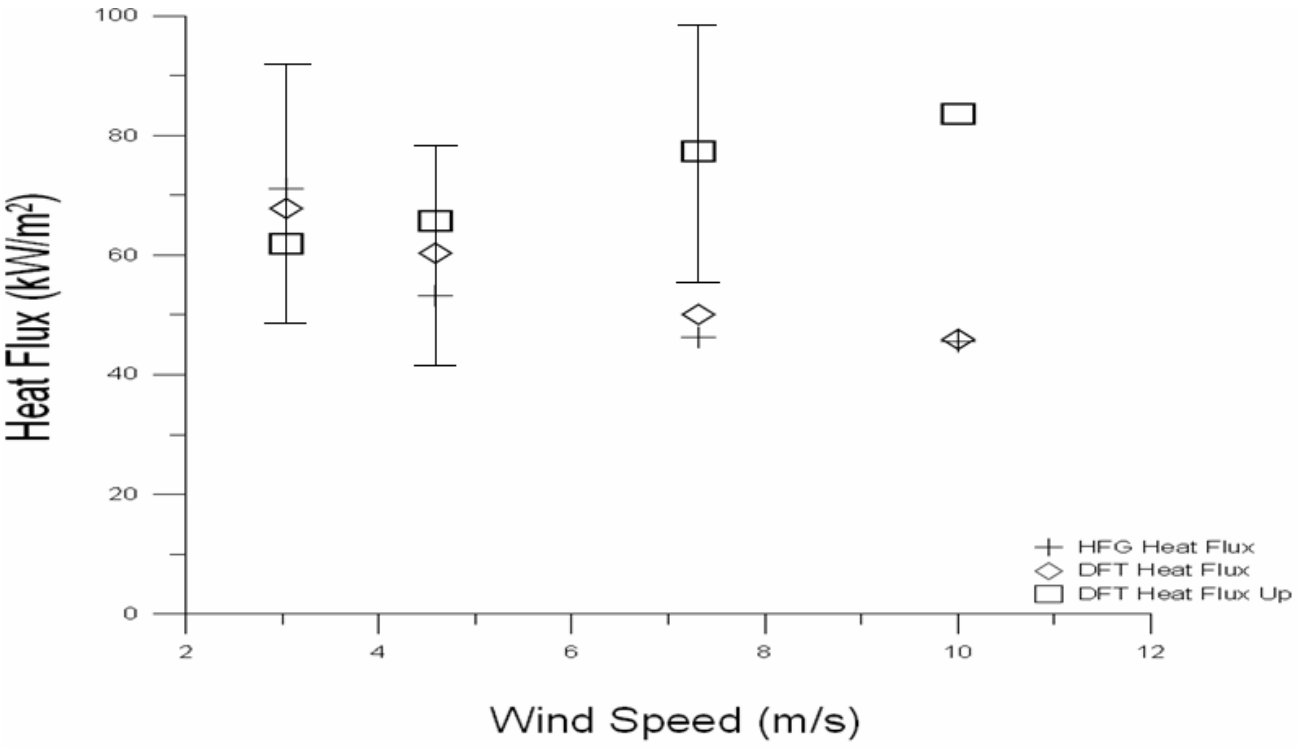

Figure 4.28 Centerline Heat Flux Results 0.5m Downwind from the Pan Center for the Test Series with No Blocking Object and a False Floor

When the false floor is present, the dynamics of the fire change considerably, as shown in Figures 4.18 and 4.19. The entire fire plume bends down and the angle of tilt becomes more pronounced with increasing wind speed. Less heat flux is registered by both the DFT and the HFG as the wind speed increases, since the majority of the windswept fire plume sits farther away from the gauges, oriented at an angle where radiative heat flux is significantly reduced compared to that in a quiescent fire. Error bars are placed on points for all three gauges. The top plate of the DFT and the HFG have very similar maximum amounts of error, measuring ± 22.6 and ± 22.1 kW/m^2 respectively. The bottom plate of the DFT has less possible error, measuring ± 18.3 kW/m^2.

In contrast to the previous results, during these experiments heat flux to the bottom plate of the DFT was on average 72.2 kW/m^2, but steadily increased with increasing wind speed. At the slowest wind speed, 3.0 m/s, the measured heat flux was 62.0 kW/m^2, increasing to 83.7 kW/m^2 at the highest wind speed of 10.0 m/s. It should be noted that at 3.0 m/s, the measurement of the bottom plate of the DFT in the buoyancy-dominated fire is very similar to the results from tests when the false floor and blocking object were not in place at that wind speed, which was measured to be 66.2 kW/m^2. At wind speeds of 10.0 m/s, the heat flux measured on the bottom plate of the gauge is almost twice the heat flux measured by the top plate of the gauge. These results can be explained by the tilt of the fire plume under differing wind speeds. As the speed increases, the angle of tilt of the flames increases until at 10.0 m/s the fire plume actually passes underneath the bottom plate of the DFT according to thermocouple results, causing an increase in the heat flux measured by the bottom plate. This same phenomenon results in a decrease in heat flux to the top plates of the DFT and the HFG, as their measuring surfaces are exposed to less flame as the angle of tile of the fire plume increased until

the fire plume passed under the DFT. However, despite the fact that the tests with a false floor present show promising trends with regards to heat flux and wind speed, not enough tests have been performed to determine if this trend stands up to repeated testing.

4.5.3 Comparison of Heat Flux and Fuel Regression Rate

Since the heat flux is thought to directly influence the fuel regression rate in a fire, plotting values of heat flux measured in each fire test against measured fuel regression rate for that test should provide more insight into the relationship between the two properties. Figures 4.29 and 4.30 show such results for the test series with no Blocking Object, again broken down into those tests without the false floor present and those with a false floor.

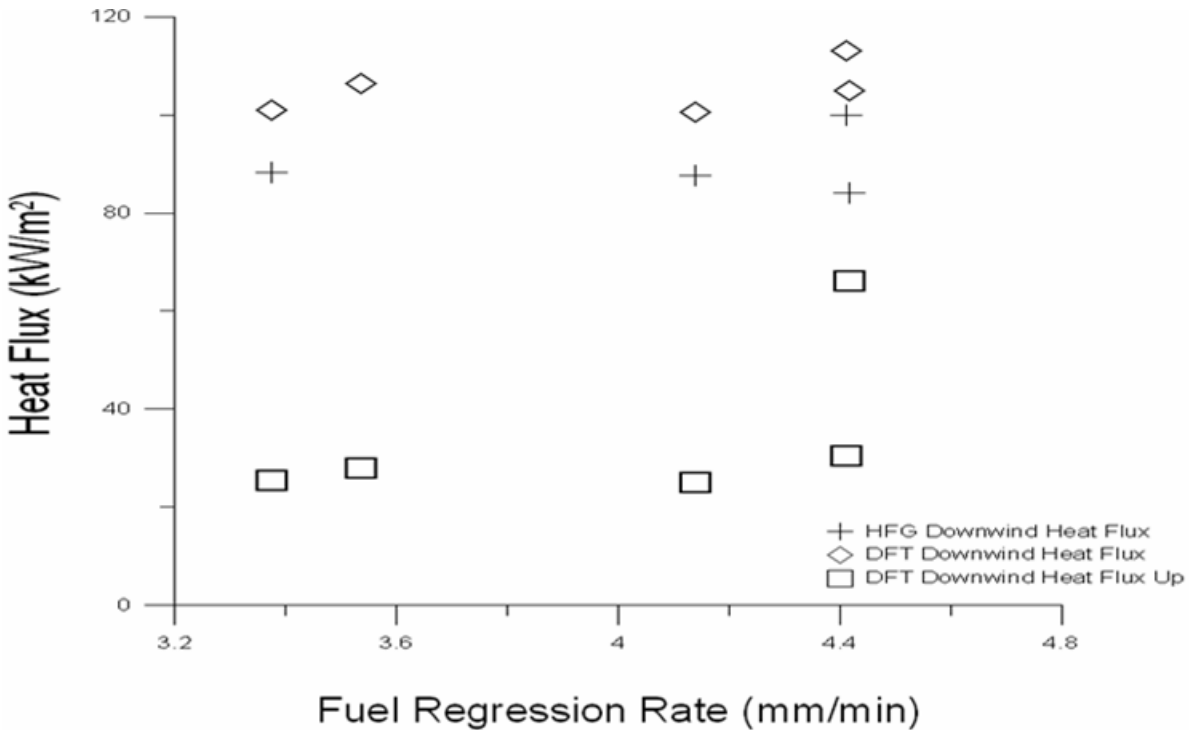

Figure 4.29 Heat Flux Results during the Test Series with no Blocking Object present and no False Floor compared to the Fuel Regression Rate measured using Load Cells

The results without the false floor, Figure 4.29, indicate almost constant values of heat flux correspond to all measured values of fuel regression rate. This figure has the same total uncertainty as Figure 4.27. As discussed in Section 4.3.1, two tests were performed at a wind speed of 7.1 m/s without a false floor present. These appear in Figure 4.29 at fuel regression rates of 3.4 mm/min and 4.1 mm/min respectively. Despite the differences in measured fuel regression rate, the steady state heat flux measured during these two tests is almost identical with the HFG recording 88.3 kW/m^2 and 87.6 kW/m^2 in Tests 37 and 41 respectively. The DFT results were even closer, with Test 37 recording 100.9 kW/m^2 and 25.5 kW/m^2 on the top and bottom plates, while during Test 41 the DFT recorded 100.7 kW/m^2 and 25.1 kW/m^2 on the top and bottom plates.

Another comparative set of data are the two tests that have almost identical fuel regression rates, measured at 4.4 mm/min. These two tests correspond to fires exposed to the lowest and highest wind speeds, 3.0 m/s and 10.0 m/s respectively. The HFG and the top plate of the DFT record higher heat flux for the 10.0 m/s wind speed test than during the test occurring at 3.0 m/s. On the other hand, the bottom plate of the DFT records a higher heat flux during the test occurring at 3.0 m/s. This DFT measurement is due to the characteristics of the buoyancy-dominated fire at that wind speed compared to a faster speed fire affected by the momentum-dominated wind as discussed in the previous section. The buoyancy-dominated fire sits higher above the fuel pan, so the bottom plate of the DFT records the heat flux leaving the fuel surface, whereas the momentum-driven fire in a higher crosswind engulfs the DFT in flames, increasing the recorded heat flux over only that leaving the pool surface. However, at 3.0 m/s, the buoyancy-dominated upward traveling pool fire is not swept back by the wind and is traveling

upwards, which causes the bottom plate of the DFT to measure higher amounts of heat flux than at higher speeds, where more of the flame is swept back onto the top plate of the DFT and HFG.

As mentioned previously, variations in overall fire plume behaviour due to the lack of a false floor during these tests seems to have led to more unpredictable fuel regression rate and heat flux results. Only one testing condition, 7.1 m/s, could be repeated twice, and while these tests led to very similar values of measured heat flux, values of fuel regression rate were different. No clear explanation for this has emerged. Further no consistent trend between fuel regression rate and measured heat flux can be seen in Figure 4.29, which suggests that the fuel regression rate is dependent on more than just heat flux within the fire as measured by these gauges.

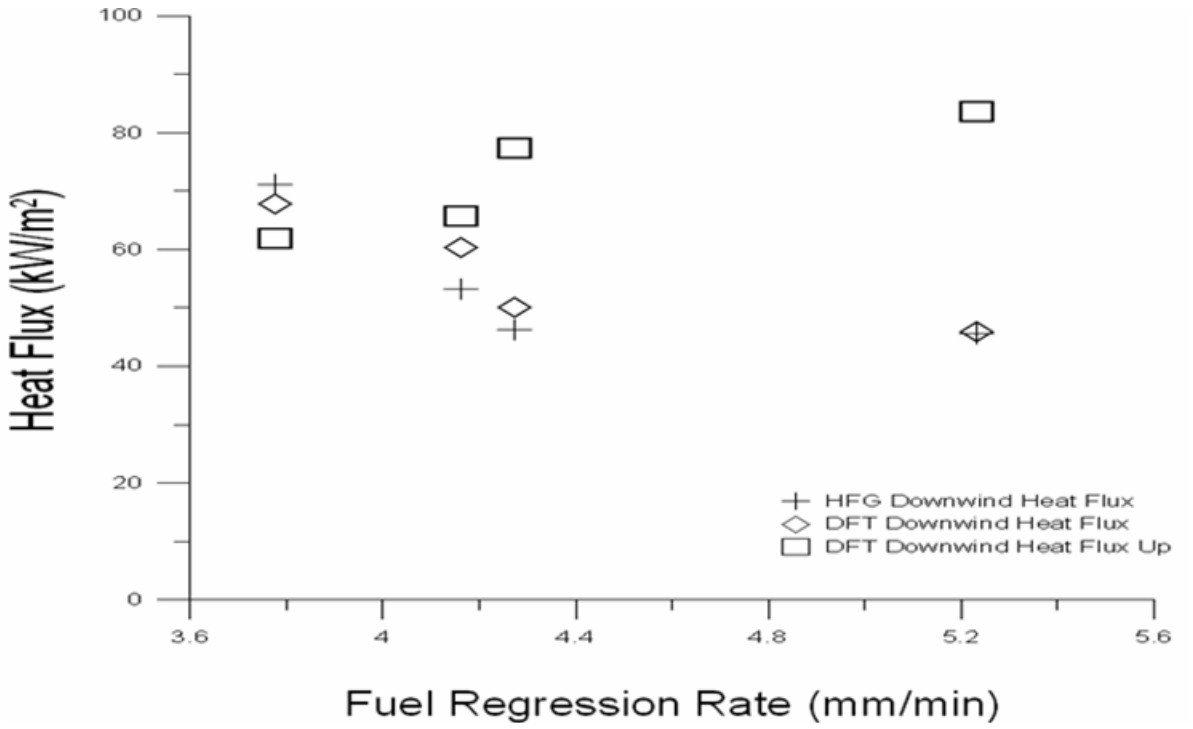

Figure 4.30 Heat Flux Results during the Test Series with no Blocking Object present and a False Floor compared to the Fuel Regression Rate measured using Load Cells

Figure 4.30 summarizes values of heat flux plotted against the fuel regression rates measured in tests for which there was a false floor present around the fuel pan. This figure has the same amount of total uncertainty in each measurement as Figure 4.28. Two trends are visible: as heat flux measured by the HFG and the top plate of the DFT decreases, measured values of fuel regression rate increase, and, in direct contrast, as heat flux measured by the bottom plate of the DFT increases, measured values of fuel regression rate also increase. These same trends were noted earlier for plots of heat flux versus wind speed since fuel regression increases with increasing wind speed in these tests. However, as noted earlier, not enough testing has been performed with this configuration in order to determine how strong these trends between heat flux, fuel regression rate and wind speed actually are.

4.5.4 Comparison of False Floor and No False Floor Results

When the tests with and without the false floor in place are examined, the effect of the false floor is evident. It has been seen previously that a floor surround can have an effect on fire behaviour [31, 35, 36, 56, 58], although the effect varies considerably depending on the detailed configuration and range of parameters used in a particular study. During these experiments the presence of the false floor caused three visible trends: as the wind speed increased, the heat flux measured by the bottom plate of the DFT increased, the heat flux measured by the top plate of the DFT decreased, and the fuel regression rate increased. This was because of the flame tilt and shape seen previously in Figure 4.18. As the tilt increased, the bottom plate of the DFT was exposed to more of the fire plume while at the same time the top plate was exposed to less of the flame as it passed under the gauge. The increased flame tilt increases the heat feedback to the

flame surface, which combines with enhanced mixing and entrained air at the higher wind speeds to increase the fuel regression rate.

None of the trends observed in the case with a false floor are evident when the false floor is no longer in place; for that configuration the only trend evident is a decrease in heat flux measured by the bottom plate of the DFT with increasing wind speed. A different, notable feature of the tests without a false floor are the relatively constant values of heat flux measured by the top plates of the DFT and the HFG throughout the experiments, suggesting that the heat flux from the fire plume gases to these gauges was not particularly sensitive to variations in wind speed nor did it entirely govern the final values of fuel regression rate. While upwind flame attachment, seen in Figure 4.19, may be argued to create a similar environment in the vicinity of the upper surfaces of these gauges at every wind speed, measured values of the other parameters will change because they are more susceptible to the effects of flame tilt as the wind speed increases. This is seen on the bottom plate of the DFT, as the angle of the flame tilt increases causing the bottom plate of the DFT to be exposed to less flame in the case where there is no false floor present. This is contrasted to the trends seen when the false floor was in place, because the fire plume traveled underneath the DFT when the false floor was present. Without the false floor present however, the fire plume is more elevated in the pan [Figure 4.19] and passes above the DFT. Overall, this comparison holds promise but more testing is required.

4.5.5 Heat Flux during Tests with the Blocking Object present

During testing with the Blocking Object present, more heat flux gauges were placed in the pan. This allowed for more comprehensive measurement of the heat flux to the fuel surface at

more locations in the pan burner, including on the upwind side of the pan. Heat flux measurements from each DFT will be presented separately, followed by the measurements from the HFG.

Results of measured heat flux from both sides of the DFT gauge placed in the centre of the pan for fire tests with a Blocking Object present are plotted in Figure 4.31 against the wind speed employed for each test. Heat flux to the top plate of the DFT was approximately constant across tests at all wind speeds, with an average value of 111.9 kW/m^2. Values of heat flux measured during tests at the lowest wind speed, 4.7 m/s, were highest, averaging 115.5 kW/m^2, with a standard deviation of 4.6 kW/m^2. Values dip slightly for the intermediate wind speeds, 7.3 m/s and 10.5 m/s, to 109.4 kW/m^2 and 108.4 kW/m^2 with standard deviations of 3.5 kW/m^2 and 5.4 kW/m^2 respectively, still very similar to the values recorded at other wind speeds. At a wind speed of 13.5 m/s, the value of heat flux of 113.4 kW/m^2, was slightly higher than for the intermediate speeds but lower than that recorded under 4.7 m/s winds. Heat flux data for this latter wind speed have a higher standard deviation, 7.8 kW/m^2, than any of the other tests due largely to Test 25 that recorded an average heat flux of 131.0 kW/m^2, the largest recorded for any of the tests.

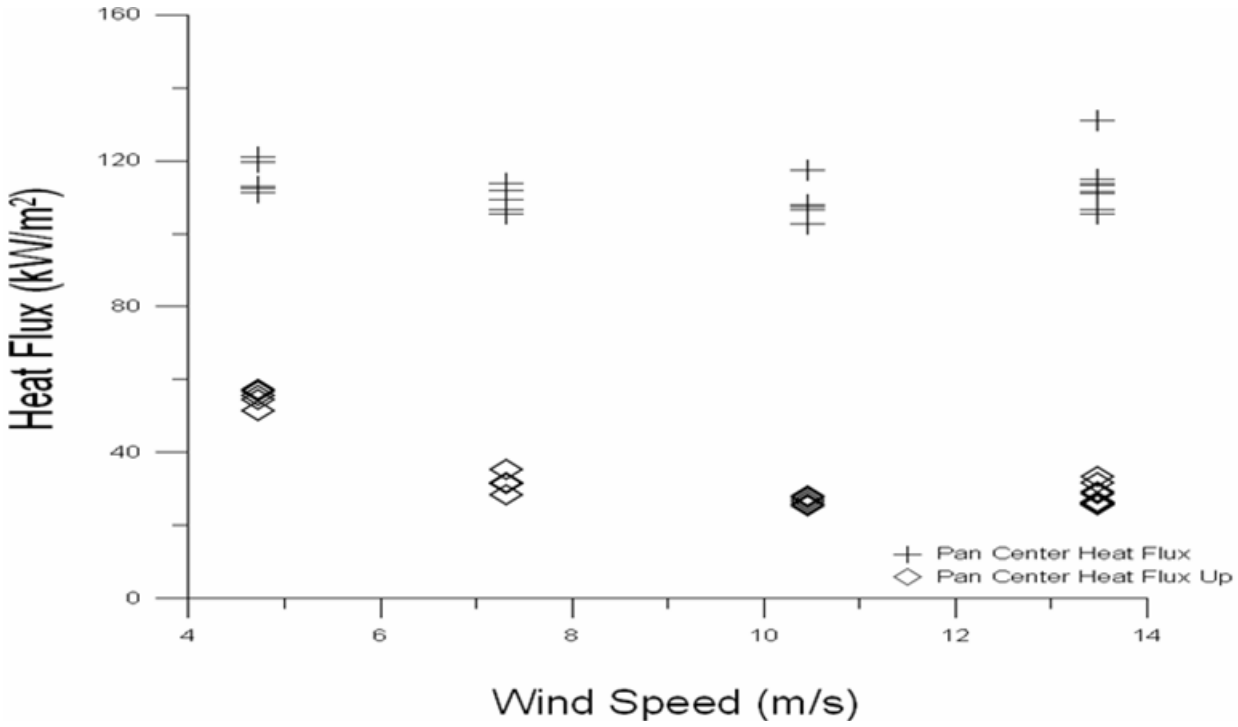

Figure 4.31 Pan Center DFT Heat Flux Measurements Versus Wind Speed in the Test Series with a Blocking Object Present

When examining the heat flux measured by the bottom plate of the DFT at the center of the pan [Figure 4.31], the highest values are all recorded at the lowest wind speed of 4.7 m/s. The average value of measured heat flux at this speed is 55.1 kW/m^2, compared to values of 31.7 kW/m^2, 26.8 kW/m^2, and 28.4 kW/m^2 at wind speeds of 7.3 m/s, 10.5 m/s and 13.5 m/s respectively. The standard deviations for these results are also all fairly low, with the largest standard deviation, 2.9 kW/m^2, occurring for the highest wind speed, 13.5 m/s. The average heat flux to the bottom plate of the DFT across all tests conducted at all wind speeds is 34.6 kW/m^2. Error bars are not placed on this graph due to the proximity of the points but the maximum error associated with the top plate DFT is ± 23.3 kW/m^2, while the bottom plate of the DFT has a maximum error of ± 17.3 kW/m^2.

In general, average values of heat flux to the top and bottom plate of the DFT at the centre of the pan are relatively constant across all wind speeds, with the possible exception of the heat flux measured on the bottom plate at a wind speed of 4.7 m/s. The similarity in values of heat flux to the top plate of the DFT are due to upwind flame attachment, (Figure 4.19), which creates a similar environment in vicinity of the gauge surfaces under all wind conditions, as seen in the previous section without the blocking object present. The heat flux on the bottom plate decreases as the wind speed increases from 4.7 m/s, due to the flame tilt resulting in the bottom plate of the DFT being exposed to less of the fire plume. The difference in heat flux on the bottom plate of the DFT is not that large due to the overall similar environment in the fuel pan at different wind conditions, as seen in the other heat flux gauges.

Results of measured heat flux from both sides of the DFT gauge placed 0.5 m downwind of the centre of the pan for fire tests with a Blocking Object present are plotted in Figure 4.32 against the wind speed employed for each test. The highest average heat fluxes measured by each side of the DFT occur at the lowest speed, 4.7 m/s, with an average value of 127.5 kW/m^2 on the top plate (standard deviation 4.5 kW/m^2). Much lower heat fluxes are recorded on the top plate for all other wind speeds, averaging 107.8 kW/m^2, 106.2 kW/m^2, and 110.1 kW/m^2 at wind speeds of 7.3 m/s, 10.5 m/s and 13.5 m/s respectively, with higher standard deviations of 6.8 kW/m^2, 8.9 kW/m^2, and 8.2 kW/m^2 at wind speeds of 7.3 m/s, 10.5 m/s and 13.5 m/s respectively. The larger standard deviations are brought about by two tests which indicated much higher heat flux to the top plate of the DFT than other tests at the same wind speed, Test 20 (10.5 m/s) at 121.5 kW/m^2 and Test 25 (13.5 m/s) at 127.3 kW/m^2. The total uncertainty on the top plate of the DFT is ± 34.4 kW/m^2, while the bottom plate of the DFT is more accurate with an uncertainty of ± 12.8 kW/m^2.

Examination of measured heat flux to the bottom plate of the DFT [Figure 4.32] indicates that it is very similar to the heat flux measured at the pan center. The average heat flux at 4.7 m/s is again highest, averaging 47.2 kW/m^2, while the other values are much lower, 28.7 kW/m^2, 26.0 kW/m^2, and 28.9 kW/m^2 at wind speeds of 7.3 m/s, 10.5 m/s and 13.5 m/s respectively. The standard deviation across tests at similar wind speeds is again not very large, with a maximum of 3.1 kW/m^2 at 13.5 m/s. Elevated heat flux values were not measured for either of the tests (Test 20,25) for which elevated values of heat flux were recorded on the top plate of the DFT.

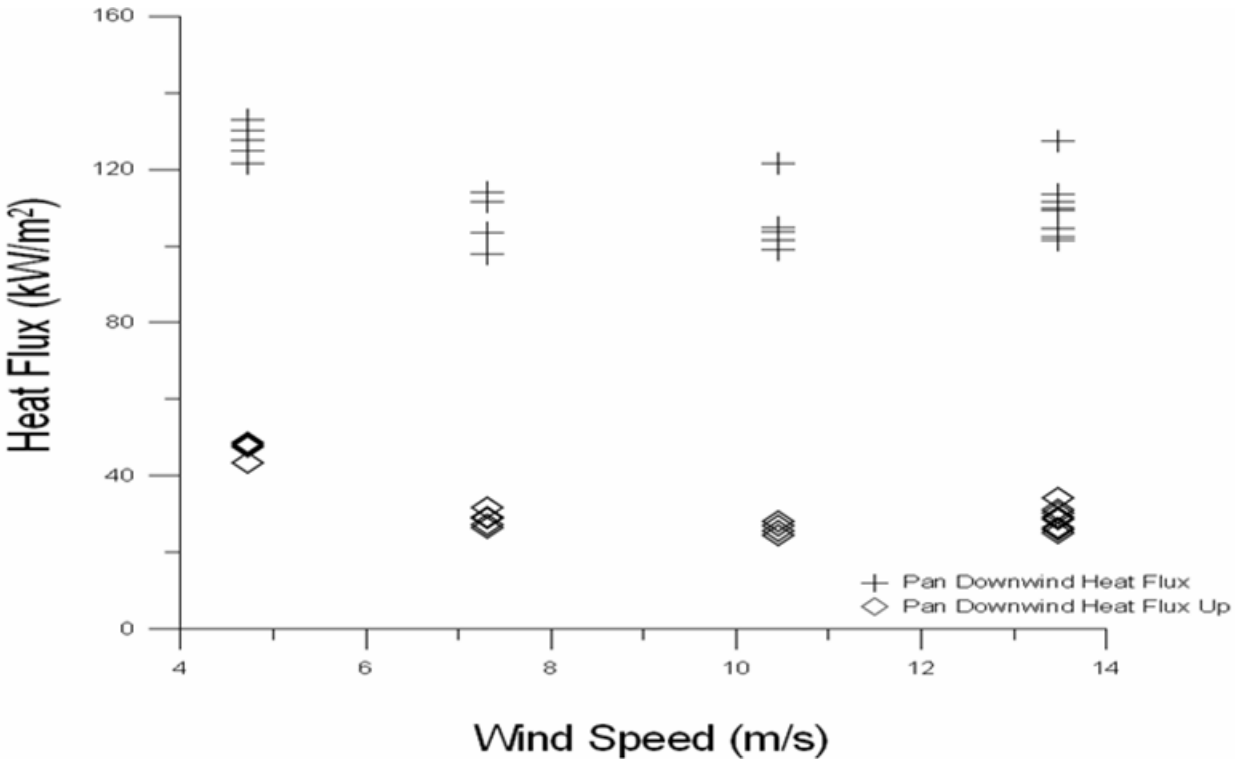

Figure 4.32 DFT 0.5 m downwind of Pan Center Heat Flux Measurements Versus Wind Speed in the Test Series with a Blocking Object Present

Except for the results taken at the lowest wind speed, values of heat flux determined for the top or bottom plate vary by a maximum of 6 % across the range of wind speeds tested. At 4.7 m/s, the heat flux recorded 0.5 m downwind of the pan center is higher than the heat flux recorded at the pan centre. This increase in heat flux is due to flame impingement on the Blocking Object that occurs at the lowest wind speed, with subsequent heating of the object and radiation back towards the fuel pan. In wind speeds of 7.3 m/s and higher, average values of heat flux measured on both the top and bottom plates of the downwind DFT are within 10 % of values obtained from the DFT located at the pan center, as well as to each other. This supports the notion that upwind flame attachment causes relatively homogeneous conditions near the fuel pan. Since the flames do not impinge on the object at wind speeds of 7.3 m/s and higher, measured heat flux values are relatively unaffected by the heating of the Blocking Object with subsequent re-radiation to the fuel surface that occurred under low wind conditions.

Results of measured heat flux from three different HFG situated in the fuel pan at positions 0.5 m upwind and downwind of the center of the fuel pan on the centre-line, as well as offset to the +y side for fire tests with a Blocking Object present are plotted in Figure 4.33 against the wind speed employed for each test. When the results are averaged for all tests across all wind speeds, the downwind HFG on the +y side records the highest average heat flux, at 114.5 kW/m^2, followed by the downwind centre-line HFG measuring an average of 107.7 kW/m^2 and finally the upwind centre-line HFG measuring 91.8 kW/m^2. As can be seen in the figure, the downwind HFG records relatively similar values across all wind speeds, averaging 110.9 kW/m^2, 105.3 kW/m^2, 106.2 kW/m^2, and 108.2 kW/m^2 at wind speeds of 4.7 m/s, 7.3 m/s, 10.5 m/s and 13.5 m/s respectively. Standard deviations for the first three wind speeds, varying between 7.3 and 8.2 kW/m^2, similar to the minimum deviation of 4.8 kW/m^2 for the 13.5 m/s winds. The

constant heat flux recorded at different wind speeds by the downwind HFG is in contrast to results from the other two HFGs, for which data show an increase in average heat flux as wind speed increases. The upwind HFG shows the most marked increase in heat flux with wind speed, averaging 51.3 kW/m^2, 86.5 kW/m^2, 103.8 kW/m^2, and 112.8 kW/m^2 for wind speeds of 4.7 m/s, 7.3 m/s, 10.5 m/s and 13.5 m/s respectively. This gauge also has the largest standard deviations in heat flux, with a maximum of 15.6 kW/m^2 at 4.7 m/s, and decreasing with increasing wind speed to a minimum of 6.0 kW/m^2. The downwind HFG on the +y side shows a similar, though not quite as marked trend, with average heat flux values of 80.7 kW/m^2, 113.0 kW/m^2, 126.9 kW/m^2, and 128.7 kW/m^2 at wind speeds of 4.7 m/s, 7.3 m/s, 10.5 m/s and 13.5 m/s respectively. The standard deviation, 13.7 kW/m^2, for this gauge is also highest at the lowest wind speed. Unlike the other two gauges, the lowest standard deviation for this gauge, 3.5 kW/m^2, occurs at a wind speed of 10.5 m/s. The maximum uncertainty for all three HFGs is ± 39.9 kW/m^2.

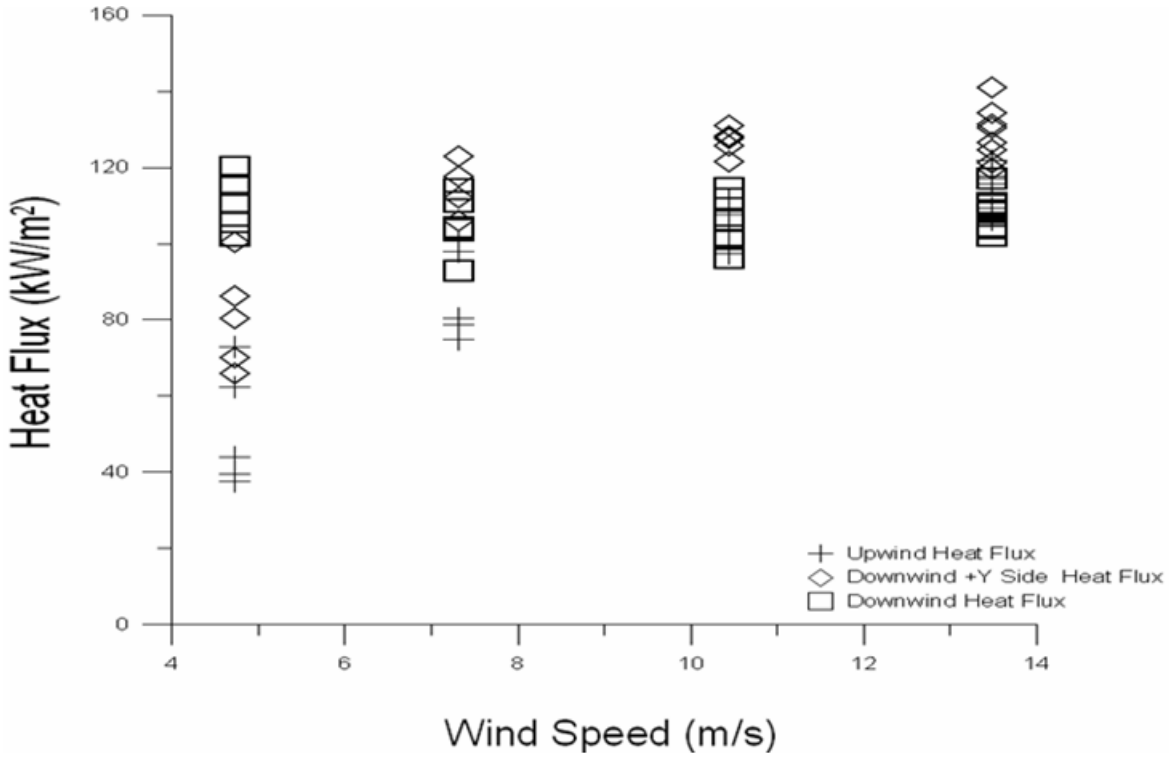

Figure 4.33 HFG Heat Flux Measurements Versus Wind Speed in the Test Series with a Blocking Object Present

The largest difference between the heat fluxes measured by the three HFGs occurs at the lowest wind speed, 4.7 m/s, when the downwind HFG records higher heat flux than either of the other two gauges. Since the downwind gauge is situated closest to the Blocking Object, these higher values are likely due to heating of the Blocking Object and subsequent re-radiation back to the surface of the gauge. As wind speed increases, measured values of heat flux suggest development of a more homogeneous fire environment. In support of this description, the HFG on the downwind +y side records increasing values of heat flux with increasing wind speed until it records approximately constant, albeit the highest, heat flux of the three gauges at 10.5 and 13.5 m/s. Based on examination of Figure 4.33, heat flux values measured using the DFT also point towards the homogeneity of the fire for the higher wind speeds. The upwind HFG initially records the lowest heat flux at the lower wind speeds, but recorded values of heat flux increase to equal those recorded by the other two gauges for the highest wind speeds. This suggests that fire conditions are very similar upwind and downwind of the pan centre at the higher speeds, consistent with the argument made in previous sections that upwind flame attachment results in relatively homogeneous conditions across the region immediately above the fuel surface.

Temperature measurements on the surface of the blocking object lend insight into the cause of the slightly elevated heat flux recorded by the HFG on the downwind +y side of the pan burner. It was seen that even though the fire plume visibly travels away from this gauge as it offsets toward the –y side [9], the thermocouples on the +y side of the surface of the blocking object at distances of 1 m from the centre of the test enclosure record elevated temperatures during fire tests. These temperatures are similar or even slightly higher than thermocouple measurements on the surface of the blocking object at a distance of -1.15 m from the centre of the test enclosure. This effect is exacerbated as the wind speed increases, most notably in Test 28

at 7.3 m/s and Test 29 at 10.5 m/s, where the thermocouples 1 m to the +y side actually record hotter temperatures than the thermocouples in the fire plume 1.15 m to the –y side [9]. This increased heating of the blocking object surface results in increased radiation feedback to the heat flux gauge on the +y side, which is seen in the increased heat flux measured by this gauge in Figure 4.33. The upwind heat flux gauge is not greatly affected by this radiation feedback from the Blocking Object, as upwind flame attachment to the fuel pan due to no false floor present causes the increase in measured value at this heat flux gauge.

Since there was a DFT and an HFG directly side-by-side during these tests with the blocking object present situated at 0.5 m downwind of the pan center, it will be useful to compare the results of the two different gauges. These are summarized in the plot of heat flux versus wind speed given in Figure 4.34. It can be seen in the figure that at the lowest wind speed, the DFT consistently recorded slightly higher heat flux levels than the HFG, but the values approached one another for wind speeds higher than 4.7 m/s. For example, the average heat flux value measured using the DFT was 127.5 kW/m^2 at the slowest wind speed. The corresponding value of heat flux measured using the HFG was 110.9 kW/m^2, or 13.1 % lower, at this wind speed. At the higher wind speeds of 7.3m/s, 10.5 m/s and 13.5 m/s, the DFT records average heat flux values of 107.8 kW/m^2, 106.2 kW/m^2 and 110.1 kW/m^2 while average heat flux measured by the HFG are 105.3 kW/m^2,106.2 kW/m^2 and 108.2 kW/m^2, 3.3 %, identical and 1.7 % lower respectively. Overall, these two gauges indicate excellent consistency in results suggesting very similar heat flux values particularly at higher wind speeds.

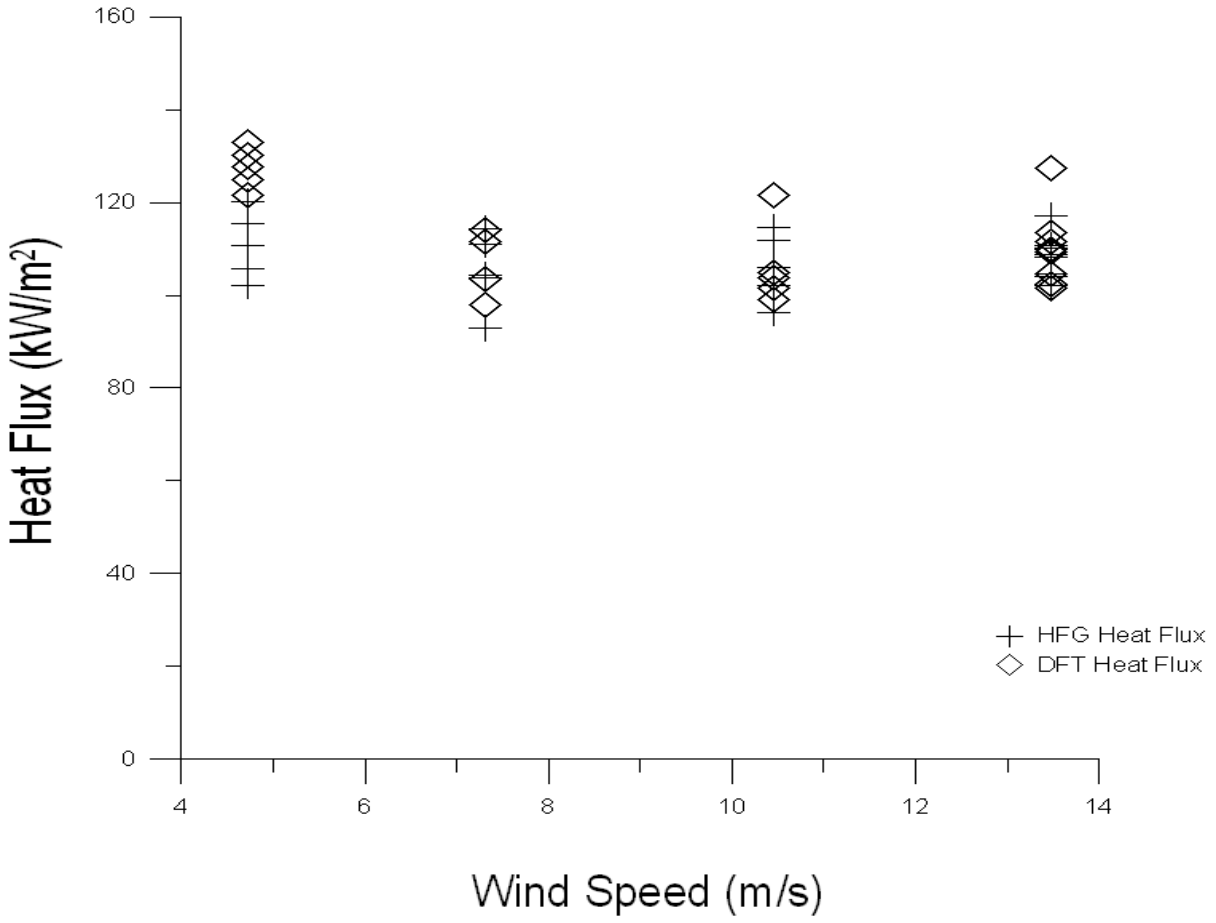

Figure 4.34: Comparison of side by side DFT and HFG Results from 0.5m downwind of the Pan Centre during the Test Series with a Blocking Object Present

The reason for the discrepancy between results from the DFT and the HFG is most likely due to conductive losses within the HFG, as was the case during the no Blocking Object tests. The difference is most prevalent at 4.7 m/s since any gauge heat losses due to conduction will be largest for the highest values of measured heat flux when the gauges are enveloped in flame. Both heat flux gauges have approximately equal maximum uncertainty, at ± 34.4 kW/m^2.

4.5.6 The Effect of the Blocking Object

In previous research, it was reported how much the shape of the fire plume changed as a function of wind speed, as well as due to the presence of the Blocking Object. These changes in fire shape and interactions with the Blocking Object will also affect the present measurements of heat flux.

At the slowest wind speed, 4.7 m/s, the main fire plume appears to oscillate around the Blocking Object as seen in Figure 4.35, sometimes attaching to it, sometimes passing underneath and occasionally some of the plume passes over the object instead of passing under it. In all these situations, the hot gases from the fire plume remain in very close proximity to the Blocking Object, resulting in significant heating of the front surface and underside of the object itself. Of particular interest is the heating of the front of the object since that would be expected to directly impact heat transfer to the fire plume. Indeed, evidence of such increased heating and resulting radiation transfer within the fire is evidenced by the higher values of heat flux to the surface of the fuel measured by both DFTs and the downwind HFG at the low wind speeds (Section 4.5.5). The effect is most noticeable in results recorded by the downwind DFT, which is closest to the Blocking Object. The accompanying HFG next to it records less heat flux than the DFT due to internal conduction losses as mentioned previously, but still records the highest heat flux of any wind speed at 4.7 m/s.

Figure 4.35: Fire Plume Attachment to the Blocking Object during a Live Fire Test at 4.7 m/s wind speed

With a wind speed of 7.3 m/s, the fire plume may still attach to the Blocking Object from time to time, but not nearly to the same degree as at the wind speed of 4.7 m/s. During the majority of the live fire tests, the fire plume passes cleanly under the Blocking Object and continues to oscillate [Figure 4.36].

Figure 4.36: Fire Plume Attachment to the Blocking Object during a Live Fire Test at 7.3 m/s wind speed

The DFT at the pan centre and all three downwind heat flux gauges, two HFGs and one DFT, record very similar values of average heat flux at this wind speed, with values slightly lower than those measured for a wind speed of 4.7 m/s. Only the downwind HFG on the +y side records a higher heat flux at this wind speed than at 4.7 m/s, but this has previously been discovered to be caused by heating of the blocking object away from the fire plume on the +y side. Values of heat flux recorded by the upwind HFG gauges are lower than those at the downwind gauges, but are higher overall compared to the results from 4.7 m/s. Since there is less flame impingement on the Blocking Object as seen by the temperatures on the surface of the Blocking Object [9], heating of the object does not affect heat fluxes to the same extent as it did

for fires in a crosswind of 4.7 m/s. However, flame tilt with the increased wind speed results in increased heat flux from the fire plume to the downwind gauges, as the plume is located closer to the gauges, and farther away from the upwind gauge. The upwind gauge still measures elevated heat flux compared to slower speed tests due to the upwind flame attachment to the fuel pan seen previously during fire tests with no false floor in place, but the bulk of the fire plume is traveling away from this gauge.

As the wind speed increases again to 10.0 m/s and 13.5 m/s, the fire plume is flattened out to the point that it does not impinge on the Blocking Object but rather passes cleanly underneath it during each test. Most of the heat flux gauges record readings similar to those measured for the lower wind speed, with the exception of the upwind HFG and downwind HFG on the +y side, which both record increased levels of heat flux. The upwind HFG is affected by the upwind flame attachment to the fuel pan, resulting in more heat flux in that location compared to the relative homogeneity of the environment above the fuel pan. As previously discussed, the downwind HFG on the +y side is receiving increased feedback from the Blocking Object, as increased heating on the +y side of the Blocking Object occurs at these wind speeds. It is not known exactly why this occurs, but there is speculation that it is due to the flame oscillating laterally during fire tests as well. The majority of the time the flame passes to the –y side, which results in the highest temperatures being recorded on that side of the Blocking Object, but the elevated temperatures on the +y side of the Blocking Object suggest that the oscillation could be a real phenomenon.

The Blocking Object definitely has an effect on heat flux measurements made inside the fuel pan at all wind speeds. This results in higher overall heat flux values recorded by all gauges when compared to heat flux measurements made when the Blocking Object was not present. At

the lowest wind speed, the Blocking Object has the most effect on downwind heat flux due to flame impingement and re-radiation from the surface of the Blocking Object. At higher velocities, while this effect is still present, the influence of the Blocking Object on the local flow conditions becomes more important in the determination of heat flux distribution.

4.5.7 Comparison of Heat Flux and Fuel Regression Rate

In the previous sections, measured values of heat flux and fuel regression rates were independently plotted versus wind speed to assess any trends and relationships that could be drawn from the data. Using the load cell data for fuel regression rate with data from the HFGs and DFTs, relationships between heat flux and fuel regression rates are explored in this section. Figure 4.37 contains a plot of heat flux, as measured by both upwind and downwind HFG gauges, versus fuel regression rate. The spread of fuel regression rate results is expected, despite a similar test setup for every experiment, as this is encountered frequently in large scale pool fire research [64]. While for most of the gauges heat flux appears relatively constant despite increasing fuel regression rate, there does appear to be a weak relationship of increasing fuel regression rate with increasing heat flux for the downwind HFG on the +y side. There are many outliers in the data, however, especially for lower values of fuel regression rate so such a relation may be masked by the effects of other complex phenomena that interact to determine the overall behaviour of the fire. The maximum uncertainty in this graph is ± 39.9 kW/m^2.

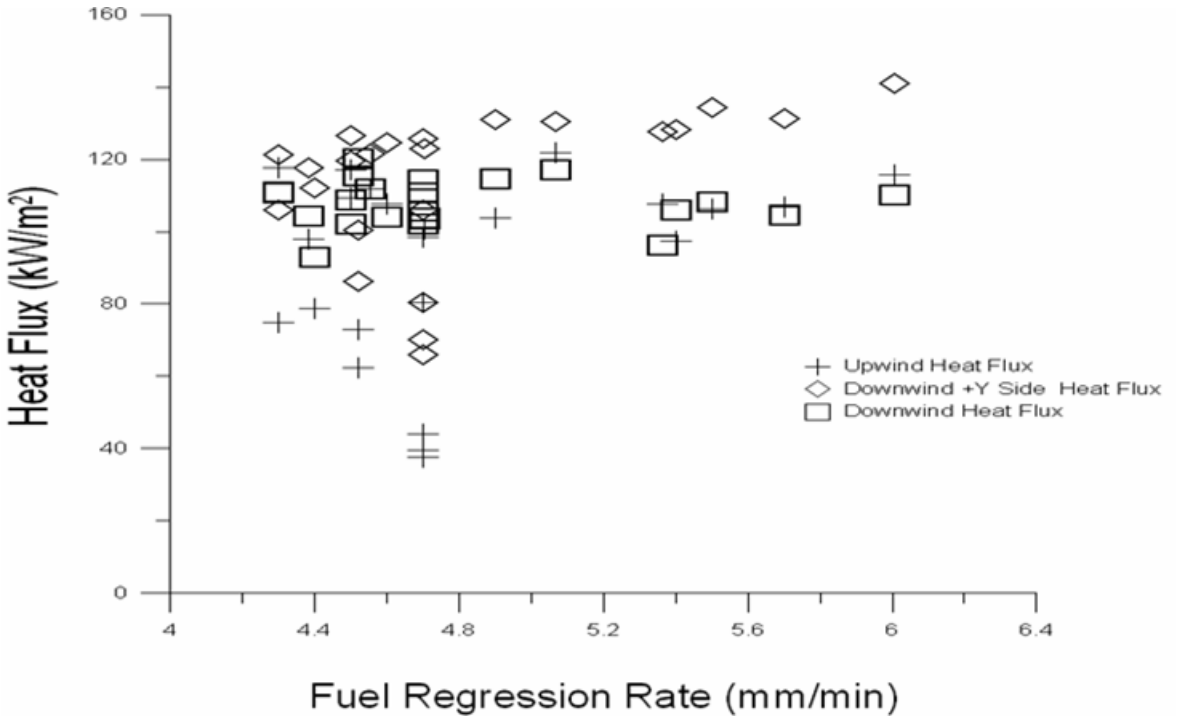

Figure 4.37 HFG Heat Flux Results during the Test Series with a Blocking Object present compared to the Fuel Regression Rate

Figure 4.38 contains a plot of heat flux, as measured by the pan centre and downwind DFT gauges, versus fuel regression rate. There are no obvious trends evident in the data, which suggest relatively constant heat flux across the range of fuel regression rate found in this work. This has been noted previously [64] and is consistent with the overall scatter and lack of clear trends seen in plots of measured fuel regression rate and heat flux versus wind speed. The maximum uncertainty for the top plate of the DFT is ± 34.4 kW/m^2, while the bottom plate of the DFT has an uncertainty of ± 14.9 kW/m^2.

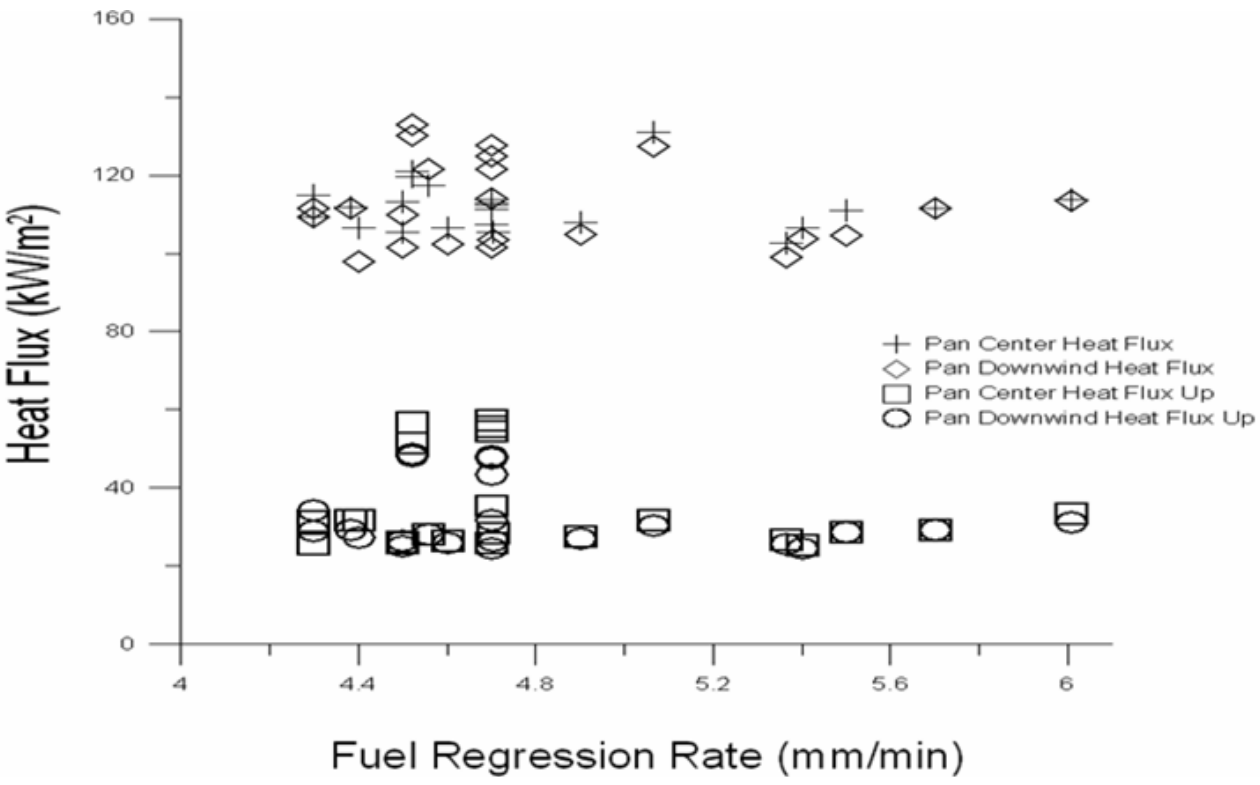

Figure 4.38 DFT Heat Flux Results during the Test Series with a Blocking Object present compared to the Fuel Regression Rate

Overall, when examining the measured heat flux, wind speed and fuel regression rate of the three different configurations, only fire tests with no Blocking Object present but with a false floor present showed a trend between the three measurements, as an increase in any one of the measurements resulted in an increase in the other two measurements as well. However, not enough testing was performed with this configuration in order to demonstrate these trends with any repeatability. During the test series with no Blocking Object or false floor present, and the test series with a Blocking Object present, the majority of measured heat fluxes remained relatively constant regardless of wind speed, and the fuel regression rates showed no trends with either the wind speed or the measured heat flux.

Chapter 5

Conclusions and Future Work

5.1 Conclusions

This thesis explores the relationship between the fuel regression rate of a 2.0 m diameter pool fire and the crosswind speed, the local heat flux and the ambient conditions as determined in experiments conducted at the UWLFRF. Three different configurations were used: no blocking object and no false floor present, no blocking object and a false floor present, and a blocking object present. The blocking object in question is a 2.7 m diameter culvert which is intended to represent an aircraft fuselage, as this series of experiments initially was based on transportation accidents. The wind speed was varied between 3.0 m/s and 13.5 m/s and background crosswind turbulence measurements were taken when possible. The fuel regression rate was measured using two different methods; with load cells, and with a sight glass. The wind speed was measured downwind of the fuel pan using bidirectional probes and the heat flux in the fuel pan was measured with two different heat flux gauges, known as the HFG and the DFT respectively. Ambient conditions were determined with data from two separate weather stations. An uncertainty analysis was presented for all instrumentation where it was feasible, and estimates of uncertainty are presented for all instruments. A wind characterization of all three configurations involving the blocking object and the false floor was also performed in order to better understand the local flow conditions near the fuel pan during a fire test, which also has an influence on the fuel regression rate. When the experiments were finished and the results were analyzed, the following conclusions were evident:

1. During characterization of the flow within the UWLFRF, it was found that the bulk of the flow acted like a pair of rectangular jets whether or not the blocking object was in place, whereas it was previously postulated that the flow resembled that of a bluff wall jet. It was also discovered that the baffle plates on each of the six fans divert the flow from a given fan laterally, where flow from one fan merges with the flow of the adjacent fan to form an area of elevated velocity that can be seen as the flow leaves the plenum into the test enclosure. As these areas of elevated velocity travel downwind, they merge with the surrounding flow in the manner expected by a pair of rectangular jets. A "saddle-shape" velocity profile, indicative of a rectangular jet in the transitional region, is present, but it is caused by jets merging due to physical blockage within the flow as the rectangular jet has not had enough time to develop into the transitional region. When the blocking object was in place, velocity measurements taken directly upwind and downwind of the blocking object are greatly influenced by the presence of the blocking object. Upwind of the object, they are very similar to the velocity results when the blocking object is not in place. However, downwind of the blocking object, the effect of the object is clear.
2. Turbulence measurements taken on the centre-line of the test enclosure when the blocking object is not in place show some areas of elevated turbulence intensity at heights of 4.2 m and higher. Below this height, as the flow travels through the test enclosure the maximum turbulence intensity is measured at 11.5 %, 9.6 %, 20 % and 8 % at distances of 1.25 m, 4.25 m, 10.25 m and 14.25 m from the plenum outlet, with the average turbulence intensity being even lower. Above this height, measurements located in shear layers between areas of elevated velocity and depressed velocity result in increased turbulence intensity with a maximum intensity of 50.7 % measured in one location.

3. The fuel regression rate for the test series with no blocking object present was determined using load cells, as the sight glass method failed during this test series. When the false floor was not in place the fuel regression rate was measured to be 4.4 mm/min, 3.5 mm/min, 3.8 mm/min and 4.4 mm/min at wind speeds of 3.0 m/s, 4.6 m/s, 7.1m/s and 10.0 m/s respectively. When the false floor was put into place the fuel regression rate was measured to be 3.8 mm/min, 4.2 mm/min, 4.3 mm/min and 5.2 mm/min at wind speeds of 3.0 m/s, 4.6 m/s, 7.1m/s and 10.0 m/s respectively. Without the false floor in place, there was no trend relating the wind speed and the fuel regression rate, but when the false floor was in place, an increase in wind speed resulted in an increase in the fuel regression rate.
4. The fuel regression rate for the test series with a blocking object was determined using both load cells and the sight glass. The load cell fuel regression rate measurements were higher, averaging 4.6 mm/min, 4.5 mm/min, 5.0 mm/min and 5.0 mm/min at wind speeds of 4.7 m/s, 7.3 m/s, 10.5 m/s and 13.5 m/s respectively. The sight glass measured average fuel regression rates were 3.9 mm/min, 3.7 mm/min, 4.1 mm/min and 4.4 mm/min at wind speeds of 4.7 m/s, 7.3 m/s, 10.5 m/s and 13.5 m/s respectively. Both methods showed considerable variation in the measured fuel regression rate from test to test. However, it can be seen that the highest fuel regression rates occur in the higher wind speed tests. Ambient temperature and wind speed did not appear to influence measured

5. When the heat flux around the fuel pan is examined during the fire tests with no blocking object present, it is measured to be relatively constant during tests with no false floor present except for during tests at 3.0 m/s wind speed, when the heat flux measured on the bottom plate of the DFT is higher than measurements made at other wind speeds, which is due to the increasing flame tilt as the wind speed increases. The top plate of the DFT records a maximum heat flux of 113.1 kW/m^2 and a minimum heat flux of 100.7 kW/m^2 across all wind speeds. The bottom plate of the DFT records a maximum of 66.2 kW/m^2 at the aforementioned slowest wind speed of 3.0 m/s, and then decreases to a minimum of 25.1 kW/m^2 at higher wind speeds, with the other measurements very similar to the minimum heat flux measured. When the heat fluxes are compared to the fuel regression rates from each test no trends are evident, due to the similarity between the heat flux during each test combined with the high variation in the measured fuel regression rates. When the false floor is put into place, some trends become visible: the heat flux measured on the top plate of the DFT and the HFG decreases with increasing wind speed, while the bottom plate of the DFT records increasing heat flux with increasing wind speed; the HFG records a maximum of 71.2 kW/m^2 at the slowest wind speed and the minimum 45.6 kW/m^2 at the fastest wind speed, and the top plate of the DFT records 67.7 kW/m^2 at the slowest wind speed, and the lowest heat flux, 45.9 kW/m^2, almost identical to that recorded by the HFG, at the highest wind speed. The bottom plate of the DFT records the lowest heat flux 62.0 kW/m^2 at the lowest speed of 3.0 m/s, while at the highest wind speed of 10.0 m/s the heat flux is measured to be 83.7 kW/m^2.

6. The heat flux results from the test series with a blocking object present are similar to the results from the test series with no blocking object and no false floor present, in that the heat flux is relatively constant for some of the gauges, especially those near the pan centre. Both DFTs record similar heat flux at all wind speeds, with the top of the pan centre DFT recording an average of 111.9 kW/m^2 with a maximum heat flux of 115.5 kW/m^2 at the slowest wind speed of 4.7 m/s and the top of the downwind DFT recording an average of 112.5 kW/m^2 with a maximum heat flux of 127.5 kW/m^2 at the slowest wind speed of 4.7 m/s, with the other heat fluxes being slightly lower than the average. The bottom plates of both of these DFTs record higher heat flux at the lowest wind speed and then near constant heat flux at all subsequent wind speeds, with the pan centre DFT recording an 55.1 kW/m^2 at 4.7 m/s, compared to an average of 34.6 kW/m^2 across all tests conducted at all wind speeds and the downwind DFT averages 47.2 kW/m^2 during tests at 4.7 m/s, with an overall average of 32.2 kW/m^2 across all tests.
7. Heat flux measured using the HFGs are very different depending on the gauge location in the fire. The downwind HFG records relatively constant heat flux with an average of 107.7 kW/m^2 across all wind speeds, and a maximum heat flux of 110.9 kW/m^2 at the lowest wind speed of 4.7 m/s. The downwind HFG on the +y side and the upwind HFG both record increasing heat flux with increasing wind speed. The upwind HFG averages 51.3 kW/m^2, 86.5 kW/m^2, 103.8 kW/m^2, and 112.8 kW/m^2 for wind speeds of 4.7 m/s, 7.3 m/s, 10.5 m/s and 13.5 m/s respectively, while the downwind HFG on the +y side records 80.7 kW/m^2, 113.0 kW/m^2, 126.9 kW/m^2, and 128.7 kW/m^2 at wind speeds of 4.7 m/s, 7.3 m/s, 10.5 m/s and 13.5 m/s respectively. When examining these results compared to the measured fuel regression rates, the downwind HFG on the +y side shows

5.2 Future Work

1. Fuel regression rate under quiescent conditions could not be measured in the present set of experiments. It is thought that performing a quiescent live fire test inside the UWLFRF would damage the facility as well as the measuring equipment, so another location where the local wind conditions can be controlled may be more suitable for this experiment. The lack of this value makes non-dimensional analysis of the present data difficult.
2. A false floor could be used in future tests with a blocking object as it appeared to stabilize the flow near the fuel pan. While it is not completely realistic to have a perfectly level surface upwind of a hydrocarbon fuel fire in a crosswind, it is equally unrealistic to have a large step directly upwind of the fire. Placing the false floor during fire tests with the blocking object present would result in no upwind attachment of the flames as the fire plume would stay cohesive and be swept downwind away from the fuel pan.
3. Differing amounts of fuel placed inside the pan has previously been suggested, but never implemented as a possible way to improve the investigation of the effect of lip height and fuel depth in the fuel pan on pool fire behaviour. It is thought that using a full drum of fuel during a test will damage the instrumentation during a live fire test, but ¼ and ¾ of a barrel of fuel could be used in order to vary the lip height and fuel depth enough to investigate effects on the fuel regression rate and overall pool fire behaviour.

4. More flow conditioning in the plenum would result in fewer areas of elevated and depressed velocity within the test enclosure. A more uniform flow issuing from the plenum could be accomplished through placing tubes in the grid at the plenum exit, provided they would not impede the flow enough to decrease the maximum velocity below the desired maximum velocity. Removing the baffle plates on each fan or straightening them so that they are aligned with the flow would also decrease formation of areas of elevated velocity, leading to better merging of the flows from the individual fans, and hence result in a more uniform flow overall.

References

1. Lois, E., Swithenbank, J., Fire hazards in oil tank arrays in a wind. In 17th Symposium (International) on Combustion, Pittsburgh, PA, 1979. The Combustion Institute.
2. Capener, E. L., Alger, R. S., Characterization and suppression of aircraft and fuel fires. In Western States Section Meeting of the Combustion Institute, Monterey, CA, 1972. Paper WSCI 72-26.
3. Planas-Cuchi, E., Casal, J., Lancia, A., Bordignon, L., Protection of equipment engulfed in a pool fire. Journal of Loss Prevention in the Process Industries, 9:231-240, 1996.
4. Gritzo, L. A., Nicolette, V. F., Murray, D., Moya, J. L., Skocypec, R. D., Wind-induced interaction of a large cylindrical calorimeter and an engulfing JP-8 pool fire. Technical Report SAND95-1635C, Sandia National Laboratories, Albuquerque, NM, 1995. In Symposium on Thermal Sciences and Engineering in Honor of Chancellor Chang-Lin Tien, San Francisco, CA, November 1995.
5. Keltner, N. R., Gill, W., Kent, L. A., Simulating fuel spill fires under the wing of an aircraft. In Fourth International Symposium on Fire Safety Science, International Association for Fire Safety Science, July 1994.
6. Fry, C. J., Pool Fire Testing at AEE Winfrith. In Proceedings of the 9th International Symposium on Packaging and Transportation of Radioactive Materials, Washington, D.C., June 1989.
7. Burgess, M. H., Fry, C.J., Fire Testing for Package Approval. RAMTRANS, 1(1):7-16, 1990.
8. Lam, C. S., Thermal characterization of a pool fire in crosswind with a large adjacent cylindrical object: Experimental design. Master's Thesis, University of Waterloo, Waterloo, ON, 2004.
9. Lam. C. S., Thermal Characterization of a Pool Fire in Crosswind With and Without a Large Downwind Blocking Object. PhD Thesis, University of Waterloo, Waterloo, ON, 2009.
10. Randsalu, E., Measurement of Fuel Regression Rate in a Jet-A Fuelled Fire in Crosswind. Master's Thesis, University of Waterloo, Waterloo, ON, 2005.
11. Weisinger, J., Characterization of the university of waterloo live fire research facility wind generation system. Master's Thesis, University of Waterloo, Waterloo, ON, 2004.
12. Rajaratham, N., Turbulent Jets. Elsevier Scientific Publishing Company, New York, 1976.
13. Abramovich, G.N., The Theory of Turbulent Jets. The M.I.T. Press, Cambridge, MA, 1963.

14. Rodi, W., Turbulent Buoyant Jets and Plumes. In The Science and Application of Heat and Mass Transfer: Reports, Reviews & Computer Programs, Vol 6, Pergamon Press, New York, 1982.
15. Krothapalli, A., Baganoff, D., and Karamcheti, K., On the mixing of a rectangular jet. *Journal of Fluid Mechanics*, 107:201-220, 1981.
16. Deo, R., Nathan, G., Mi, J., Comparison of turbulent jets issuing from rectangular nozzles with and without sidewalls. *Experimental Thermal and Fluid Science*, **32**(2):596-606, 2007
17. Trentacoste, N., Sforza, P.M., Further experimental results for three-dimensional free jets. *AIAA Journal*, 5:885-891, 1967.
18. Laufer, J., New trends in experimental turbulence research. *Annual Review of Fluid Mechanics*, 7:307-326, 1975.
19. Sforza, P. M., Herbst, G., A Study of Three-Dimensional, Incompressible, Turbulent Wall Jets. PIBAL Report No. 1022, Polytechnic Institute of Brooklyn, Department of Aerospace Engineering and Applied Mechanics, 1967.
20. Rajaratnam, N., Pani, B. S., Three-Dimensional Turbulent Wall Jets. *Journal of the Hydraulics Division*, 100:69-82. 1974.
21. Miller, D. R., Comings, E. W., Force-Momentum Fields in a Dual Jet Flow. *Journal of Fluid Mechanics*, 7:237-256, 1960.
22. Militzer, J., Dual Plane Parallel Turbulent Jets: The Measurement and Prediction of the Mean Velocity Field. PhD Thesis, University of Waterloo, Waterloo, Ontario, January, 1977.
23. Lin, Y. F., Sheu, M.J., Interaction of Parallel Turbulent Plane Jets. AIAA Journal, **29**(9), 1372-1373, 1991.
24. Anderson, E. A., Spall, R.E., Experimental and Numerical Investigation of Two-Dimensional Parallel Jets. Journal of Fluids Engineering, 123:401-406, 2001.
25. Nasr, A., Lai, C. S., Comparison of Flow Characteristics in the Near Field of Two Parallel Plane Jets and an Offset Plane Jet. *Physics of Fluids*, **9**(10), 2919-2931, 1997.
26. Munson, B. R., Young, D. F., Okiishi, T. H., Fundamentals of Fluid Mechanics, 4th Edition. John Wiley & Sons, Inc., New York, 2002.
27. Nakakuki, A. Heat transfer in small scale pool fires. *Combustion and Flame*, 96:311-324, 1994.
28. Hamins, A., Fischer, S. J., Kashiwagi, T., Klassen, M.E., Gore, J. P., Heat feedback to the fuel surface in pool fires. *Combustion Science and Technology*, 97:37-62, 1994.
29. Burgess, D.S., Strasser, A., Grumer, J., Diffusive burning of liquid fuels in open trays. *Fire Research Abstracts and Reviews*, 3:177-192, 1961.
30. Rasbash, D. J., Rogowski, Z. W., Stark, G. W. V., Properties of fires of liquids. *Fuel*, 35:94-107, 1956.
31. Emmons, H.W., Some observations of pool burning. In *International Symposium on the Use of Models in Fire Research*, Washington, DC, 1961. National Academy of Sciences. NAS/NRC Publication 786.

32. Hogben, C.D.A., Determination of the radiative properties of an acetone pool fire. Master's Thesis, University of Waterloo, Waterloo, Ontario, 1998.
33. Akita, K., Yumoto, T., Heat transfer in small pools and rates of burning of liquid methanol. In *10th Symposium (International) on Combustion*, Pittsburgh, Pa, 1965.
34. Corlett, R. C., Fu, T. M., Some recent experiments with pool fires. *Pyrodynamics*, 4:253-269, 1966.
35. Weckman, E. J., The Structure of the Flow field Near the Base of a Medium-Scale Pool Fire. PhD Thesis, University of Waterloo, Waterloo, Ontario, 1987.
36. Crauford, N.L., The Structure of an Unconfined Buoyant Turbulent Diffusion Flame. PhD Thesis, Dept. Of Aeronautics and Astronautics, University of Southampton, England, 1984.
37. Hall, A. R., Pool burning. *Oxidation and Combustion Reviews*, 6:169-225, 1973.
38. Gritzo, L. A., Gill, W., Nicolette, V.F., Estimates of the extent and character of the oxygen-starved interior in large pool fires. In Keltner, N.R., Alvares, N. J., Grayson, S. J., editors, *Very Large-Scale Fires*, 84-98, American Society for Testing and Material, 1998. ASTM Special Technical Publication 1336.
39. Wood, B. D., Blackshear, Jr., P. L., Eckert, E.R.G., Mass fire model: An experimental study of the heat transfer to liquid fuel burning from a sand-filled pan burner. *Combustion Science and Technology*, 4:113-129, 1971.
40. Shinotake, A., Koda, S., Akita, K., An experimental study of radiative properties of pool fires of an intermediate scale. *Combustion Science and Technology*, 43:85-97, 1985.
41. Adiga, K. C., Ramaker, D. E., Tatem P. A., Williams, F.W., Modeling thermal radiation in open liquid pool fires. In *Second International Symposium on Fire Safety Science*, International Association for Fire Safety Science, June 1988.
42. Brosmer, M. A., Tien, C. L., Radiative energy blockage in large pool fires. *Combustion Science and Technology*, 51:21-37, 1987.
43. Kelley, C. S., The transfer of radiation from a flame to its fuel. *Journal of Fire and Flammability*, 4:56-66, 1973.
44. Blinov, V. I., Khudyakov, G. N., Diffusion burning of liquids. Technical report, Izdatel'stvo Akademii Nauk SSSR, Moscow, 1961. T-1490a-c, English Translation: U.S. Army Engineer Research and Development Laboratories, Information Resources Branch, Translation Analysis Section, Fort Belvoir, VA.
45. Blinov, V. I., Khudyakov, G. N., On certain regularities of diffusion burning of liquids. *Doklady Akademii Nauk SSSR*, 113:1094-1098, 1957. English Translation: Doklady Physical Chemistry, 113:241-244, 1957.
46. Hottel, H. C., Review: Certain laws governing diffusive burning of liquids. *Fire Research Abstracts and Reviews*, 1:41-44, 1959.
47. Magnus, G., Tests on combustion velocity of liquid fuels and temperature distribution in flames and beneath surface of the burning liquid. In *International Symposium on*

48. Koseki, H., Iwata, Y., Natsume, Y., Takahashi, T., Hirano, T., Tomakomai large scale crude oil fire experiments. *Fire Technology*, 36:24-38, 2000.
49. Chatris, J. M., Quintela, J., Folch, J., Planas, E., Arnaldos, J., Casal, J., Experimental study of burning rate in hydrocarbon pool fires. *Combustion and Flame*, 126:1373-1383, 2001.
50. Yumoto, T., Heat transfer from flame to fuel surface in large pool fires. *Combustion and Flame*, 17:108-110, 1971.
51. Alger, R. S., Corlett, R. C., Gordon, A.S., Williams, F. A., Some aspects of structures of turbulent pool fires. *Fire Technology*, 15:142-156, 1979.
52. Babrauskas, V., Estimating large pool fire burning rates. *Fire Technology*, 19:251-261, 1983.
53. Hamins, A., Fischer, S. J., Kashiwagi, T., Klassen, M.E., Gore, J. P., Heat feedback to the fuel surface in pool fires. *Combustion Science and Technology*, 97:37-62, 1994.
54. Masliyah, J. H., Stewart, F. R., Radiative heat transfer from a turbulent diffusion buoyant flame with mixing controlled combustion. *Combustion and Flame*, 13:613-625, 1969.
55. Burgess, D., Hertzberg, M., Radiation from pool flame. In Afgan, N. H., Beer, J. M., editors, *Heat Transfer in Flames*, 413-430, Scripta Book Company, 1974.
56. Burgess, D., Grumer, J., Wolfhard, H. G., Burning rates of liquid fuels in large and small open trays. In *International Symposium on the Use of Models in Fire Research*, Washington, DC, 1961. National Academy of Sciences. NAS/NRC Publication 786.
57. Burgess, D., Zabetakis, M., Fire and explosion hazards associated with liquefied natural gas. Report of Investigations 6099, U.S. Department of the Interior, Bureau of Mines, Washington, 1962.
58. Zhou, X. C., Gore, J. P., Effects of a floor on the entrainment flow field induced by a pool fire. In Smith S. B., editor, *Annual Conference of Fire Research: Book of Abstracts October 17-20, 1994*, 81-82, Gaithersburg, MD, Building and Fire Research Laboratory, National Institute of Standards and Technology. NISTIR 5499.
59. Orloff, L., Simplified radiation modeling of pool fires. In *18th Symposium (International) on Combustion*, Pittsburgh, PA, 1981. The Combustion Institute.
60. Drysdale, D., An Introduction to Fire Dynamics. John Wiley and Sons, 2nd edition, New York, 1998.
61. Mudan, K. S., Thermal radiation hazards from hydrocarbon pool fires. *Progress in Energy and Combustion Science*, 10:59-80, 1984.
62. Pitts, W.M., Wind effects on fires. *Progress in Energy and Combustion Science*, 17:83-134, 1991.

63. Gritzo, L. A., Nicolette, V. F., Tieszen, S.R., Moya, J.L., Holen, J., Heat transfer to the fuel surface in large pool fires. In Chan S. H., editor, *Transport Phenomena in Combustion (Volume 1)*, 701-712, Washington, DC, 1996. Taylor and Francis.
64. Lam, C. S., Randsalu, E., Weckman, E. J., Brown, A., Gill, W., Gritzo, L. A., Fuel Regression Rates in Large Hydrocarbon Pool Fires in Crosswinds. In Interflam 2004 10th International Fire Science and Engineering Conference, Edinburgh, July 2004.
65. Lois, E., Swithenbank, J., Fire hazards in oil tank arrays in a wind. In *17th Symposium (International) on Combustion*, Pittsburgh, PA, 1979. The Combustion Institute.
66. Welker, J. R., Sliepcevich, C. M., Burning rates and heat transfer from wind-blown flames. *Fire Technology*, 2:211-218, 1966.
67. Apte, V. B., Green, A. R., Kent, J. H., Pool fire plume flow in a large-scale wind tunnel. In *Third International Symposium on Fire Safety Science*, International Association for Fire Safety Science, July, 1991.
68. Neill, D. T., Welker, J. R., Sliepcevich, C. M., Direct contact heat transfer from buoyant diffusion flames. *Journal of Fire and Flammability*, 1:289-301, 1970.
69. Russell, L. H., Canfield, J. A., Experimental measurement of heat transfer to a cylinder immersed in a large aviation-fuel fire. *Journal of Heat Transfer*, 95:397-404, 1973.
70. Kramer, M. A., Greiner, M., Koski, J. A., Lopez, C., Suo-Anttila, A., Measurements of heat transfer to a massive cylindrical calorimeter engulfed in a circular pool fire. *Journal of Heat Transfe*r, 125:110-117, 2003.
71. Bainbridge, B. L., Keltner, N. R., Heat transfer to large objects in large pool fires. *Journal of Hazardous Materials*, 20:21-40, 1988.
72. Gregory, J. J., Keltner, N. R., Mata, Jr., R. Thermal measurements in large pool fires. *Journal of Heat Transfer*, 111:446-454, 1989.
73. Kramer, M. A., Greiner, M., Koski, J. A., Radiation heat transfer to the leeward side of a massive object suspended over a pool fire. In *Proceedings of the ASME Heat Transfer Division*, American Society of Mechanical Engineers, 2001. Paper IMECE2001/HTD- 24250.
74. Suo-Anttila, J. M., Gritzo, L. A., Thermal measurements from a series of tests with a large cylindrical calorimeter on the leeward edge of a JP-8 pool fire in cross-flow. Technical Report SAND 2001-1986, Sandia National Laboratories, Albuquerque, NM, 2001.
75. Videocube, October 2000. http://research.microsoft.com/en-us/downloads/ec37a62b-ce59-4aac-b0af-f465c63b026c/default.aspx. Last accessed Feb, 2009.
76. Gibbons, M., Analysis of Irregular Thermocouple Data in Large-Scale Fire Testing. Work Report, University of Waterloo, Waterloo, ON, 2005.
77. Lomas, C. G., Fundamentals of Hot Wire Anemometry. Cambridge University Press, Cambridge, U.K., 1986.
78. O'Hern, T. J., Schefer, R. W., Gerhart, A. L., Young, C., Weckman, E.J., Simultaneous Measurement of Velocity and Concentration Fields Using a High-

Speed Motion Picture PIV/PLIF System in a Buoyant Helium Plume. In ASME International Mechanical Engineering Congress and Exposition, New York, November 2001.
79. Campbell Scientific Inc., CSAT3 Three-Dimensional Sonic Anemometer, Logan, UT, Revised November 2007.
80. Berard, R. Personal Communication. Campbell Scientific Canada, Edmonton, AB, June 2006.
81. Labine, C. Personal Communication. Campbell Scientific Canada, Edmonton, AB, August 2006.
82. Blanchat, T. K., Humphries, L. L., and Gill, W., Sandia heat flux gauge thermal response and uncertainty models. Technical Report SAND2000-1111, Sandia National Laboratories, Albuquerque, NM, 2000.
83. Lam, C. S., Weckman, E. J., Steady-state heat flux measurements in radiative and mixed radiative–convective environments. *Fire and Materials*, published online Feb 2009.
84. Keltner, N., Directional Flame Thermometers – A Tool for Measuring Thermal Exposure in Furnaces and Improving Control. In 11th Interflam Conference, London, U.K., 2007.
85. Beck, J., User's Manual for IHCP1D, a Program for Calculating Surface Heat Fluxes from Transient Temperatures Inside Solids. Beck Engineering Consultants Co., Okemos, MI, 1999.
86. Souil, J.M., Vantelon, J.P., Joulain, P., Grosshandler, W. L., Experimental and theoretical study of thermal radiation from freely burning kerosene pool fires. Progress in Astronautics and Aeronautics, 105 Part 1:388-401, 1986.
87. Schneider, M. E., Kent, L. A., Measurements of gas velocities and temperatures in a large open pool fire. *Fire Technology*, 25:51-80, 1989.
88. Koseki, H., Yumoto, T., Air entrainment and thermal radiation from heptanes pool fires. *Fire Technology*, 24:33-47. 1988.
89. Davis Instruments., Integrated Sensor Suite Installation Manual, Hayward, CA, Revised April 2008.
90. OMEGA Engineering, The OMEGA Temperature Measurement Handbook and Encyclopedia, 6th Edition. Stamford, CT, 21st century edition.
91. Keltner, N., L. Nash, J. Beitel, A. Parker, S. Welsh and B. Gilda, Fire Safety Test Furnace Characterization Unit. *Thermal Measurements: The Foundation of Fire Standards*, ASTM STP 2002.
92. Golden Software Inc., Help Manual for Surfer version 8.00, Golden, CO, February 2002.

APPENDIX A

Bidirectional Probe Calibration Factors [11]

Probe Location		Calibration Factor (k)	
Hot Flow Rake (m)	Cold Flow Rake (m)	Windward Face	Leeward Face
-2.00	-4.65	1.08	1.10
-1.66	-4.03	1.08	1.08
-1.33	-3.41	1.08	1.05
-1.00	-2.79	1.09	1.08
-0.66	-2.17	1.10	1.09
-0.33	-1.55	1.09	1.10
0.00	-0.93	1.08	1.08
0.33	-0.31	1.06	1.09
0.66	0.31	1.10	1.09
1.00	0.93	1.07	1.11
1.33	1.55	1.08	1.08
1.66	2.17	1.09	1.10
2.00	2.79	1.07	1.09
2.33	3.41	1.09	1.10
2.66	4.03	1.08	1.10
3.00	4.65	1.09	1.08

APPENDIX B

Pressure Transducer High and Low Pressure Equations [11]

Probe Location		Type of Transducer	Fit Equation
Hot Flow Rake (m)	Cold Flow Rake (m)		
-2.00	-4.65	Low Pressure	$P=-25.83+5.245E-0.002002E^2$
-2.00	-4.65	High Pressure	$P=-252.6+50.36E-0.03403E^2$
-1.66	-4.03	Low Pressure	$P=-25.3+5.013E-0.001955E^2$
-1.66	-4.03	High Pressure	$P=-252.3+50.16E-0.01859E^2$
-1.33	-3.41	Low Pressure	$P=-25.23+4.966E+0.003328E^2$
-1.33	-3.41	High Pressure	$P=-252.7+50.43E-0.03355E^2$
-1.00	-2.79	Low Pressure	$P=-25.2+4.979E+0.0008156E^2$
-1.00	-2.79	High Pressure	$P=-252.3+49.79E+0.02606E^2$
-0.66	-2.17	Low Pressure	$P=-25.22+4.961E+0.003141E^2$
-0.66	-2.17	High Pressure	$P=-252.6+50.51E-0.04888E^2$
-0.33	-1.55	Low Pressure	$P=-25.32+5.059E-0.005689E^2$
-0.33	-1.55	High Pressure	$P=-252.5+50.08E-0.007468E^2$
0.00	-0.93	Low Pressure	$P=-25.19+5.001E-0.0001998E^2$
0.00	-0.93	High Pressure	$P=-252.1+49.43E+0.04555E^2$
0.33	-0.31	Low Pressure	$P=-25.31+5.029E-0.003172E^2$
0.33	-0.31	High Pressure	$P=-252.3+50.37E-0.03872E^2$
0.66	0.31	Low Pressure	$P=-25.26+4.999E-0.0002989E^2$
0.66	0.31	High Pressure	$P=-252.6+49.57E+0.04586E^2$
1.00	0.93	Low Pressure	$P=-25.23+4.994E-0.0003146E^2$
1.00	0.93	High Pressure	$P=-252.4+50.32E-0.0314E^2$
1.33	1.55	Low Pressure	$P=-25.27+4.997E-0.0006447E^2$
1.33	1.55	High Pressure	$P=-252.1+50.17E-0.01594E^2$
1.66	2.17	Low Pressure	$P=-25.28+5.005E-0.0001235E^2$
1.66	2.17	High Pressure	$P=-252.4+50.17E-0.008193E^2$
2.00	2.79	Low Pressure	$P=-25.26+4.990E+0.0009586E^2$
2.00	2.79	High Pressure	$P=-252.2+50.25E-0.02201E^2$
2.33	3.41	Low Pressure	$P=-25.2+4.974E+0.003123E^2$
2.33	3.41	High Pressure	$P=-252.8+50.3E-0.0294E^2$
2.66	4.03	Low Pressure	$P=-25.24+5.005E-0.0009042E^2$
2.66	4.03	High Pressure	$P=-252.4+49.97E-0.0007914E^2$
3.00	4.65	Low Pressure	$P=-25.29+5.021E-0.002516E^2$
3.00	4.65	High Pressure	$P=-252.6+50.39E-0.0368E^2$

Appendix C

Load Cell Calibration Factors

Test Series with the Blocking Object Present

-Y load cell 1 Volt = 45.481 kg

+Y load cell 1 Volt = 45.477 kg

Upwind load cell 1 Volt = 45.472 kg

Test Series with no Blocking Object Present

These load cells were calibrated as a system due to the presence of the different load cell compared to previous experiments

-Y load cell Weight (kg) = Voltage × 45.500 + 0.559

+ Y load cell Weight (kg) = Voltage × 45.091 – 0.738

Upwind load cell (kg) = Voltage × 46.182+ 0.187